Electronic structure studies of metal-organic and intermetallic compounds

by Albert F. Takács

UNIVERSITÄT OSNABRÜCK

Thesis advisor:
apl. Prof. Dr. Manfred Neumann

Contents

List of Figures

List of Tables

Chapter 1

Introduction

The understanding and prediction of the properties of matter at atomic level represents one of the great achievements of the last years in science. In this contents, the advantage of photoelectron spectroscopy, in the study of electronic structure and properties of matter is due to progress in both, experimental and in relevant theory. Photoemission techniques, have been developed sufficiently to become a major tool for the experimental studies of solids. These techniques are also attractive for the study of changes in, or destruction of, crystalline order. The understanding of the magnetic behavior of the matter in a detailed way, cannot be achieved without the complete study of the electronic structure.

In the present thesis, the aim is to present a complete study of the electronic structure of selected materials, by means of experimental and theoretical methods. The class of the materials which will be presented in this thesis, are belonging to magnetic molecules and intermetallic compounds type of classes.

Molecular magnetism is relatively recent scientific field which originated from the transformation of magnetochemistry in an interdisciplinary area where chemists and physicists started to collaborate very closely with the stated goal of designing, synthesizing, and characterizing the magnetic properties of molecular based materials [1]. Molecular magnets are a new class of materials which have been rigorously studied since their discovery several decades ago. Since then, new phenomenon have been discovered surrounding this materials and many new materials have been developed. Accordingly to Miller and Epstein, who have done considerably work in this field (1994), the molecular magnet is defined as those magnetic materials that are prepared by low temperature methods of the preparative chemistry [2]. The medium of study in this new field is the molecular magnet, which can come in many different arrangements and synthesis and can be extended over a broader range of materials that extends into the realm of organic, organic–inorganic, and inorganic molecular magnets.

In the quest for molecular magnets which might be useful for practical applications such as ultradense magnetic storage [3], quantum computing [4], or other interesting devices, one finds at times molecules which combine structural beauty, promising chemistry for further development, non–trivial physics and good properties (intramolecular exchange interactions, magnetic anisotropy). One of such system is studied in this thesis, namely

the "ferric star" molecule. One can call this molecule as being a "simple enough" to allow an accurate study of its electronic structure, yet far from trivial for what regards its chemical manipulation (crystallization with different ligands) and physical treatment. The general formula of the "ferric star"–molecule is $\{M[\mathrm{Fe}(\mathrm{L}^1)_2]_3\}\cdot4\mathrm{CHCl}_3$, where L^1 is an organic ligand and M is Fe or Cr. Magnetochemical investigations on the "ferric star" in the case of M=Fe (FeFe$_3$–star) indicate that the three spins S=5/2 of peripheral Fe ions at the star edges couple with an antiparallel orientation to the central ion, yielding the magnetic ground state of S=5. In the present thesis, the aim regarding the "ferric star"–molecule is to clarify the electronic structure, as it emerges from a combined spectroscopic study and first principle calculations.

The second class of materials which is studied in this thesis by means of electronic structure are the intermetallic compounds and alloys, namely the Mn–Pd class of intermetallic compounds. This materials are of highly interest because of their applicability as permanent magnets or as practicable hydrogen storage materials. The study of core level and valence band photoelectron spectra of $3d$ transition metals can yield important information on the electronic structure of their alloys and intermetallic compounds. The alloy $\mathrm{Mn}_x\mathrm{Pd}_{1-x}$ suffers a continuous transformation as it can be seen in the chapter dedicated for this materials, from the AuCu$_3$ to the AuCuI structure type, while passing through the tetragonally distorted periodic antiphase structure, with the changing of the Mn concentration. Diffraction measurements revealed that Mn–Pd alloys and compounds, order antiferromagnetically with Néel temperatures and magnetic moments on Mn site raging from approximately 200 to 825 K and 4 to 4.4 μ_B, respectively.

The doping of the Mn–Pd alloys and compounds can bring significant changes, not only in the crystallography of the compounds but also in their magnetic and electronic properties. For this reason, antimony was used as a doping material in order to see the effects which are taking place in the given compounds. For this case, the palladium atoms were replaced by antimony atoms by the given formula: $\mathrm{MnPd}_{3-x}\mathrm{Sb}_x$. In the parent compound, without antimony, the structure is formed in the following way, a Mn atom is surrounded by twelve Pd atoms, and a Pd atom by four Mn and eight Pd atoms, respectively. By replacing the Pd atoms with Sb atoms, three electrons per atom will be brought by Sb in the conduction band, leading to changes in the electronic, and magnetic structures.

The structure of the thesis is "build up" as it follows:

- In Chapter 2, a brief description of the experimental techniques used is given, namely X–ray photoelectron spectroscopy (XPS), X–ray emission spectroscopy (XES), X–ray absorption spectroscopy (XAS) and resonant X–ray emission spectroscopy (RXES).

- Chapter 3 presents the characteristics of the molecular magnets class of materials, the origin of them, as well as their properties, and formation of this magnets.

- In Chapter 4, experimental and theoretical results on the "ferric star"–single molecule magnet are presented, starting with the characterization of the molecule and studying the electronic structure of it. In this chapter, besides the experimental results

obtained at the different facilities (see Chapter 2), two theoretical models are included in order to explain the photoemission $3s$ splitting of the transition metal ions, and the magnetic interactions (superexchange interaction) which occur in the studied molecule.

- Chapter 5, gives a short description of the intermetallic compounds and alloys, together with their characteristic and properties.

- The 6-th Chapter presents spectroscopic, magnetic and theoretical study as well, on the Mn–Pd alloys and compounds. In particular, two systems are studied, the Mn_xPd_{1-x} and $MnPd_{3-x}Sb_x$ systems.

- In Chapter 7, the conclusions are presented together with the outlook of the presented thesis

Chapter 2

X-ray excitations produced by electron spectroscopies

The experimental methods used in this thesis are presented in this chapter. The aim for using this methods was to investigate the electronic structure of the investigated materials. The state of the art of the experimental methods is presented, including theoretical and practical details.

2.1 X-ray Photoelectron Spectroscopy (XPS)

X-ray photoelectron spectroscopy (XPS) is a widely-used technique for studying the properties of atoms, molecules, solids, and surfaces. The photoelectron spectroscopy (PES) has it roots over more than a century ago. H. Hertz and W. Hallwachs discovered the external photoelectric effect [5] in 1887 and in the following years refined experiments by J.J Thomson led to the disocery of the electron, thus elucidating the nature of photo-emitted particles [6]. The extent of development between the first experiments of this type by Robinson and Rawlinson in 1914 [7] and the present state of the art is indeed great, with most of this growth occurring within the last 40 years under the simulation of pioneering studies begun in the early 1950's [8, 9], particulary those carried out at Uppsala University.

From the first observation that core photoelectron peak intensities could be used for quantities analysis by Steinhardt and co-workers [8] and that core electron binding energies exhibited chemically-induced shifts by Siegbahn and co-workers [9], the number of distinct physical and chemical effects noted has expanded considerably. The group of K. Siegbahn from Sweden reported substantially improvements on the energy resolution and sensitivity of the so-called β spectrometers. The determination of electron binding energies in atoms was improved by using X-rays ($h\nu \simeq 1500$ eV). This technique was named *Electron Spectroscopy for Chemical Analysis* (ESCA). Thus, together with numerous developments in interpretive theory, this expansion has provided a rich panoply of information that can be derived by analysing different aspects of an x-ray electron spectrum. To be sure, a greater understanding of the theoretical models underlying these phenomena has not always led to

results as directly interpretable in simple chemical or physical terms as was initially imagined, but overall scope of information derivable is nonetheless large enough to be useful in a broad range of disciplines [10].

2.1.1   Principles of the technique

The basics of PES data acquisition are based on the photoelectric effect. A photon of known energy is used to impart energy on an electron. The electron uses this energy to overcome the binding energy holding it to the atom. The electrons remaining energy is in the form of kinetic energy, which is measured. Thus the binding energy for the electron is determined by taking the difference between the incident photons energy and the kinetic energy possessed by the photoelectron. A PES experiment is presented in Fig.2.1. Photoelectron spectroscopy is a modern development of early experimentation on
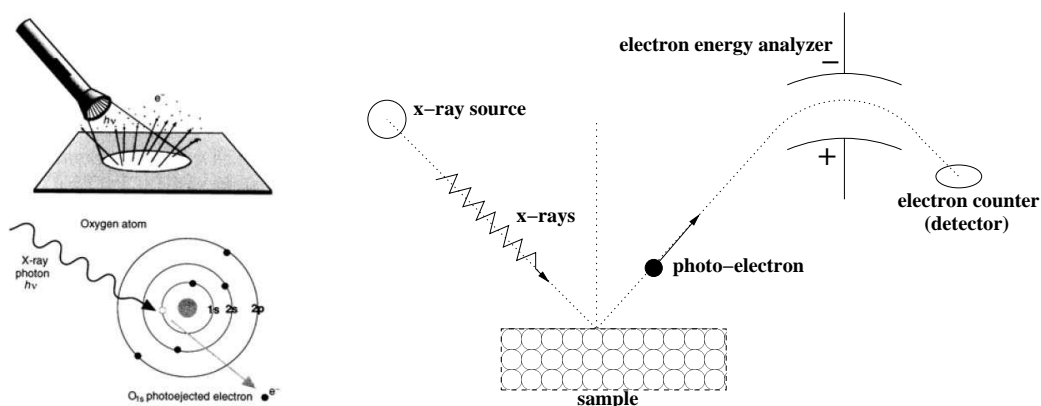
Figure 2.1: *Schematic representation of a PES experiment*

the *Photoelectric Effect*. Furthermore, it was shown that the kinetic energy of the ejected photoelectron dependeds only on the wavelength of the impacting photons, and not on their intensity. Regarding the energy of the incident radiation, the experimental techniques are labelled as: **X-ray Photoelectron Spectroscopy** (XPS) with $h\nu > 1000$ eV, **Soft X-ray Photoelectron Spectroscopy** (SXPS) with 100 eV $< h\nu < 100$ eV, **Ultra-Violet Photoelectron Spectroscopy** (UPS) with $h\nu < 100$ eV. AlK_α (1486.6 eV) and MgK_α (1253.6 eV) are the most used incident X-rays in the case of XPS. What makes XPS and attractive surface science tool, is that photons have limited penetrating power in a solid to the order of 1-10 micrometers, and the escape depht of the emitted electrons is limited to $\simeq 50$Å. The Einstein Photoelectric Law[1], together with the general case of electrons situated on different bounded levels gives the kinetic energy (E_{kin}) of the ejected electrons:

$$E_{kin} = h\nu - E_B - \Phi \tag{2.1}$$

---

[1]Albert Einstein was awarded with the Nobel Prize in Physics in 1921 "for his service to Theoretical Physics, and especially for his discovery of the law of the photoelectric effect"

with E_B the binding energy of the atomic orbital from which the electron originates and Φ the work function. For the case of solid specimens, an electrical connection is made to the spectrometer in an attempt to minimize charging effects and maintain a well-defined and fixed potential during photoemission. For the simplest possible case of a metallic specimen in a metallic spectrometer, the energy levels and kinetic energies which result are shown in Fig. 2.2.
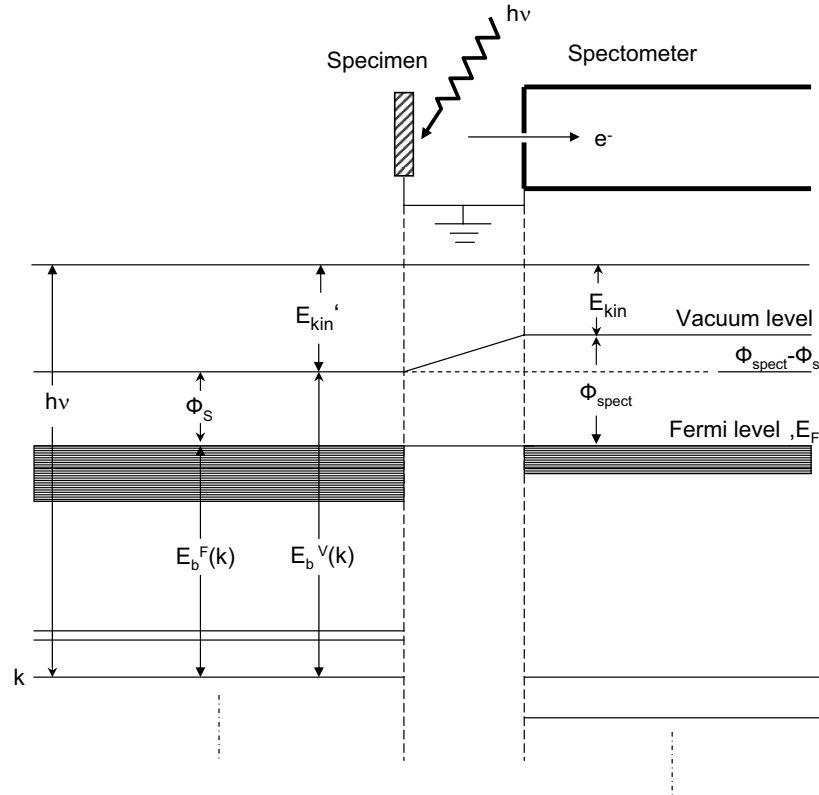
Figure 2.2: *Energy level diagram for a metallic specimen in electrical equlibrium with an electron spectrometer. The closely spaced levels near the Fermi level E_F represent the filled portions of the valence bands in specimen and spectrometer. The deeper levels are core levels. An analogous diagram also applies to semi-conducting or insulating specimens, with the only difference being that E_F lies somewhere between the filled valence bands and the empty conduction bands above.*

Thermodynamic equilibrium between specimen and spectrometer requiers that their electron chemical potentials or Fermi levels be equal as shown. In a metal the absolute zero (T= 0K), the Fermi level E_F has the interpretation as being the highest occupied level, as indicated in the figure; this interpretation of E_F is also a very good approximation for metals at normal experimental temperatures. For semiconductors and insulators, however,

it is not so simple to locate the Fermi level, which lies somewhere between the filled valence bands and the empty conduction bands. The work function Φ for a solid is defined to be the energy separation between the vacuum level and the Fermi level. When connected as shown in Fig. 2.2, the respective vacuum levels for specimen and spectrometer need to be equal, however, so that in passing from the surface of the specimen into the spectrometer, an electron will feel an accelerating or retarding potential equal to Φ-Φ_{spect}, where ϕ_{spect} is the spectrometer work function. The X-ray phototelectron spectrum represents the number
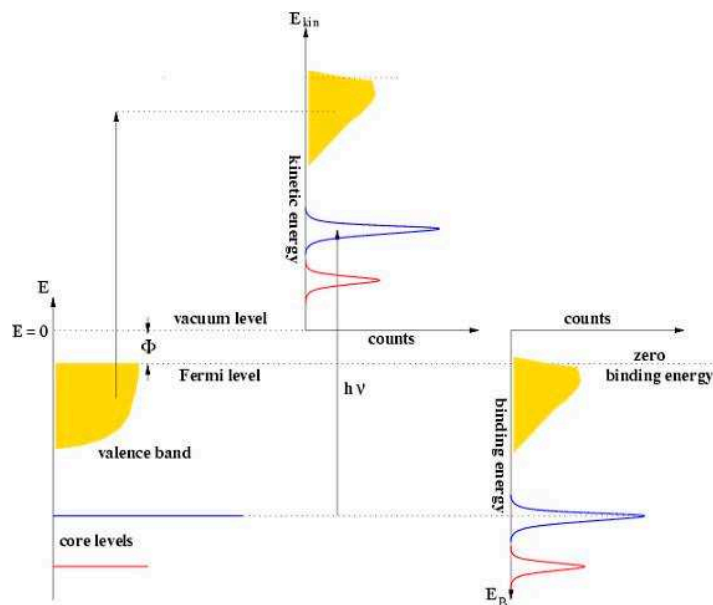
Figure 2.3: *Representation of energy levels in a solid with the corresponding XPS spectra*

of electrons, recorded with the detector versus their kinetic energy, measured by using the electron analyzer. The kinetic energy depends on the energy of the incident radiation while the binding energies are solely material specific, and for this reason in general it is preferred to use a binding–energy abscissa (see Fig. 2.3).

2.1.2   Data analysis

The aim of spectral analysis in XPS is to determine the location, intensities, and, in certain cases also shapes of the various peaks observed, many of which are not clearly resolved from one another. Three main conditions must be achieved in order to full fill these conditions:

- All peaks will exhibit inelastic tails toward low kinetic energy and these tails may in turn exhibit structure. For many solids the inelastic tail can be roughly approximated by a linear or a constant function , with extra features perhaps superimposed on it. Valence band spectra from solids have been corrected for inelastic scattering by using a close-lying core level to derive the form of the inelastic tail, [11, 12] as well as by

the more approximate procedure of assuming an asymptotically constant tail at low kinetic energy whose value at any energy is proportional to the integrated ni-loss peak intensity at higher kinetic energies.

- All peaks ride on a background of secondary electrons from higher-kinetic-energy peaks. For the case of narrow energy regions, the background can be approximated as linear or constant.

- The basic peak shape observed in XPS are a convolution of several variable factors: exciting x-ray lineshape, contributions from weaker x-rays such as satellites from non-monochromatized sources, the analyzer lineshape, possible non-uniform specimen charging, a Lorentzian hole-state lifetime contribution, Doppler broadening in gases [13], and various final-state effects involving many-electron excitations [14] and vibrational excitation [15]. Thus, no universal peak shapes of Gaussian or Lorentzian form, to which are smoothly added an asymptotically constant inelastic tail of variable height [16]. The effects of satellite x-rays can also automatically be included in the basic peak shape chosen, and a variable linear background is also present.

2.1.3 Theory of Photoelectron Spectroscopy

A rigorous theoretical description of the photoemission process implies a full quantummechanical treatment of the process in which an electron is removed from an occupied state within the solid and then detected. Theoretical approaches of this type treat photoemission as a onestep process. Less accurate, but very simple, is the threestep model that is a phenomenological approach.

2.1.3.1 Sudden approximation

A description from the theoretical point of view, of the photoelectron process will be described as it follows. In any photoelectron emission experiment, the basic excitation process involves absorption of a photon of energy $h\nu$ according to:

$$\Psi^i_{tot}(N), E^i_{tot}(N) \xrightarrow{h\nu} \Psi^f_{tot}(N, K), E^f_{tot}(N, k) \tag{2.2}$$

Here $\Psi^i_{tot}(N)$ is the initial-state N-electron wave function corresponding to a total energy $E^i_{tot}(N)$, and $\Psi^f_{tot}(N, K)$ is the K-th final-state N-electron wave function (including the photoelectron) corresponding to a total energy of $E^f_{tot}(N, K)$. The relevant energy conservation equation is:

$$E^i_{tot}(N) + h\nu = E^f_{tot}(N, K) \tag{2.3}$$

In the simplest situation, the index K thus labels the one electron orbital k from which emission occurs, but in general it should describe all possible excitations within the final state, including electronic, vibrational, and translational. In all forms of higher-energy photoelectron spectroscopy, it is customary to assume that the photoelectron is sufficiently

weakly coupled to the (N-1) electron ion left behind so as to permit separating the final state of the excitation process to yield:

$$\Psi_{tot}^i(N), E_{tot}^i(N) \xrightarrow{h\nu} \Psi_{tot}^f(N-1,K), E_{tot}^f(N-1,K) + \phi^f(1)\chi^f(1), E_{kin} \qquad (2.4)$$

in which $\Psi_{tot}^f(N-1,K)$ and $E_{tot}^f(N-1,K)$ refer to the K-th $(N-1)$ electron ionic state that can be formed, E_{kin} is the kinetic energy of the K-th photoelectron, $\phi^f(1)$ is the spatial part of a one electron orbital describing the photoelectron and $\chi^f(1)$ is the spin part of the photoelectron orbital ($\chi=\alpha$ or β). The form of $\phi^f(1)$ thus depends on the kinetic energy. $\Psi_{tot}^f(N-1,K)$ and $\phi^f(1)$ can be combined in a suitable sum of products to yield the correct overall antisymmetry with respect to electronic coordinates necessary in the final state. This can be written with an antisymmetrizing operator $\hat{A}$ as: [17, 18]

$$\Psi_{tot}^f(N,K) = \hat{A}(\phi^f(1)\chi^f(1), \Psi_{tot}^f(N-1,K)) \qquad (2.5)$$

The resulting energy conservation equation is that most useful in analyzing XPS spectra:

$$E_{tot}^i(N) + h\nu = E_{tot}^f(N-1,K) + E_{kin} \qquad (2.6)$$

The binding energy corresponding to the ion in a state described by $\Phi_{tot}^f(N-1,K)$ is thus given by:

$$E_b^v(K) = E_{tot}^f(N-1,K) - E_{tot}^i(N) \qquad (2.7)$$

in which the vacuum level reference is implicit. An inherent source of linewidth in any binding energy measurement is thus energy broadening due to lifetime effects in either the initial and final state. If the relevant lifetime is denoted by τ, uncertainly principle arguments thus lead to a broadening that is Lorentzian in shape, with a FWHM (full with at half maximum) in eV given by $\sim \hbar/\tau = 6,58 \times 10^{-16}/\tau(s)$. The initial state lifetime is usually very long, and so contributes negligible broadening. However, final-state lifetimes are estimated to be as short as 10^{-18} s in certain cases, so that such effects can play a major role in limiting XPS resolutions, particulary for inner subshell excitation.

2.1.3.2   Three step model

The photoelectron process is considered in this model as having three distinct contributions:

1. the local absorption of the photon and the excitation of the (photo)electron (photoionization);

2. the propagation of the electron through the sample to the surface;

3. the penetration of the photoelectron through the surface and emission into the vacuum, where it is detected.

2.1.4   Spectral Characteristics

The first step which is taken generally in the sample characterization is the recording of a wide scan. This is the so called survey spectrum, which allows to identify the chemical components in the sample and to define acquisition windows. The lines which are of interest are recorded afterwords with a high resolution. The XPS spectra can be divided into: *primary spectrum* which is given by the electrons which leave the solid without inelastic scattering processes, and *secondary spectrum* arising from photo-electrons which have already lost a percentage of their kinetic energy trough inelastic scattering processes on their way to the surface.

2.1.4.1   Core levels

Photoemission produces a final state that is lacking one electron with respect to the initial state. Therefore PES (photoemission spectroscopy) always measures final-state energies which can be related to initial-state energies only after some theoretical considerations, as it was mentioned in the last paragraph. The XPS lines associated with the core levels may have variable intensities and widths, which, except for the s levels, are doublets. Photoelectrons, which originate from core-levels, give rise to the most intensive lines in the XPS spectra. The position of the core level lines is like a fingerprint for each element and thus the chemical identification of the components in the investigated specimen can be easily performed. Generally two or more elements will be detected on the surface. The relative intensities of their lines is governed by: occupancy of the sub–shell, stoichiometry, atomic cross-section σ. The values of σ can be derived from X-ray mass absorption coefficients or can be directly calculated [23, 24]. Since the occupancy of the atomic sub-shells is known, XPS can be used as a non-destructive chemical analysis tool. The width of the
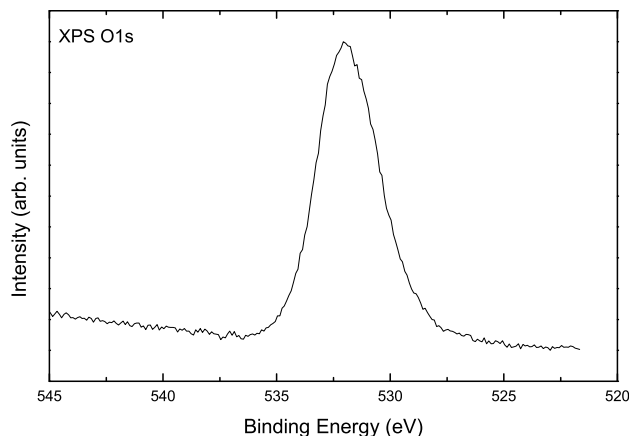
Figure 2.4: *Illustration of a core level*

The first process, namely the optical excitation of the electron, is described by Fermi's golden rule:

$$\omega \sim |\langle \Psi_f | H^* \Psi_i | \rangle|^2 \delta(E_f - E_i - h\nu) \tag{2.8}$$

For an energy E and a wave vector around k, the internal electron current $I_{int}(E, h\nu, k)$ is given by [2]:

$$I_{int}(E, h\nu, k) = \sum |\Psi_f| H^* |\Psi_i|^2 f(E_i) \delta(E_f(k) - E_i(k) - h\nu) \delta(E - E_f(k)) \tag{2.9}$$

where $f(E_i)$ is the Fermi distribution function. During the propagation to the surface, many electrons lose a part of their energy by electron-electron and electron-plasmon scattering. The continuous background in the XPS spectrum is due to such electrons, which do not carry any more information about their initial states. The transport probability $D(E; k)$, which describes the propagation process, is proportional to the mean-free path λ:

$$D(E, k) \sim \lambda(E, k) \tag{2.10}$$

where λ depends on the energy E, electron wave factor k, and the particular crystallographic direction. The penetration of the electron through the surface depends on the transmission rate [3]

$$T(E, k)\delta(k_{\parallel} + G_{\parallel} - k_{\parallel}^{ex}) \tag{2.11}$$

Taking into account the three steps described above, the detected (external) emission current can be written as:

$$I_{ext}(E, h\nu, k_{\parallel}^{ex}) = I_{int}(E, h\nu, k) D(E, k) T(E, k) \delta(k_{\parallel} + G_{\parallel} - K_{\parallel}^{ex}) \tag{2.12}$$

2.1.3.3 One step model

Apart from its didactic simplicity, the three step model fails to offer a practical computational tool for the simulation of photoelectron lines. State of the art is the employment of one step theoretical approaches in which the whole photoelectron process is regarded as a single one. The first of this kind was a compact and mathematically elegant solution to the previous three-step model [19] but was followed by fully dynamical [20] and relativistic one step theories [21] . When specific crystal potentials are given as input data one step models deliver theoretical simulations of the XPS spectra [22].

---

[2]It is necessary to mention that only the electrons with energies above vacuum energy and with the final state vector k directed outwards from the surface (k⊥0) can be detected

[3]$K_{\parallel} + G_{\parallel} = K_{\parallel}^{ex}$ is required by the conservation of the electron wave vector parallel to the surface

peak is defined as the full width at half maximum intensity (FWHM) (see Fig2.4). This is a sum of three distinct contributions [25]: the natural inherent width of the core-level γ_n, the width of the photon source γ_p and the analyzer resolution γ_a. Thus the overall FWHM will be given by:

$$\gamma = \sqrt{\gamma_n^2 + \gamma_p^2 + \gamma_a^2} \tag{2.13}$$

The first contribution is dictated via the uncertainty principle $\Delta E \Delta t \geq \hbar$ by the core-hole life time τ.

$$\gamma_n = \frac{h}{\tau} \tag{2.14}$$

where h is the Plank constant. The lifetimes depend on the relaxation processes which follow the photoemission. The narrowest core-levels have lifetimes in the range $10^{-14} - 10^{-15}$ s whilst the broader have lifetimes close or slightly less than 10^{-15} s.

2.1.4.2 Spin-orbit coupling

As it was discussed in the previous section, all core lines except the s levels, are doublets. This character of the core–level lines arises through the *spin-orbit* (j − j) coupling (see Fig. 2.5) In the j − j coupling scheme, the total angular momentum of one electron
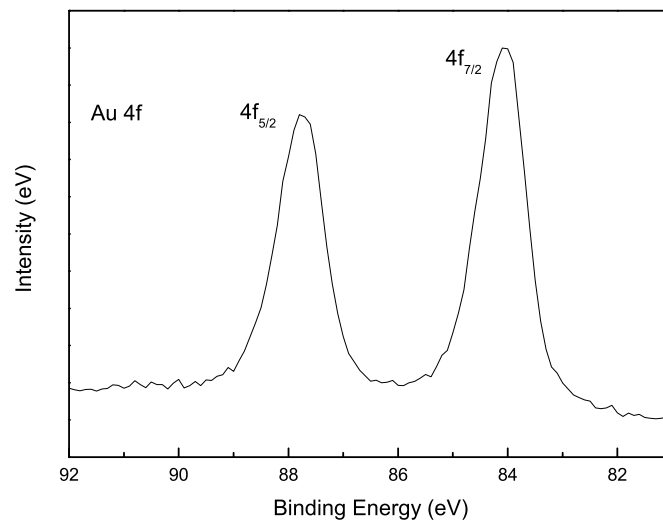
Figure 2.5: *Drawing of the spin-orbit splitting*

(j) is given by the sum of the electronic spin and angular momenta (j = l + s). To obtain total angular momentum of an atom J, one has to sum all total angular momenta of the constituent electrons: $J = \sum j$. Therefore, except the case of $l=0$ (for the s levels), for each state there will be a doublet in the XPS spectrum. Taking into account that for a given j

value there are $(2j+1)$ allowed states for electrons and that s $= 1/2$, the ratio of relative intensities can be easily calculated:

$$\frac{I_{j=l-s}}{I_{j=l+s}} = \frac{2(l-\frac{1}{2})+1}{2(l+\frac{1}{2})+1} = \frac{l}{l+1} \qquad (2.15)$$

High-resolution core-level spectroscopy studies show small deviations from this branching-ratio due to different cross sections for the $j=l+s$ and $j=l$-s lines and photo-diffraction effects.

2.1.4.3   Chemical shifts

In the investigation of the molecules and solids, one is not interested in the absolute binding energy of a particular core level, but in the change in binding energy between two different chemical forms of the same atom. This difference is the so-called *chemical shift* [26]. Using a simple model one can discuss how the chemical shift arises. As an example the Li 1s level in Li metal and Li oxide is chosen. Fig. 2.6 gives a representation of the
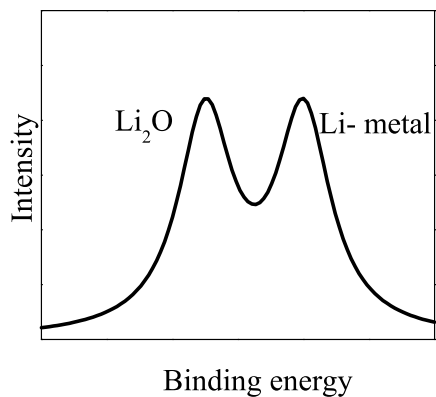
Figure 2.6: *Schematic drawing of the electron configuration of Li metal and Li_2O, and the corresponding Li 1s PES spectra (after [26])*

electronic structure of these two systems. In lithium metal the lithium 2s electrons form a band, and their wave function is therefore only partly at the site of a particular lithium atom. However, in lithium oxide each lithium atom donates its 2s electrons totally into the 2p shell of oxygen such that a closed $2p^6$ configuration is obtained. Thus in Li_2O in principle one can not speak about Li $2s$ electrons because the former Li $2s$ electrons (atomic case) are now O $2p$ electrons. The 1s electrons in lithium oxide therefore feel a somewhat stronger Coulomb interaction than in Li metal, where the lithium nucleus is screened from the $1s^2$ shell through the 2s valance electron. Therefore the binding energy of the Li 1s level is larger in Li_2O than in Li metal and a "chemical shift" between the two compounds is observed. The chemical shift between a metal and its oxide very often serves

to monitor the surface cleanliness. For example, the absence of oxygen is proven by the absence of the chemically shifted (to higher binding energies) metal oxide line (after [26]).

2.1.4.4 Satellites

Atoms, molecules and solids are many-electron systems. Since the electrons interact with each other via the Coulomb and exchange interaction, the emission of one electron after the photoexcitation process can and must lead to excitations in the remaining system. The excitations require energy and therefore lead to signals in the PE spectrum with a smaller kinetic energy (larger binding energy) than the signal corresponding to the ground state of the system after the PE process. This means that the PE spectrum must consist of the *main line* (representing the ground state after photoexcitation) and a number of *extra lines* (satellits) representing the excited states. In solids is yet another source which gives rise to additional lines in the PE spectrum. Here the photoexcited electron travels a relatively long way through a volume which is occupied by other electrons, and therefore has the possibility of exciting them. This excitation energy delivered to the sample must again be supplied from the kinetic energy of the outgoing electron and therefore this photoelectron may be observed with a kinetic energy smaller than that expected otherwise.

The electrons which are travelling through the solid without any loss are responsible for the so-called *no–loss line* (main line), while those experiencing an inelastic collision on their way from the site of photoexcitation to the surface constitute the "inelastic tail", which generally consists of a featureless part and discrete peaks. One can see that in
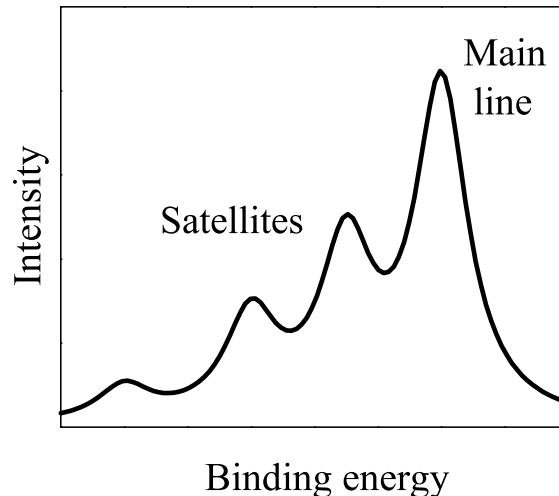
Figure 2.7: *Example of a main line and it's satellites*

principle we can discuss about two sources of extra structures in the PE spectrum, an *intrinsic* part (created in the photoemission process) and an *extrinsic* part (created by the photoexcited electron in a solid via other electrons during its travel to the surface).

For the insulating samples a reorganization of the electronic structure in form of a *charge transfer* occurs after the creation of a core hole [27, 28, 29, 30, 31, 32]. The process of the charge transfer mechanism is presented in Fig. 2.8 in case of a transition metal oxide and in terms of a molecular orbital description (after [33]). Because of the creation of a core
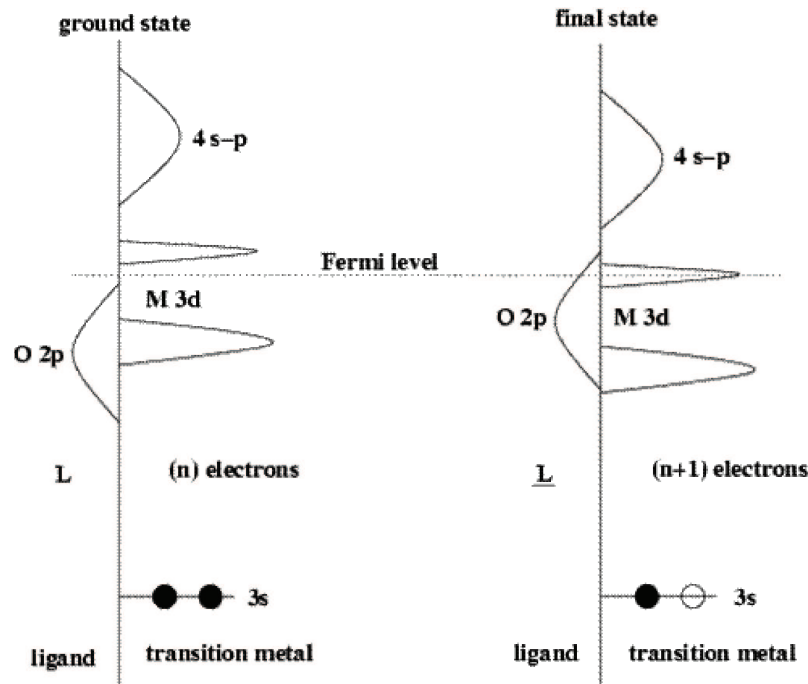
Figure 2.8: *Schematic representation of charge transfer process in transition metal oxides*

hole on the s level, the Coulomb interaction pulls down the valence states in order to fill up the created core. During this process, an electron will be transferred from the ligand to metal valence states and thus the total energy of the $(N-1)$ system will be minimized. In the given example the donor ligand shell is 2p of O^{2-}. For this case the charge transfer process is characterized by:

$$3s^2 3d^n L \longrightarrow 3s^1 3d^{n+1} \underline{L} \tag{2.16}$$

where n represents the number of electrons in the 3d sub-shell, L is the ligand and $\underline{L}$ denotes the loss of an electron on the ligand valence sub-shell. The deexcitation of the photohole leads to quantized excitations in the conduction-electron system, namely to the creation of *plasmons*[4]. These are called intrinsic plasmons, because they are an intrinsic property of the photoemission process. In contrast extrinsic plasmons are excited somewhere else in the solid by the outgoing photoelectron during its travel from the place of the photoexcitation process to the surface [34, 35, 36]. The reorganization of electronic structure after the creation of a core hole could also lead to an excess of energy which is not available to

---

[4]This is not always the case. In insulators plasmons are not possible. Plasmons excitations requires a free electron gas (i.e. metals).

the primarily excited photoelectron. Thus two-electron processes can occur in case of conducting samples. The corresponding structures in the spectra are denoted as shake satellites. The hole appears to increase the nuclear charge and this perturbation is the cause of valence electron reorganization. It may involve the excitation of one of them to a higher energy level. If an electron is excited to a higher bounded state then the corresponding satellite is called *shake-up* satellite. If the excitation occurs into free continuum states, leaving a double ionized atom with holes both in the core level and valence shell, the effect is denoted as a *shake-off* satellite [37].

2.1.4.5 Core-line shapes

A range of physically possible line profiles in core-level XPS is possible, and simple Gaussian or Lorentzian functions are very rarely adequate. In the case of metal samples it has been shown that asymmetric profiles should be expected on theoretical grounds [38], however, recorded spectra exhibit deviations from idealized profiles due to a range of instrumental and physical effects:

- The response function of the electron analyzer

- The profile of the X-ray line-shape

- Intrinsic life-time broadening of the core level hole state

- Photon broadening

- Differential surface charging of the sample

In addition to the instrumental considerations the shape of a synthetic peak is also influenced by the choice of background algorithm used to remove the so-called extrinsic electrons from the data. The intrinsic part of the XPS peak due to the core-level life time is described by a Lorentz function:

$$f_L(\epsilon) = \left(1 + \frac{4\epsilon^2}{\gamma_n^2}\right)^{-1} \tag{2.17}$$

where $\epsilon = E - E_0$ is the difference relative to the maximum of the curve. The overall line shape of core lines are obtained by convoluting the above two functions in a resulting so-called Voigt profile:

$$f_L(\epsilon) = f_L \otimes f_G = \int_{-\infty}^{+\infty} f_L(\epsilon') f_G(\epsilon - \epsilon') d\epsilon' \tag{2.18}$$

Doniach and Sunjic [38] have shown that in metals the core level lines have a characteristic asymmetrical shape.

$$f_{DS}(\epsilon, \alpha) = \frac{\Gamma(1-\alpha)}{(\epsilon^2 + (\gamma_n/2)^2)^{(1-\alpha)/2}} \cos\left[\frac{\pi\alpha}{2} + (1-\alpha)\arctan\left(\frac{2\epsilon}{\gamma_n}\right)\right] \tag{2.19}$$

where Γ is the gamma function, $\Gamma(z) = \int\limits_{0}^{\infty} t^{z-1}e^{-t}dt$, and α is an asymmetry parameter. The values of α can range between 0.1 and about 0.25 [39]. For the case of non-conducting samples the asymmetry factor is equal to zero and $F_{DS}(\epsilon, 0) = f_L(\epsilon)$. The asymmetry of the intrinsic XPS lines of conducting samples can be explained by taking into account the nonzero density of states at the Fermi level.

2.1.4.6   Multiplet splitting

In any atomic system with unpaired valence electrons, the exchange interaction affects spin-up and spin-down core electrons differently. Since exchange acts only between electrons with the same spin [40], core electrons with spins parallel to those of the unpaired valence electrons will experience a valence-electron exchange potential, whereas core electrons with spins antiparallel will not. Exchange interactions within or between closed shells balance exactly, as the numbers of electrons with same spin are equal. This interaction between core and unpaired valence electrons is responsible for core-polarization contributions to magnetic hyperfine structure [41]. The spectral splitting of the $3s$ core-level x-ray photoemission spectra (XPS) in transition metals and their compounds originates from the exchange coupling between the $3s$ hole and the $3d$ electrons and was experimentally observed about three decades ago [42, 43]. The magnitude of the $3s$ spectral splitting according to the van Vleck theorem [44] is determined by:

$$\Delta E_{ex} = \frac{1}{2l+1}(2S+1)G^2(3s, 3d) \qquad (2.20)$$

where S is the total spin of the ground state of the $3d$ electrons, l is the orbital quantum number ($l=2$) and $G^2(3s, 3d)$ is the Slater exchange integral. A core-level line with a doublet, $3s$ multiplet splitting is presented in Fig. 2.9. The intensity ratio for the two
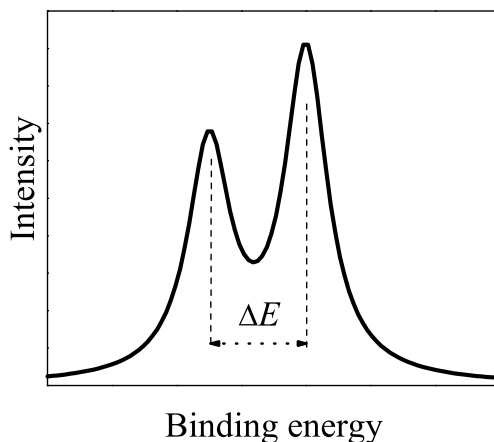
Figure 2.9: *Representation of a 3s multipet splitting*

peaks is proportional in this model to the ratio of the angular momentum multiplicity:

$$\frac{I\left(S+\frac{1}{2}\right)}{I\left(S-\frac{1}{2}\right)} = \frac{2\left(S+\frac{1}{2}\right)+1}{2\left(S-\frac{1}{2}\right)+1} = \frac{S+1}{S} \tag{2.21}$$

For $3d$ metal compounds, the calculated $3s$ splitting is more than two times larger than the observed one. It indicates that the $3s$ splitting is not likely to be due to the spin exchange only. This fact was explained by the intra-shell correlation effects between $3s^13p^63d^n$ and $3s^23p^43d^{n+1}$ configurations [45, 46]. The above scheme does not take into account the effect of a core-hole screening in the final state of the photoemission. The final-state screening gives satellites in the x-ray photoelectron core-level spectra whereas "main peaks" usually correspond to the final states with an extra $3d$ electron in comparison with the ground state [47]. Veal and Paulikas [48] proposed that the $3s$ splitting is determined by the exchange interaction in the $3s^13d^{n+1}$ configuration rather than in the $3s^13d^n$ configuration. This model is correct only for compounds with more than six d electrons (e.g. Ni and Cu). It was proposed that the $3s$ splitting reflect the local magnetic moment in the ground state only when charge-transfer satellites in the $2p$ core-level spectra are negligible. Spin-resolved photoemission studies allowed a better view on the magnitude of exchange-interaction effects [49, 50, 51, 52]. State of the art in the theoretical treatment of the $3s$ multiplet splitting is the resolving of the proper Anderson hamiltonian in the impurity approximation [53, 54]. A full description or interpretation of the $3s$ XPS line can be achieved by taking into account the interpretation of the $2p$ XPS line. The $3s$ line is a good measure of the local moment of the ground state only when the charge-transfer satellite in the $2p$ core level spectra is small.

2.1.4.7 Background features

During their transport to the surface, some photoelectrons lose part of their energy through inelastic scattering processes and end up at a lower energy in the spectrum, giving rise to a background. For quantitative analysis of the XPS spectra, the true peaks areas and their shapes need to be determined. Therefore, usually background corrections are applied. Shirley was the first to deal with this problem and he proposed a practical model [55]. However its results are in most of the cases unsatisfactory. In the Tougaard algorithmus [56, 57, 58, 59] the measured spectrum $j(E)$ is considered to consist of a primary photoelectron spectrum $F(E)$ and background, as given:

$$j(E) = F(E) + \lambda(E)\int_E^\infty K(E, E - E')j(E)dE' \tag{2.22}$$

where $k(E, E - E')$ describes the probability that an electron with the energy E loses the energy $(E' - E)$ during a mean free path travel. The second term in eq. 2.22 gives the background correction. A universal loss function $\lambda(E)K(E, T)$ which should describe all

pure materials was proposed

$$\lambda(E)k(E,T) = \frac{B(T)}{[C + T^2]^2} \qquad (2.23)$$

where B and C are two constants. By comparison with experimental data, it was shown that the background correction for pure Ag, Au and Cu can be described using the following values: $B = 2866$ eV^2 and $C = 1643$ eV^2. In case of alloys this universal loss function delivers a general good fit with experiment. An accurate background can be obtained only from EELS (Electron Energy Loss Spectroscopy) experiments. In an EELS experiment electrons with kinetic energy E_0 are sent on the sample. A certain part of them will be reflected but the rest enter the surface and interact with the solid. Due to scattering processes the electrons lose energy E_L and leave the solid with the kinetic energy $E_S = E_0 - E_L$. The outgoing electrons are recorded energy resolved. In other words such an experiment simulates the kinetic energy loss of the XPS electrons [60].

2.1.4.8 Auger process

In Fig 2.10 presents a schematic energy level diagram of a solid, in which the energy is measured downwards from an assumed zero of energy at the Fermi level. In the center of Fig. 2.10 the sequence of events following ionization of a core level is shown. In this example the K level is being ionized by an incident electron, whose energy E_p must be greater than the binding energy E_k of an electron in the K shell. Following creation of a hole in the level K, the atom relaxes by filling the hole via a transition from an outer level, in this example from the as L_1 level. As a result of that transition the energy difference
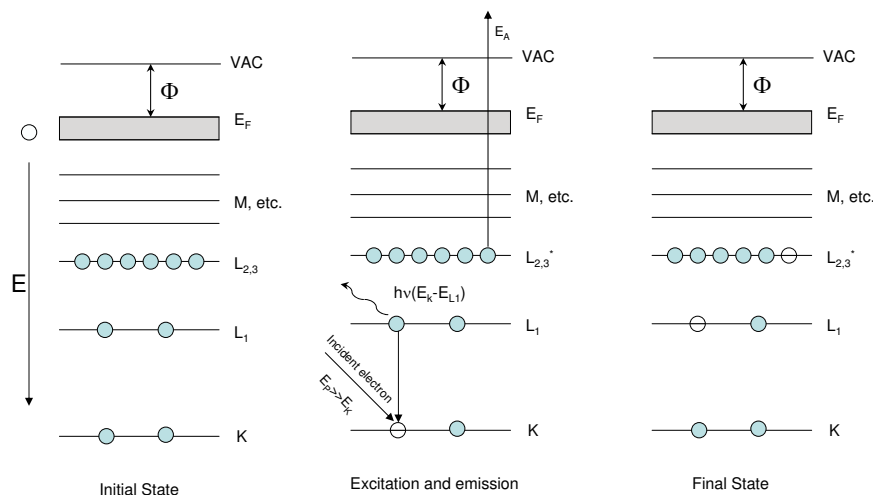
Figure 2.10: *Schematic diagram of the process of Auger emission in a solid*

$(E_K - E_{L_1})$ can be used by the atom in either of two ways. It can appear as a characteristic

X-ray photon of that energy or it can be given to another electron either in the same level or in a more shallow level, whereupon the second electron is ejected. This first process is that of X-ray fluorescence, the second that of Auger emission. Both cannot take place from the same initial core hole, so that they complete. The Auger transition depicted in Fig 2.10, would be named in the conventionally used $j - j$ coupling $KL_1L_{2,3}$. The electrons taking part in the Auger process might also originate in the valence band of the solid, in which case the convention writes the transitions as, for example, $KL_{2,3}V$ if one electron comes from the valence band and, for example, KVV if both do. The energy of the ejected Auger electron is given by:

$$E_{KL_1L_{2,3}} = E_K - E_{L_1} - E^*_{L_{2,3}} \tag{2.24}$$

where E_i is the binding energies of the i-th atomic energy level. $E^*_{L_{2,3}}$ is starred because is the binding energy of the $L_{2,3}$ level in the presence of a hole in level L_1, and is therefore different from $E_{L_{2,3}}$.

2.1.5 Experimental details

2.1.5.1 Instrumentation

The XPS experiments presented in this thesis were performed using a commercially available spectrometer PHI Model 5600 Multi-Technique System produced by the Perkin Elmer Corporation. The PHI spectrometer is build up from: a control computer, electronic control units, a "quick-entry" system and a main and preparation chamber. The measurements are performed in the main chamber while the preparation chamber is used to prepare the samples to be measured. A simple scheme of the PHI spectrometer is presented in Fig. 2.11. The main features of the spectrometer are presented and discussed in
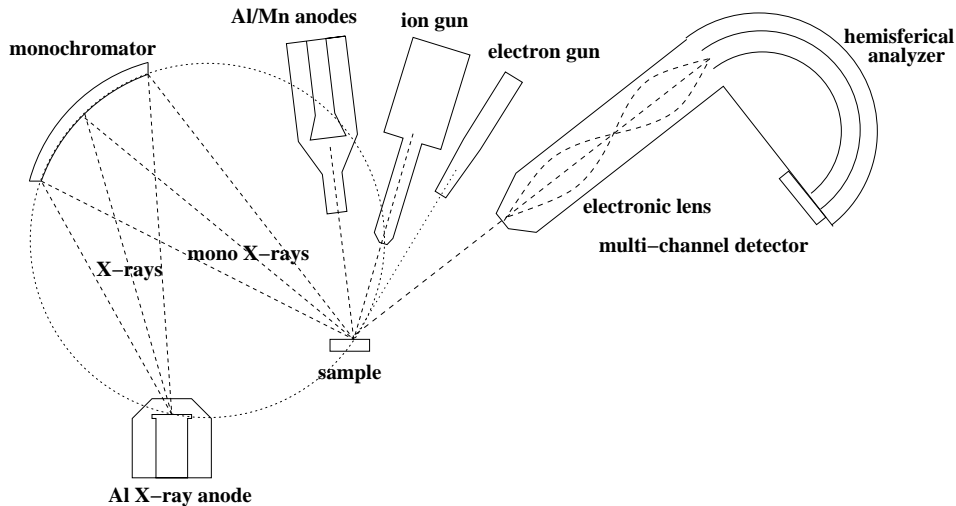
Figure 2.11: *Schematic representation of an XPS Spectrometer*

the following paragraph:

- **X–Ray sources:** Concerning the radiation sources the PHI 5600 spectrometer is equipped with a dual Al/Mg anode. X-rays are produced by bombardment of an anode at high positive potential with electrons from a hot filament at earth potential. The energies of the Al K_α and Mg K_α radiations are 1486.6 eV and 1253.6 eV. The half-widths for the unmonochromatized radiations are 0.85 eV and 0.7 eV, respectively [61] . The "orbital angular symmetry factor", which is given by the positioning of the dual Al/Mg anode (magic angle= 54.7° to the analyzer), $L = 1 + \beta(3\sin^2\theta/2 - 1)/2$ where β is a constant for a given sub-shell and θ is the source sample analyzer angle, becomes equal to 1.

- **Analyzer:** The energy of the ejected electrons is filtered using an 11 inches hemispherical condenser. The analyzer is build up from two concentrically assembled hemispheres of inner radii R_1 and outer radii R_2, a deflecting potential V being applied between the two hemispheres. A schematic representation of the analyzer, is presented in Fig. 2.12. The photoelectrons are focused with an electronic lens system
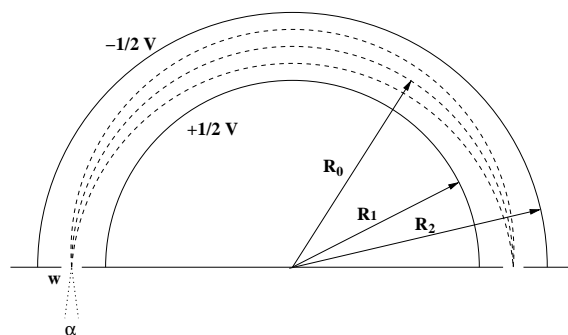
Figure 2.12: *Concentric Hemispherical Analyzer*

and then enter the analyzer through an entrance slit w which can be set to 4, 2, 0.5 or 0.15 mm. During XPS measurements the "constant analyzer transmission" (CAT) mode is used, meaning that only electrons with the energy $E_p \pm \Delta E$ (where E_p is the "pass-energy" and ΔE is the absolute energy resolution) may pass through the analyzer. The relative resolution of the analyzer is given by the:

$$\frac{\Delta E}{E_0} = \frac{w}{2R_0} + \frac{\alpha^2}{4} \tag{2.25}$$

where E_0 is the kinetic energy of the entering electrons and α is the entrance angle. Usually α is used as $\alpha^2 \simeq w/2R_0$, because of the desired large entrance slits which are used. Then eq. 2.25 becomes:

$$\frac{\Delta E}{E_0} \simeq 0.63\frac{w}{R_0} \tag{2.26}$$

For the detection of the electrons a 16–channel detector is used.

- **Electron Gun:** The features of the *electron gun* are 50 V-10 kV accelerating potential at a 5-8 nA sample current and 0.25 eV half-width of the signal. With the help of the *electron gun* which is attached to the spectrometer, one can perform EELS measurements.

- **Monochromator:** The function of the monochromator is based on the Bragg diffraction relation $n\lambda = 2d\sin\theta$ where λ is the wavelength of X-rays, d the crystal layer spacing, θ the Bragg angle and n is the diffraction order. An quartz crystal is used since for the first order diffraction of Al K_α radiation ($\lambda = 8.34\mathring{A}$) and $d = 4.255\mathring{A}$ spacing of the (100) planes, the Bragg relation yields an Al anode-crystal-sample angle of $23°$. The main characteristics of the monochromator are: focuses the radiation to a spot of 0.9 mm on the sample due to its toroidal shape, reduces the half-width to about 0.3 eV , eliminates the satellites of characteristic Al K_α radiations and improves the signal to background ratio. For this work all the XPS spectra were measured using monochromatic radiation from an Al anode with 12 kV accelerating potential and powered with 250 W.

- **Ion Gun:** Another device which belongs to the PHI 5600 spectrometer is the so called *Ion Gun*, which can be used when one desires to perform sputter-etching of the samples. The Ion gun, is using argon ions for this purpose. These can be accelerated up to 4.5 kV maximal potential with $3\mu A$ available ion-current over a 10 mm×10 mm scannable surface and a 100 μm focus. For the present work the Ion Gun was not used, because even for a low accelerating potential, this may induce drastic changes in surface geometry and stoichiometry [62].

- **Neutralizer:** When one is dealing with insulating samples local charges can occur on the surface of the samples which is leading to perturbation (shifts in the binding energy of the spectra) of the measurement. This can be avoided by using a low-energy electron gun to compensate the charging. The accelerating potential can be chosen between 0 and 10 V at maximal current of 25 μA.

- **Vacuum requirements:** An important aspect which needs to be taken into account is the conditions regarding the vacuum. For the XPS measurements, ultra-high vacuum conditions are requested, so that all components of the main and preparation chamber are kept under ultra-high vacuum during the experiments. There are two reasons why electron spectrometers used in surface analysis must operate under vacuum. In the first place electrons emitted from a specimen should collide with as few gas molecules as possible on their way to the analyzer so that they are not scattered and thereby lost for the analysis. The second reason to ensure that their mean free paths should be much greater than the dimensions of the spectrometer. Since in many experiments it is necessary to start with a well-characterized surface, either atomically clean or in some other stable conditions, and since even very small amounts of contaminant can affect the course of an experiment drastically, it is clearly necessary

to operate under conditions in which the rate of accumulation of contamination is negligible compared to the rate of change in the experiment. The principal source if contamination is the residual gas in the vacuum system. It was found that a base pressure of about 10^{-10} torr is adequate for the majority of surface experiments. This pressure is reached by employing a combination of appropiate vacuum pumps: turbomolecular, sputter and sublimation pumps. In order to accelerate the rate at which gas molecules resident on the inner walls leave the main chamber the temperature of the whole system must be increased to about $150^{\circ} - 200^{\circ}$C for several hours. A picture of the spectrometer on which the work was carried out in this thesis is presented in Fig. 2.13
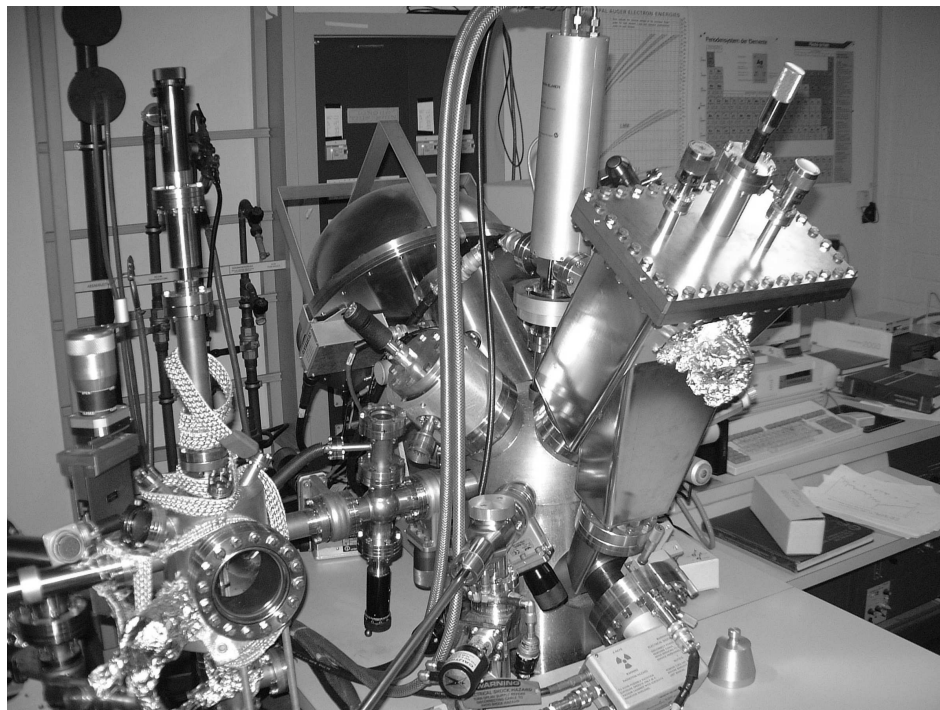
Figure 2.13: *PHI 5600 Spectrometer*

2.1.5.2   Calibration of the XPS Spectrometer

The accurate calibration of X-ray photoelectron spectrometers has been an important and continuing objective of spectroscopist over the years. Without an accurately defined spectral energy scale a full interpretation of the spectra gathered on different instruments is severely limited. Energy calibrations were reported by presenting binding energy tabulations for copper, silver and gold. These elements have the advantage of being easily cleaned and chemically inert as well as being stable conductors. For the purposes of calibration, binding energies are most accurately defined by referencing the zero to the Fermi level of conducting samples since this avoids errors arising from work functions differences

between spectrometers. The d bands of palladium and nickel provide suitably intense and sharp Fermi edges in order to define this zero. The literature calibration values of binding energies for copper, silver and gold defined in this way are given in Table 2.1. It is obvious

	Cu3p	Au4$f_{7/2}$	Ag3$d_{5/2}$	Cu2$p_{3/2}$	CuLMM (BE)	F.E. ref.
Schon (1972)	75.2 ± 1	84.0	368.2	$932.2 \pm .1$	$567 \pm .1$	Pd
Johansson *et al.* (1973)		$83.8 \pm .2$	$368.2 \pm .2$	$932.8 \pm .2$	$568.35 \pm .2$	Pd
Asami (1976)		84.07	368.23	932.53	567.97	Pd
Richter and Peplinski (1978)		84.0		932.7	568.25	Pd
Wagner, Gale and Raymond (1979)		83.8	367.9	932.4	567.9	Au4$f_{7/2}$
Powel, Erickson and Madey (1979)	75.1	84.0		932.6	567.9	
Fuggle and Mortensson (1980)	75.1	83.7	367.9			–
Lebugle *et al.* (1981)	75.13	84.0	368.2	932.57		–

Table 2.1: *XPS calibration binding energies (eV) from the literature*

that the accumulated data in this table show a variability of about 0.3 eV which, surprisingly has not reduced through the years. The most significant error of around 0.3 eV is due to positioning of the zero point. The random error of about 0.1 eV shows the measurement repeatability. Finally, the voltage scaling of the spectrometer introduces errors of approximately 500 p.p.m or 0.5 eV at 1000 eV binding energy. Binding energies of copper and gold referenced to the nickel Fermi edge were determined on the NPL spectrometer and represent the first accurately traceable calibration of binding energies. The binding energies for both Al K_α and Mg K_α radiations are listed in Table 2.2 [5] [6] [7].

	AlK_α	MgK_α
$Cu3p$	75.14 ± 0.02	75.13 ± 0.02
$Au4f_{7/2}$	83.98 ± 0.02	84.00 ± 0.01
$Ag3d_{5/2}$	368.27 ± 0.02	368.29 ± 0.01
CuL_3MM	567.97 ± 0.02	334.95 ± 0.01
$Cu2p_{3/2}$	932.67 ± 0.02	932.67 ± 0.02
AgM_4NN	1128.79 ± 0.02	895.76 ± 0.02

Table 2.2: *XPS calibration binding energies (eV)*

---

[5] Al K_α-Mg K_α=233.02eV
[6] Au4f$_{7/2}$ Al K_α BE lowered by Au4f$_{5/2}$ tail
[7] Ag 3d$_{5/2}$ Mg K_α BE raised by Ag 3d$_{3/2}$ X-ray satellite

2.2   X–ray Absorption Spectroscopy (XAS)

A more complex characterization of the electronic structure can be achieved with the help of other x-ray spectroscopic investigations. X-ray absorption spectroscopy (XAS) is one of the methods which can provide this characterization. The principle of x-ray absorption spectroscopy is related to the excitation of an electron from a core level into an empty state (conduction band). Moreover, using tunable synchrotron radiation one can induce desired absorption from a give core-level on the first unoccupied states above the Fermi level. Regarding the fact that core-level energies are unique the absorption edges will appear at certain energies of incident X-rays thus making XAS a valuable element sensitive tool for investigation of unoccupied states. A schematic representation of the XAS process is presented in Fig. 2.14. The transition probability in the XAS process is
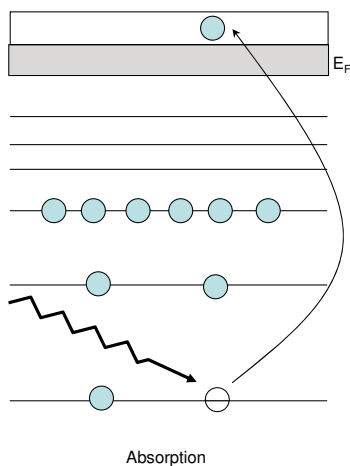
Figure 2.14: *Schematic representation of XAS*

described by Fermi's golden rule:

$$I_{XAS} \sim |< \psi_f \mid \hat{e}r \mid \psi_i >|^2 \ \delta(E_f - E_i - h\nu) \tag{2.27}$$

The intensity of the XAS in equation 2.27 is proportional to the squared dipole matrix element $\hat{e}r$ between the initial ψ_i and final state ψ_f. Because of the dipole selection rules only transitions which change the angular momentum quantum number *(l)* by one, $\Delta l = \pm 1$, occur in the XAS process. While the spin is conserved, $\Delta s = 0$, the orbital momentum of the z component has to change by zero or one, $\Delta m = \pm 1, 0$. Particular cases are for $\Delta m = 1$ for left circular polarized light and $\Delta m = -1$ for right polarized light. The x-ray absorption spectra can be divided into two spectral regions one is the *near edge x-ray absorption fine structure (NEXAFS)* which reflects excitations of the photoelectron into the unoccupied states and the other one is the *extended x-ray absorption fine structure(EXAFS)* where the photoelectron is excited into the continuum and its scattering

with the environment of the absorber leads to characteristic features in the XAS, usually at photon energies well above the corresponding NEXAFS threshold [63].

2.3   X-ray Emission Spectroscopy (XES)

After the absorption process the system will be left in an exited state with a core hole, and it can decay through different deexcitation channels. The first process which can occur is the Auger process (see Fig. 2.10), leading to the ejection of an electron. Another possibility is that the photon generated in the core-hole filling step will leave the solid without suffering scattering processes i.e. flourescence or emission processes and its energy can be recorded. By tuning the detector on the energy difference between the valence band and the core-level with a hole, only these decays will be recorded i.e. an element specific spectroscopy of the density of the occupied states. A schematic representation of the process is given in Fig. 2.15. The emission is dominated by the dipole selection rules
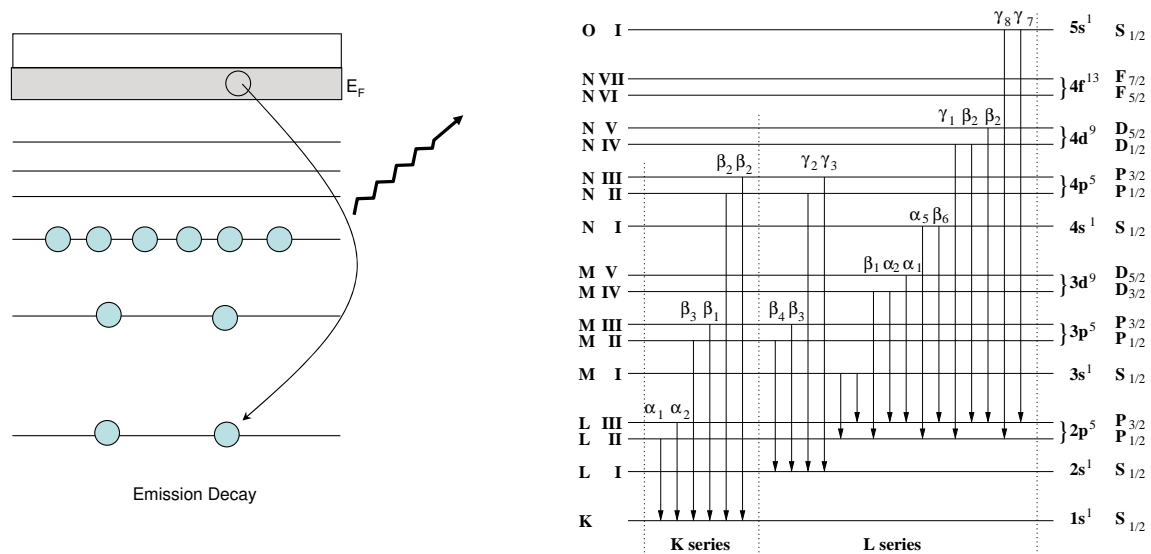
Figure 2.15: *Schematic representation of XES process and possible emission transitions of the K and L series*

$\Delta l = \pm 1$ and $\Delta j = \pm 1; 0$, when only the electric dipole vector of the radiation is taken into consideration. The probability of ion relaxation via dipolar emission is more than two times larger than that corresponding to the electric quadrupoles or to the magnetic dipole vector, therefore the last two can be often neglected, particulary in the case of normal x-ray emission spectroscopy (NEXAFS) [10].

2.3.1   Resonant X-ray Emission Spectroscopy (RXES)

Photon in-photon out, is the name of the method (XES) when one takes into account the excitation by a photon. As an example we are considering the x -ray scattering process in which a photon with energy Ω and a corresponding wave vector k_1 excites a material and as a result another x-ray photon with energy ω and a wave vector k_2 is emitted due to deexcitation process. The x-ray scattering cross section is described by the Krameres-Heisenberg equation [64, 65]:

$$F(\Omega, \omega) = \sum_f \left| \sum_m \frac{\langle f|T|m \rangle \langle m|T|i \rangle}{E_i + \Omega - E_m - m\Gamma_m} \right|^2 \cdot \delta(E_i + \Omega - E_f - \omega) \qquad (2.28)$$

$|m\rangle$ and $|i\rangle$ represent the intermediate state and initial state with energies E_m and E_i, respectively. E_f and $|f\rangle$ energy and final state configuration. The transition operator is denoted by T while Γ describes the spectral broadening which is due to the core life time. When the final state is the same as the initial state than the spectra described by equation 2.28 corresponds to resonant elastic x-ray scattering (RXES), while if the final state is different from the initial state, this will give the resonant inelastic x-ray scattering (RIXS). These two cases combined will give the overall resonant x-ray emission spectrum (RXES). The analysis of x-ray absorption and resonant x-ray emission spectra can be well achieved with the help of the energy-band theory. The energy-band model could not be often used successfully to describe the RIXS of d and f electrons. For these cases the single impurity Anderson model is widely used to analyze first order core level spectra i.e. XAS, XPS and RIXS of d and f electron systems [66, 67]. For the case of the $3d$ transition metal compounds the situation is a bit more complicated. The wave function of a $3d$ transition metal ion is more extended than the $4f$ wave function of a rare earth atom, for this reason the $3d$ electrons are more sensitive to the local atomic arrangement around the transition metal element. In Fig. 2.16 is presented the RIXS process by an energy level diagram.
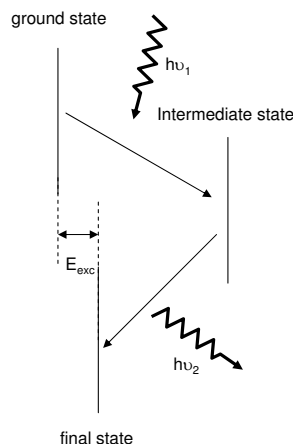
Figure 2.16: *Schematic representation of the RIXS process in an atomic like environment*

In the RIXS process the final state has the same parity as the initial state and for this reason, the so-called crystal field excitations between d orbitals of different symmetry are allowed. Besides low energy excitations in the RIXS spectra charge transfer (CT) process occur due to transitions between delocalized ligand and localized transition metal atom states. During the RIXS process energy conservation is valid from which one can obtain information about the ground state of the system via the intermediate core excited states. In this case the excitation energy of the final state E_{exe} is given by:

$$h\nu_2 = h\nu_1 - E_{exe} \tag{2.29}$$

where $h\nu_1$ and $h\nu_2$ denote the energies of the incident and scattered photons, respectively.

2.4 Instrumentation (XAS/XES)

2.4.1 Synchrotron experiments/Beamline and endstations

To be able to perform x-ray absorption and x-ray emission spectroscopy, high intensity and tunable x-ray sources are needed. X-Ray Absorption and (R)X-Ray Emission experiments are usually preformed with the highly brilliant and tunable light produced at synchrotron radiation facilities. The results in this thesis were obtained by using different beam lines equipped with complementary experimental end stations.

The x-ray emission spectra were measured at the ID 12 beamline at BESSY II in Berlin. The beam line is based upon a 41 mm period length undulator providing linearly polarized photons in the horizontal plane of the laboratory. The generated radiation can be monochromatized by three interchangeable SGMs. The spectral resolution can be selected with the help of the entrance slits. The spectra were recorded at the ROtable Spectrometer Apparatus (ROSA) endstation equipped with a soft x-ray spectrometer developed by Nordgren *et al.* [68].
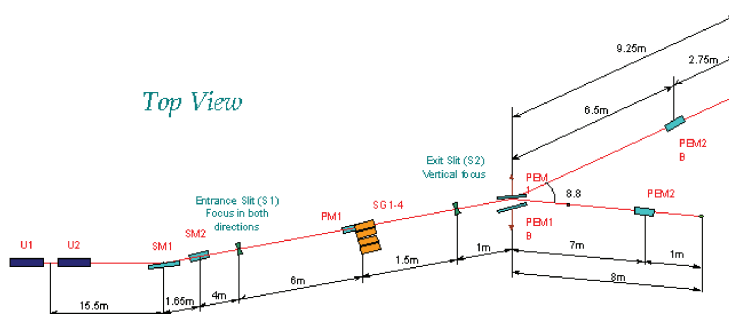
Figure 2.17: *Example of undulator beamline layout: BACH beamline at ELETTRA-Trieste Italy*

The X-ray absorption and resonant X-ray emission experiments were performed at the Beamline of Advanced diCHroism (BACH) at ELETTRA, Sincrotrone Trieste, Trieste, Italy (see Fig. 2.17). Two APPLE type helical undulators deliver x-rays over a wide range from 20-2000 eV with variable polarization, and the generated radiation can be monochromatized by four interchangeable SGMs . Two separate branches after the monochromator allow setting up two independent experimental chambers. The photon flux in the experimental chambers, calculated at the best resolutions achievable and with the aperture of the slits set at 10 μm is expected to be above 10^{11} photons/sec with linearly or circularly polarized light. In addition, a high flux grating in the 400-1600 eV range provides a higher flux, 10^{12} photons/sec with smaller resolving power allowing fluorescence and X-ray scattering experiments. The refocusing sections, based on plane elliptical mirrors in a Kirkpatrick-Baez scheme provide, a nearly free-aberration spots on the sample, whose dimensions are expected to be 200×310 μm^2 [69].

Another type of spectrometer is available, the so-called *Compact Inelastic X-ray Spectrometer* (ComIXS). The spectrometer is based upon a charged couple device (CCD) as a detector, providing very high count rates and the possibility to keep the spectrometer gratings very compact (see Fig. 2.18).
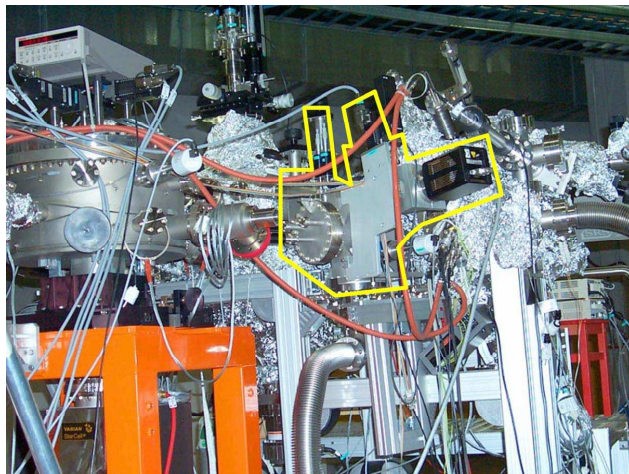
Figure 2.18: *Compact Soft Inelastic X-ray Spectrometer (ComIXS)-ELETTRA*

2.4.2   Storage ring /Inseration devices

The accelerator system for producing synchrotron radiation can be easily compared with a TV tube where electrons are emitted by a cathode (e.g. a hot filament) in high vacuum. The electrons are accelerated to an energy of 100 keV by an anode voltage of 100 000 Volts. The second accelerating stage is a microtron, the center part of which is a linear accelerator with a strong high frequency electrical field. The electrons pass through this field ten times as they are redirected on larger growing trajectories by a strong constant

magnetic field until they achieve an energy of 50 MeV. From here the electrons are passed into the vacuum chamber of the synchrotron accelerator: a closed system of tubes with a diameter of 4×8 cm^2 and ~ 96 m in circumference. The electrons are focused on a trajectory or orbit by strong magnets and are accelerated by the alternating field of a cavity resonator to the final energy of 1.7 GeV. The strength of the magnetic field is increased as the kinetic energy increases in order to keep the electrons on the correct trajectory as they approach to the speed of light. This cyclic acceleration occurs at a frequency of 10 Hertz, i.e. ten times per second some 10 billion electrons are accelerated to the final energy. Afterwards the electrons are injected via a transfer channel into the storage ring. The storage ring has a circumference of 240 meters. It is located in the center of the cylindrical building inside a radiation protection tunnel. The electrons circulating in the storage ring constitute an electric current. The maximum strength of the ring current is 0.4 A. This corresponds to roughly $2\times10^{1}2$ electrons circulating in the storage ring. The energy loss in the storage ring due to the emission of synchrotron light is compensated in each revolution by four cavity-resonators, which re–accelerate the electrons. This occurs through interaction inside
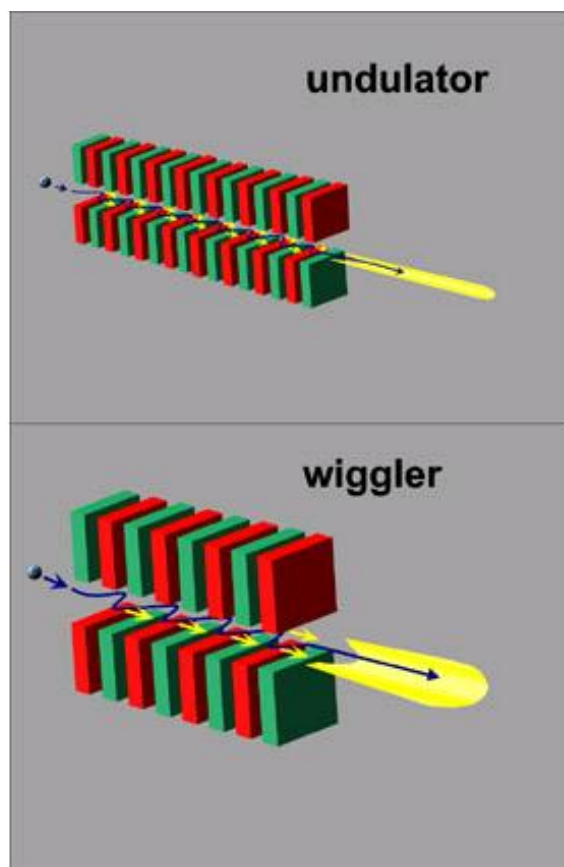
Figure 2.19: *Schematic drawing of an undulator and a wiggler (BESSY II, Berlin-Germany)*

the cavity–resonators with an electromagnetic field which oscillates at a frequency of 500

MHz. This oscillating acceleration forces the electrons in the ring into groups or bunches. Each time an electron bunch passes a radiation outlet in the ring (also called front end - leading to a beam line) a flash of "white" synchrotron "light" is visible.

More intensity and more light is one of the main request of the synchrotron users. However, this reduces the time necessary for measurements but, it also makes higher resolution feasible and enables smallest amounts of substances or several different physical quantities to be measured at the same time. Fig. 2.19 shows a drawing of the undulator and wiggler which are used at synchrotron facilities (this particular case is taken from BESSY II-Berlin).
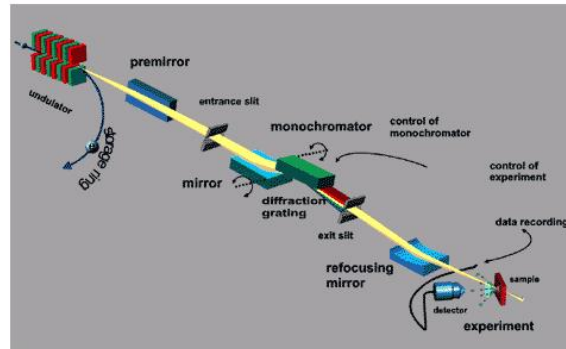
Figure 2.20: *Layout of the ROSA beamline at BESSY II*

In Fig. 2.20 is presented a typical path of the light beam from the source to the sample at BESSY II- Berlin [70].

Chapter 3

Why Molecular Magnets (Nanosized Magnetic Materials)?

Many technological aspects of everyday life are based on practical applications of the magnetic properties of the materials. Miniaturization is a key technological aspect; electronic circuits and storage devices are nowadays steadily decreasing in size and will eventually reach molecular dimensions. The field which is dealing with molecular magnetic materials is the so called *molecular magnetism*. *"Molecular Magnetism deals with magnetic properties of isolated molecules and/or assemblies of molecules"*[71]. *Molecular magnets* are relatively new born in the family of magnetic materials. However they are attracting increasing interest, since they exhibit many new properties which are difficult to be observed in classic magnets based on metallic or ionic lattices. The area of *molecular magnetism* is a strongly interdisciplinary one, where efficient collaborations have been established between chemists and physicists, the former designing new classes of molecular materials, the latter measuring the properties and developing theoretical models. At the beginning the synthetic effort was concentrated on the goal of obtaining purely organic magnets and of reaching critical temperatures above room temperatures. More recently chiral magnets have become the focus of attention, together with the design of materials showing the coexistence of conducting or superconducting behavior and magnetic properties. The results of the above efforts have been rather satisfactory, but recently is has been observed that large, but finite, magnetic molecules which can be considered as zero dimensional magnetic materials may be perfect testing ground for theories treating quantum effects in mesoscopic magnets. A class of molecules characterized by a large spin value in the ground state and large Ising type magnetic anisotropy show bistability of molecular origin, thus behaving as bulk magnets. One the other hand these molecules are still small enough to show large quantum effects, like tunnelling of the magnetisation and quantum interference effects.

At present it conveniently hosts many different activities involving methods of physical characterisation of matter : optical, X-ray, Mössbauer and neutron spectroscopies; scanning microscopies; and attracts physical methods of different degree of sophistication and abstraction [72]. The progress in this field is clearly driven by advances in chemical

synthesis of the materials and experiments.

Magnets are widely used in a large number of applications, and their market is larger than that of semiconductors. Information storage is certainly one of the most important uses of magnets and the lower limit to the size of the memory elements is provided by the superparamagnetic size, below which information cannot be permanently stored because the magnetization freely fluctuates [73]. In the future single molecules acting as nanosized magnets could be used in quantum computers or as storage media. In general, molecular magnetic materials have further advantages in terms of their synthesis at low temperatures and their processability. Molecular clusters of magnetic transition metal ions have been attracting increasing interest since the discovery that they can behave as nanomagnets and show bistability of pure molecular origin [74]. An important point is that the properties of magnetic particles scale exponentially, and therefore either it must be possible to address individual particles, or ensembles of absolutely identical particles must be available. This has been a challenge, but an attractive solution is given by the recent realization of molecules containing several transition-metal ions which can exhibit properties similar to nanoscale magnetic particles (nanomagnets). Such polynuclear metal complexes exhibiting superparamagnetic properties have been called *single-molecule magnets (SMMs)* [75]. Single-molecule magnets have attracted considerable interest in recent times. Although molecular, these species display superparamegnetic properties normally seen in mesoscale magnetic particles and thus can function as magnetizable entities below their blocking temperature. As a consequence SMMs represent the ultimate limit of miniaturization for data storage domains in magnetic media. Research into molecular magnetism, and the closely related field of molecular electronics, is only some tens of years old, but is very active. It has began in 1951 with the study of dinuclear complex, copper acetate, but it received a strong impetus in the 1980s with the discovery of the first molecular based-solids that exhibits spontaneous magnetization below their Curie temperature. Important discoveries have been made in these years, as it follows:

- the synthesis of the first bimetallic molecular magnets and organic magnets with the highest Curie temperature known so far;

- the synthesis of room-temperature molecular-based magnets;

- the discovery of spin-cross overs that occur with large hysteresis at room temperature;

- new photomagnetic processes, including light-induced excited spin-state trapping;

- the synthesis of the first molecular-based magnetic superconductor;

- the first characterisation of magnetic tunneling effect.

3.1   Origin of the Molecular Magnetism

The first *single molecule magnet* was discovered in 1993, it is the so called manganese twelve with the chemical formula: $[Mn_{12}O_{12}(O_2CCH_3)_{16}(H_2O)]\cdot 4H_2O\cdot 2CH_3CO_2H$ which is shown in Fig 3.1.

Variable field magnetization and high frequency electron paramagnetic resonance (HFEPR) data indicate that Mn_{12} has an $S=10$ ground state. The aniferromagnetic interactions between the $S=3/2$ spins of Mn^{IV} ions and the $S=2$ spins of Mn^{III} ions gives the large spin ground state for the Mn12 molecule. Another characteristic of the SMMs is the slow magnetization relaxation which is due to an individual molecule rather than to long range ordering as observed in nanoscale magnetic domains of bulk magnets.
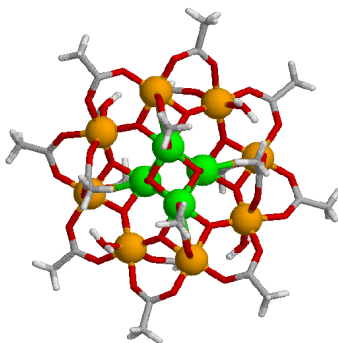
Figure 3.1: *$[Mn_4^{IV}Mn_8^{III}(\mu-O)_{12}]^{16+}$ core of $[Mn_{12}O_{12}(O_2CCH_3)_{16}(H_2O)_4]\cdot 4H_2O\cdot 2CH_3CO_2H$ showing the relative position of the Mn_{IV} ions (red ones), Mn_{III} ions (blue ones), and μ_3O^{2-} bridges: from [76]*

As an example, if Mn12 molecule is magnetized at 2K by applying a magnetic field and than removing the field, the relaxation of the magnetization is so slow that after two months the magnetization is still about 40% of the saturation (i.e., largest) value. At 1.5K, the half life for magnetization decay is hardly measurable because it is too long. If the external field is cycled to zero, the magnetization (M) is frozen by the presence of the barrier and only very slow tends to the equilibrium value (M=0)[73]. Thus a remanent magnetization is observed. A negative field reduces the height of the barrier and unfreezes the spins, thus allowing a rapid reversal of the magnetization. A hysteresis loop is therefore observed, which has a molecular and dynamical origin. The width of the loop (i.e. the coercive filed) depends on the temperature as well as the rate of sweep of the magnetic field.

The magnetic anisotropy of the ground state of Mn12 from the magnetic anisotropy of the eight Mn ^{III} ions. The bonding at each Mn ^{III} ion is such that two trans-bonds are longer than that of the other four (Jahn Teller elongation). When the single ion anisotropy is small, as in some Fe ^{III} clusters, the anisotropy originating from dipolar interactions is no longer negligible. In this case, ferrimagnetic planar structures are more suited to give an

easy axis magnetoanisotropy [77].

3.2 "Building" of SMMs

The desirable way to prepare SMMs is with large S values and with appreciable negative D values. Polynuclear metal complexes containing Fe, Mn, V and Cr have been shown to work as SMMs. The preparation of polynuclear complexes with large spin ground states is a formidable challenge to synthetic chemists [78]. In strong contrast to the predictive synthetic principles of organic chemistry, it is very difficult to prepare polynuclear metal complexes in a rational manner. In the known polynuclear single molecular magnets the metal ions are bridged by O^{2-}, OH^-, OR^-, RCO_2 or a combination or two or more of these units. As a conclusion there is no single strategy to prepare a molecule containing , for instance, 25 transition metal (TM) ions. Is is also considerable challenge to systematically build an SMM with an S=30 ground state. However with all this difficulties some strategies have been developed. A building-block strategy employing small complexes with two, three or four metal ions is one of the approaches. Regarding this approach, the relatively small building block complex is treated with a reagent that opens up one side of the complex by removing some of the organic ligands. As an example silicon forms strong Si-O bonds, so silicon containing reagents have been employed as RCO_2^- abstraction reagents, and this has often led to aggregation to a polynuclear product with more metal ions. As another approach, polydentate ligands that can form several bonds with one or more metal ions have been added to the building block complexes to cause aggregation and thus give larger complexes. Using this methodologies, it has been possible to prepare polynuclear Mn complexes with Mn_3, Mn_4, Mn_6, Mn_7, Mn_8, Mn_{10}, Mn_{12}, Mn_{18} and Mn_{30} compositions [78]. An important point in the "building" of the SMMs is the increase of the spin of the ground state, but it is not simply the number of metal ions in the molecule that determines the S value. Magnetic exchange interactions are propagated by the bridging of O^{2-}, OH^-, RO^-, or RCO_2^- ligands. Thus, it is necessary to arrange the metal ions and bridging ligands in an appropriate manner so that they give a high spin ground state for the polynuclear complex (so that the topology of the complex can be used to obtain a high spin ground state).

The formation of oxo-bridged polynuclear complexes of paramagnetic transition rare earth metal ions, derived from polyalcholato-ligands is poorly understood [79]. However, despite their unpredictable nature, oxo-bridged polynuclear iron- and manganese metal clusters have been the subject of numerous detailed spectroscopic and magnetic studies which have been rewarded by the discovery of the SMMs [77]. Recently, distinct supramolecular metal clusters have become accessible by rational design rather than serendipity [80]. In this context three examples of self assembly of six and eight membered iron-coronates [81]. The iron coronate $\{Na \subset [Fe_6[N(CH_2CH_2O)_3]_6]\}^+$ *(2)* and $\{Cs \subset [Fe_8[N(CH_2CH_2O)_3]_8]\}^+$ *(3)* with $Na \subset$[12]metallcrown-6 and $Cs \subset$[18]metallcrown-8 structure are prepared from triethanolamine *(1)* with iron (III) chlorid, sodium hydride or caesium carbonate, respectively (see Fig. 3.2).

What is common for the *(2)* and *(3)* complexes is that the μ_1-oxygens do not participate in the formation of the hexa- or octanuclear structures.
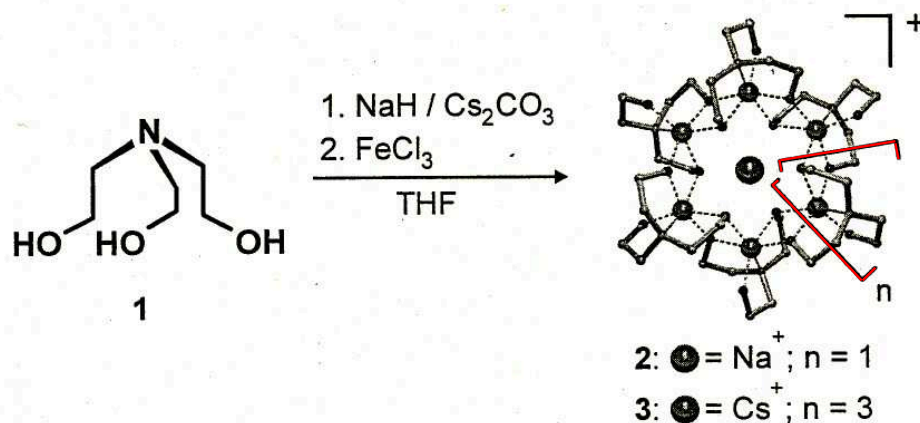
Figure 3.2: *(1)- Triethalolamine; (2) and (3)- Iron Coronates (from: [82])*

Regarding this, further mono-anionic donors, such as chlorid ions, could also be candidates for this function. Reaction of N- methyldiethanolamine *(4)* (H_2L^1) with calcium hydride and iron(III) chloride yielded the unoccupied neutral iron-cryptand $[Fe_6Cl_6(L^1)_6]$ *(5)* with Na$\subset$[12]metallcrown-6 structure (see Fig. 3.3)
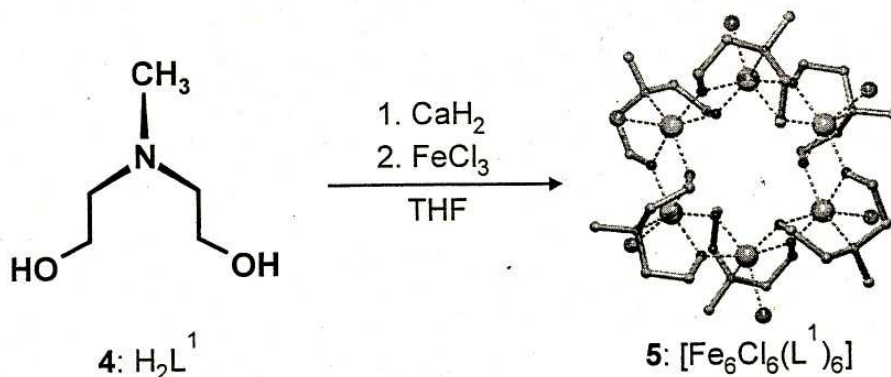
Figure 3.3: *(4)- N- methyldiethanolamine (5)- iron cryptand (from: [82])*

As a difference from the iron- coronates $\{Na\subset[Fe_6[N(CH_2CH_2O)_3]_6]\}^+$ and $\{Cs\subset[Fe_8[N(CH_2CH_2O)_3]_8]\}^+$, six- membered analogues of iron cryptate is visible. In the iron cryptate , the μ_2- oxygen donors of the N- methyldiethanolamine ligands are structure

determining, whereas their N-methyl groups are innocent and are exchangeable by various alkyl- and aryl- substituents. Another example is constituent out of (H_2L^2) *(6)* which reacts with N- iminodiethanol, calcium hydride and iron (III) chloride yielding an intermediate $[Fe_6Cl_6(L^2)_6]$ (7). Exchange of the chloride ions of (7) by bromide- or thicyanate ions afforded the unoccupied ferric wheels $[Fe_6Br_6(L^2)_6]$ (8) or $[Fe_6(NCS)_6(L^2)_6]$ *(9)* [82] (see Fig. 3.4). From X-ray crystallographic structure deter-
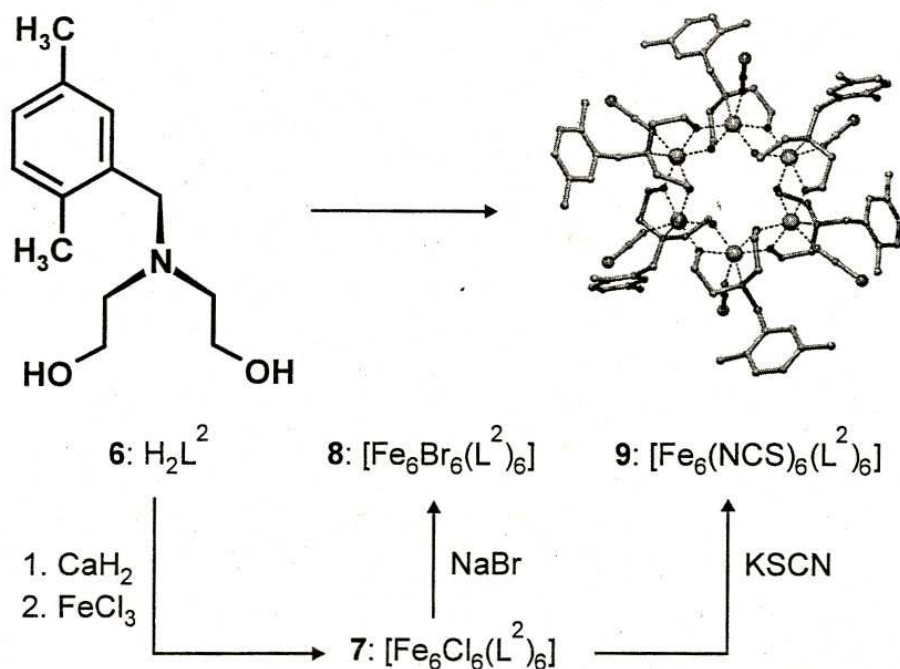
Figure 3.4: *Unoccupied neutral iron (III) complex with [12]metallacrown-6 structure (from: [82])*

mination, it was found that *(9)* is present in the crystal as unoccupied neutral iron (III) complex with [12]metallacrown -6 structure [82]. The six iron centers of the centrosymmetric molecule $[Fe_6(NCS)_6(L^2)_6]$ are located in the corners of an almost regular hexagon. The distorted octahedral coordination sphere of the iron centers compromise of two nitrogen donors (one from $(L^2)^{2-}$ and one from NCS^-) and four μ_2O donors. Thus the $[Fe_6O_{12}]$-cores of $[Fe_6Cl_6(L^1)_6]$ and $[Fe_6(NCS)_6(L^2)_6]$ are nearly superimposible.

A characteristic for the SMM's from magnetic point of view are the magnetic exchange interactions between magnetic centers.

Chapter 4

Ferric Star Single Molecule Magnet

4.1 Structure and Magnetic properties

Molecular clusters of magnetic metal ions showing single–molecule magnet behavior are being extensively studied due to their potential technological applications to new data storage systems [4]. These promising applications arise from their interesting physical properties such as magnetic bistability of pure molecular origin [74]. Such new molecular materials often arise from metal organic synthesis, which is the main driving force in studies of molecular magnets (see e.g., the monograph by Kahn [83] or Refs. [84, 85] for recent reviews). The present chapter is devoted to one such system, known as "ferric star", which is simple enough to allow an accurate study of its electronic structure, yet far from trivial for what regards its chemical manipulation (crystallization with different ligands) and physical treatment (e.g., deposition on surfaces). This synthesis of magnetic molecules

$$1/3\text{eq Fe}^{3+}$$

10: $[\text{Fe}(\text{L}^1)_2]^-$ **11**: $\{\text{Fe}[\text{Fe}(\text{L}^1)_2]_3\}$
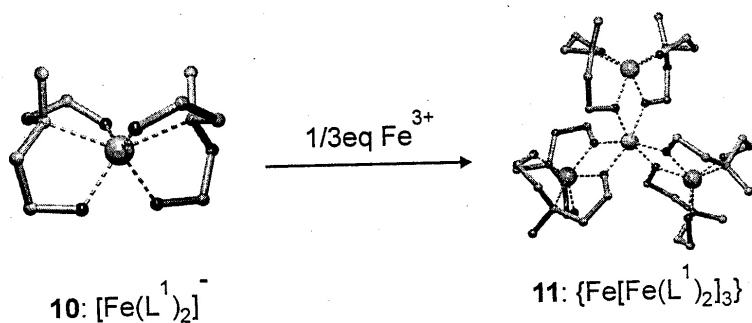
Figure 4.1: *Formation of the "ferric star" molecule (from: [82])*

with formula $\{M[\text{Fe}(\text{L}^1)_2]_3\}\cdot 4\text{CHCl}_3$ where L^1 is an organic ligand and M is Fe or Cr, has been described by Saalfrank *el al.* [82] (compounds **11** and **12** of this paper). Until now, little is known about the mechanistic aspects of self–assembling processes. More or less this was the method which was used in order to obtain the "ferric star" single molecule magnet. Careful titration of the dianion $(\text{L}^1)^{2-}$ with a solution of iron (III) chloride in the

THF afforded a colorless suspension of intermediate $[Fe(L^1)_2]^-$ with an iron/ligand ratio of 1:2 (see Fig. 4.1).

Further addition of iron (III) chloride to the colorless suspension of $[Fe(L^1)_2]^-$ up to an iron/ligand ratio of 1:1.5 resulted in gradual color change to a brown suspension. After this amber crystal were isolated and the tetranuclear cluster $[Fe\{Fe(L^1)_2\}_3]$ is generated. However, when two equivalents if iron (III) chloride is added to $[Fe\{Fe(L^1)_2\}_3]$, the known "ferric wheel" is generated. This process was shown to be reversible, when the "ferric wheel" is treated with three equivalents of $(L^1)^{2-}$, star–shaped cluster ("ferric star") was recovered. In the "ferric star" single molecule, the central atom is linked through two μ_2–alkoxo bridges from each of the three terminal building blocks $[Fe(L^1)_2]^-$. The center atom (Fe and Cr) is octahedrally coordinated through two nitrogen, μ_1–O, and μ_2–O donors. It is important to mention that during complexation of $(L^1)^{2-}$ to iron, nitrogen becomes stereogenic center [82].
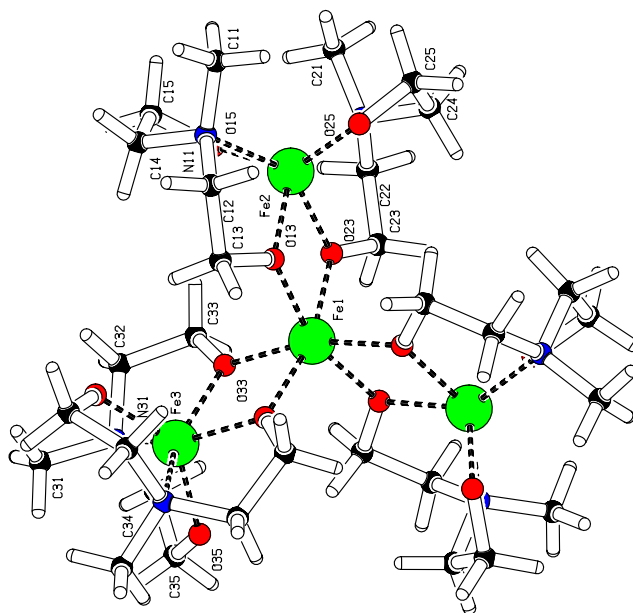
Figure 4.2: *Crystallographic structure of the Ferric Star Single Molecule Magnet*

Regarding the geometry of the "ferric star" molecule, all the transition metal ions are located in a plane, having the Fe–M–Fe (where M= Fe, Cr) angles of about $120°$ (see Fig 4.2). The crystallographic structure of this molecule is presented in Fig. 4.2 having as a transition metal in the middle of it's structure the Fe atom. Previous magnetochemical investigations of the "ferric star" molecule [86] indicate that the three spins $S=5/2$ of peripheral Fe ions at the star edges couple with an antiparallel orientation to the central ion, yielding (for $M=$Fe) the magnetic ground state of $S=5$. In this chapter the main issue is to clarify the electronic structure, as it emerges from a combined spectroscopic study and first–principle calculations. Specifically core–level excitations were probed on the "ferric

star" at the L and other edges by several core spectroscopies, namely near–edge X - ray absorption spectroscopy (NEXAFS), resonant inelastic X - ray scattering (RIXS) and X - ray photoemission spectroscopy (XPS). The electronic structure calculations presented in this chapter were done from first principles within the density functional theory [1]. The spectra gives insight into the distribution of energy–resolved state densities within the valence band, which reveal the M 3d – O 2p hybridization, and into charge states of transition metal (TM) atoms. The calculations give estimates of local magnetic moments, spatial distribution of the spin density, and of magnetic interaction parameters.

As it was mentioned before, in the present chapter, the $FeFe_3$ and $CrFe_3$–stars systems are studied. The structure of a single molecule derived from crystal structure analysis can be seen in the left panel of Fig 4.3, while the spatial packing of the molecules crystallized
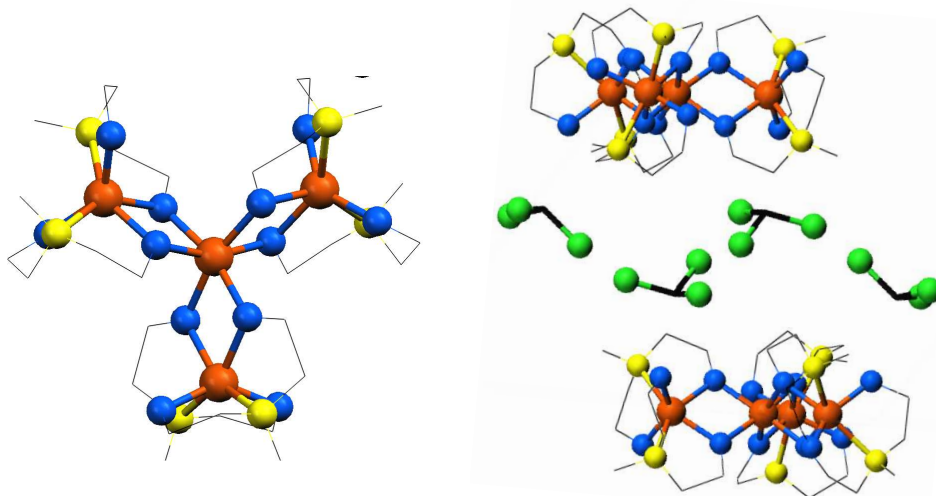
Figure 4.3: *Single "ferric star" molecule in the top view (left) and side view of the molecules packed in the crystal structure with chloroform (right). Hydrogen atoms are omitted, and carbon chains are shown as wireframe [87]*

from chloroform is shown in the right panel. As known from the literature, similar types of ferric stars with $FeFe_3$–framework can be synthesized using different ligands like dipival-oylmethane (Hdpm) in combination with methanolate or 1,1,1 – tris(hydroxymethyl)ehane (H_3thme), yielding respectively [$Fe_4(OMe)_6(dpm)_6$] [86] or [$Fe_4(thme)_{26}$] [88]. Contrary to the "ferric wheels" with even numbers of Fe atoms, which have zero spin in the ground state, in the "ferric star" the antiparallel coupling of three outer Fe spins to the central one results in a net ground–state spin $S = 3 \times 5/2 - 5/2 = 5$. For the magnetic anisotropy, the effective Hamiltonian of which can be conventionally written in the form :

$$H = DS_z^2 + E(S_x^2 - S_y^2) \tag{4.1}$$

in terms of the cumulative spin of the molecule, the axial parameter D is -0.20 cm^{-1} (-0.29K) from the high field electron spin resonance experiments [86, 77]. The absolute value of E (the sign may depend on the definition) was predicted by Kortus to be 0.064 K from a first principle calculation [89], and later estimated as 0.056 K in experiments by Müller *el al.* [90].

It has been recently demonstrated that the Fe in "ferric star" single molecule magnet can be substituted by other 3d ions. In this present chapter the spectroscopic study of Cr–doped "stars". The accuracy of the amount and position of the substitution has not yet been unambiguously established. For the *ab initio* calculations it was assumed the substitution in the central position, in an otherwise unchanged geometry. A more systemetic theoretical analysis of the electronic structure of "ferric stars" with substitution by different ions in different positions will be reported elsewhere [91].

4.2   Studies on the electronic structure

4.2.1   Specific experimental details

For the XPS measurements poly–crystalline samples were prepared and introduced in the main chamber under a basis pressure of about 5×10^{-8} mbar. Regarding the fact that the samples have an insulating character, during measurements the charging on the surface was compensated by employing low–energy electron gun. The parameters (electron energy and flux) were chosen in a convenient way in order to ensure a stable position of the most intensive core–level lines as well as a minimal full width at half minimum. In this particular case the line of C1s was chosen. Since tiny changes of surface's quality may influence its overall conducting properties thus requesting slightly modified parameters for the neutralizer profile–like measurements were performed. Because of the chemical instability (as conventional crystalline samples), these kind of spectra recording is recommended. The XPS spectra which are presented in this chapter, are a result of a careful sum of partial sweeps. Using this way of representing the XPS spectra allows the exclusion of partial spectra in case some changes of the observed features were noticed and prevents the inclusion of information which may mislead to the final interpretation. In order to ensure the surface quality of the sample during the measurements, and the stability check, survey spectra were recorded before and after the measurements.

4.2.2 Calibration of the XPS data

When non–conductive samples are studied by XPS technique, one problem which occurs is the calibration. As a reference line in the case of the "ferric star" molecule, the carbon 1s line was chosen. The XPS C 1s line of the "ferric star" is presented in Fig. 4.4 .
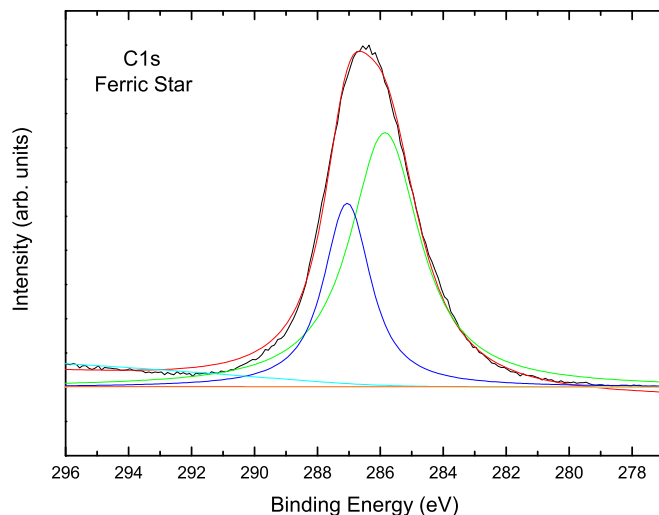
Figure 4.4: *XPS C 1s core–level of FeFe$_3$*

A fit was performed on the C 1s line, using Lorentz shapes for the peaks and a Tougaard–type form for the background. The Lorentz peaks were convoluted with a 0.6 eV Gauss line which accounts for the apparatus broadening. With the black line is denoted the experimental XPS line, while the red line denotes the fit for the C 1s line. The green and blue line denotes the two contributions one from carbon and oxygen respectively, to the total C 1s line from the "ferric star" molecule. A 2:3 area ratio was imposed as an restrictive condition, and in the same time a zero asymmetry was taken into consideration. The calibration was performed by assigning the C 1s line from the "ferric star" to 286.45 eV [92]. The C 1s line after which the calibration was performed is presented in Fig 4.5. The relatively high width of the C 1s line may be explained by taking into account the nature of the investigated samples. The most important reason is that related to their crystallinity. In contrast to samples which are monocrystals, the poly–crystalline samples present wider XPS lines. Another reason, which is also related to their crystallinity, may be because of their surface. In order to ensure an optimal charging compensation, the surface of the sample has to be uniform, which is not the case for the poly–crystalline kind of samples. In Fig. 4.6 a schematic representation is presented in order to explain this aspect. XPS active regions of the surface, where the low–energy electron beam is shadowed
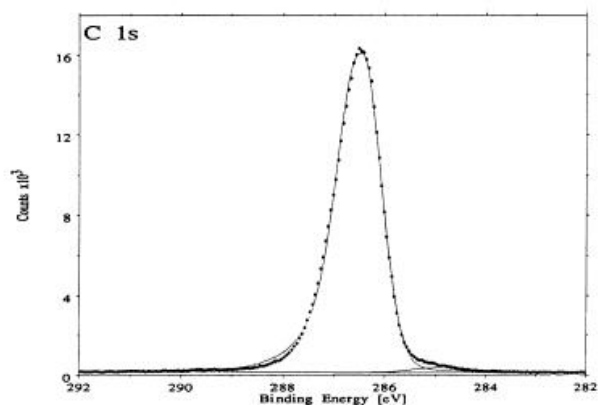
Figure 4.5: *XPS C 1s core–level of CH_2CH_2O from: [92]*
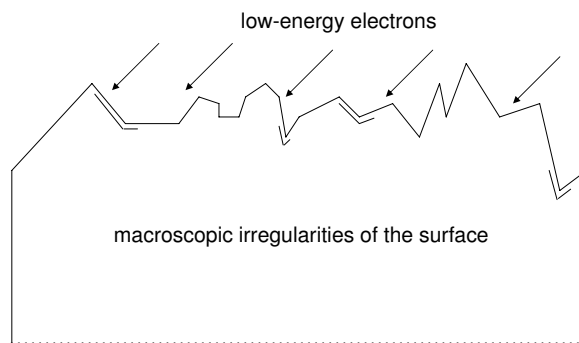
Figure 4.6: *Partial charge compensation in case of XPS measurements on unbalanced surfaces. Regions with deficient charge compensation are marked with double line (from [60])*

by irregularities could be responsible for low–intensity diffuse features situated at higher binding energy with respect to the main line. These structures can be observed for the $FeFe_3$ and $CrFe_3$ in the N 1s core–level lines as a result of a small shoulder at lower binding energies (see Fig. 4.7). The analysis of the spectra is not influenced by the presence of this shoulder since the area of this shoulder is below 5 % the sum of two material specific N peaks. As a conclusion of the related facts from above, one can say that the recording and analyzing of XPS spectra for metal–organic compounds is far for being trivial.
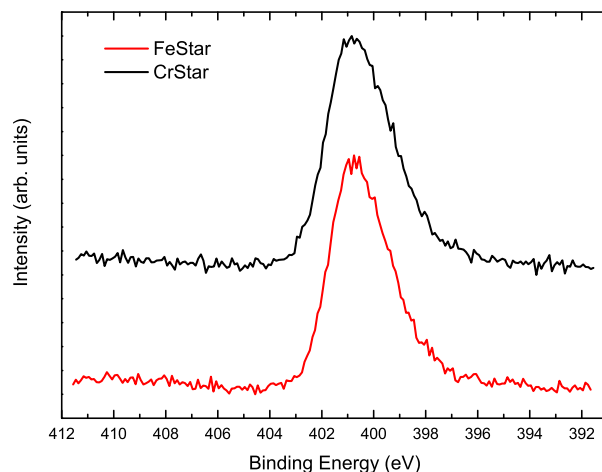
Figure 4.7: *XPS 1s core–level lines of N in MFe$_3$ (M= Fe,Cr)*

4.2.3 Core–level lines

The X-ray photoelectron of Fe (2p, 3s), C 1s, O 1s, and N 1s core levels spectra were recorded. These lines comprise information on the valence state, local magnetic properties and local electronic structure. Because of this points, they are of highly interest. It is important to specify that a good correlation between the organo–metallic materials and transition metal oxides does exists, and for this reason in the study of the core–level lines references to the transition–metal oxides will be brought. A comparison between these two classes of materials is appealing since the core–level lines of simple or complex oxides are nowadays well understood. Regarding the studies of the 2p and 3s XPS lines, these depend on different factors which are divided in intra– and extra–atomic features. The intra–atomic features are characteristic for the ionic species and may be compared between similar ions in two different compounds. The second features (extra–atomic) are specific for a particular material and depend on the local geometry of the first atomic neighborhood of 3d–metal. For the case of organo–metallic materials another important aspects are the screened final–states, where an electron is transferred from a ligand atom in order to screen the created core–hole. This aspect plays an important role in the shape of the XPS spectra. The extra–atomic features becomes evident for the configuration interaction cluster approach to the Anderson hamiltonian [93, 94]. The interplay between final states effects and exchange interaction or spin–orbit coupling can be estimated in the frame of Zaanen–Sawatzky–Allen diagram [95]. This classifies the transition metal compounds with respect to their ligand to metal charge transfer energy, the d–d Mott–Hubbard repulsion and bandwidths of metal and ligand states. For this reasons, the comparison of XPS transition metal core–level spectra coming from different classes of materials must be carefully defined.

In order to prof the quality of the samples which they were studied and to denote the

main lines, in Fig. 4.8 the survey spectra of the $FeFe_3$ and $CrFe_3$ are presented.
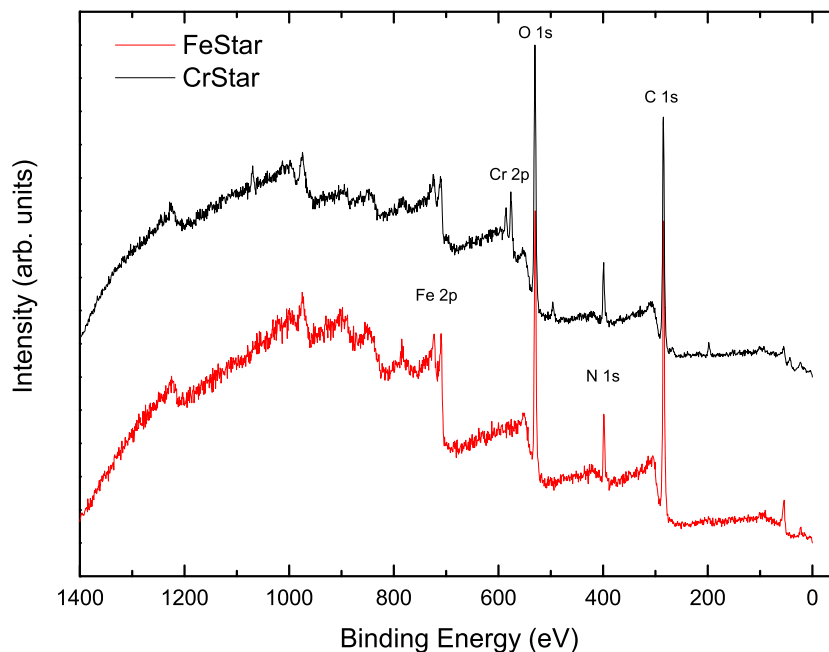
Figure 4.8: *XPS survey spectra of $FeFe_3$(FeStar) and $CrFe_3$(CrStar)*

The main lines are indicated in the spectra above, and the positions at which they appear are the expected ones.

It is essential to emphasize that bulk techniques (magnetization, magnetic susceptibility) probe the effective spin value, however without addressing its localization. The issue of localization – whether the spin S=5 relates strictly to the Fe ion only or extends over ligands – is related to that of nominal valence. Fe^{3+} presumes the maximum spin $3d_{\uparrow}^5 d_{\downarrow}^0$ configuration, whereas Fe^{2+} corresponds to local magnetic moment of 4 μ_B. Core–level spectroscopy, being an element–sensitive method, may permit one to distinguish between these two cases. Fig. 4.9 depicts the Fe $2p_{3/2}$ and $2p_{1/2}$ photoelectron spectra of the $FeFe_3$ and $CrFe_3$. Characteristic ligand–to–metal charge–transfer effects are present in the Fe 2p spectra of the FeStar, as well as in the spectra of CrStar. The relative positions and widths of the peaks due to the final state with charge transfer $2p^5 3d^{n+1}\underline{L}$ (A) and that without charge–transfer $2p^5 3d^n L$ (B) in the spectrum of $FeFe_3$ is similar to that of $CrFe_3$.

The absolute binding energy of Fe$2p_{3/2}$ line in $FeFe_3$ was found to be at 710.65 eV, which is higher than the value measured for $CrFe_3$ (710.45 eV). This reveals a higher degree of ionic character for the $FeFe_3$ as compared to the $CrFe_3$. In figure 4.10 the Fe 2p of the $FeFe_3$ and $CrFe_3$ is presented along with those of two benchmark, of well–known Fe^{2+} and
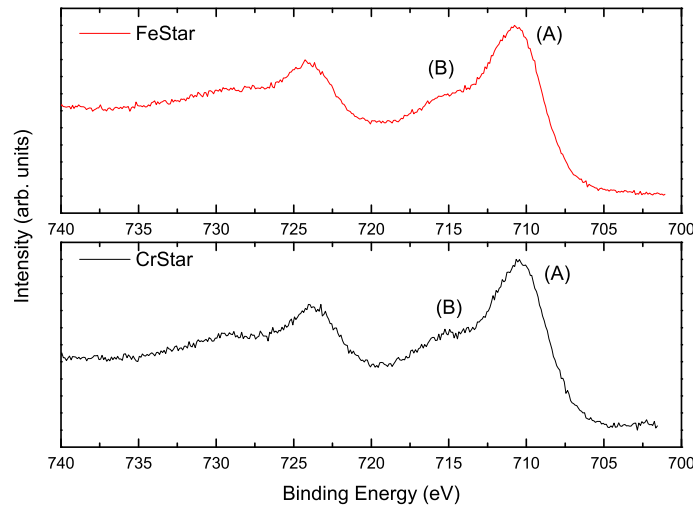
Figure 4.9: *XPS Fe 2p core–level lines of FeFe$_3$ respectively CrFe$_3$*

Fe^{3+} valence: FeO [96] and LiFeO$_2$ [97].
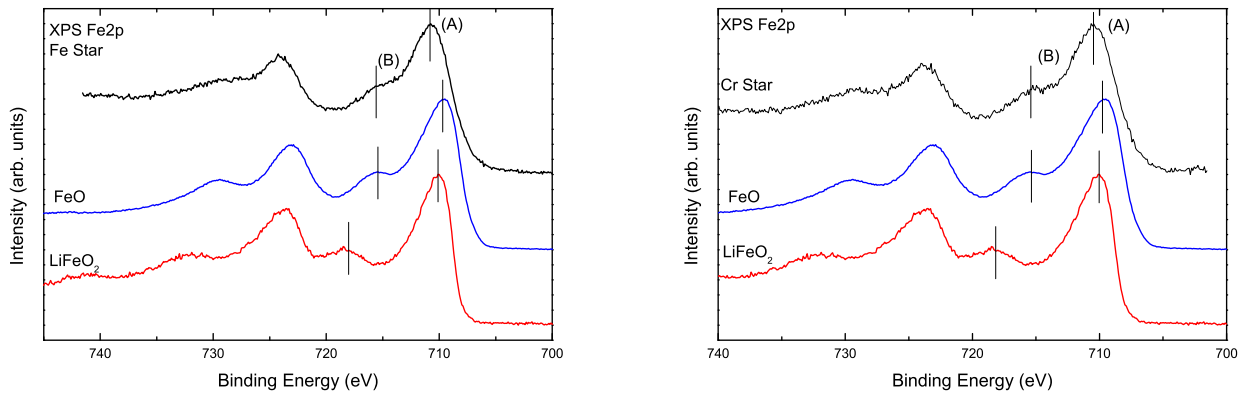
Figure 4.10: *Left panel: XPS Fe 2p(FeFe$_3$) comparison with FeO and LiFeO$_2$; Right panel: XPS Fe 2p (CrFe$_3$ comparison with FeO and LiFeO$_2$)*

As it was described before, charge transfer effects are present in the Fe 2p spectra for FeFe$_3$ as well for CrFe$_3$. The same features can be observed for the two cases taken from literature FeO an LiFeO$_2$. Yet there are some dissimilarities between these two reference systems. For both Fe 2p spectra from FeFe$_3$ and CrFe$_3$, the distance between the main line $(2p^5 3d^{n+1}\underline{L}$ (A)) and the peak due to final state without charge–transfer $(2p^5 3d^n \underline{L}$ (B))

is similar to that of FeO which indicates a clear Fe^{2+} valence state.

The Fe 3s core–level photoelectron spectra of the $FeFe_3$ and $CrFe_3$ is presented in Fig. 4.11
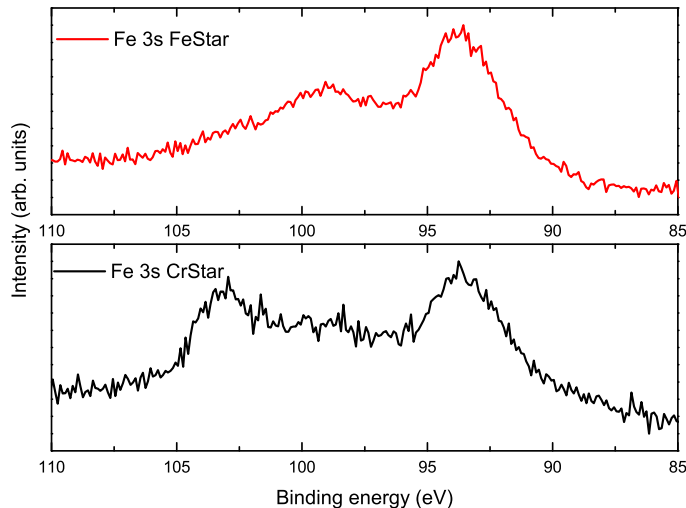
Figure 4.11: *XPS 3s spectra of iron in FeFe$_3$ (upper panel) and CrFe$_3$ (lower panel)*

As it was indicated in the XPS study of the 2p lines charge–transfer effects are present also in the 3s line. The Fe 3s spectra for both compounds are composed out of two main peaks. In the Fe 3s spectra of $CrFe_3$ a third peak appears at about 102 eV which has an intensity which cannot be described in the frame of 3s multiplet splitting theory an corresponds most probably to an impurity line. [2]

The intensities of two peaks in the Fe 3s spectra for both $FeFe_3$ as well as for $CrFe_3$ molecules, are far from the value expected $3d^5$ configuration, thus motivating some other configuration of peaks under the experimental curve. These facts, lead to the conclusion that the visual multiplet splitting exhibited by the 3s spectra does not directly reflect the value of the magnetic moment.

The 3s core–level photoelectron spectra of the $FeFe_3$, again in comparison with those of FeO and $LiFeO_2$, are shown in Fig. 4.12. As it was described before, the spectra of the $FeFe_3$ consists of two well separated peaks (a) and (c), according to whether the spin of the emitted 3s core electron is parallel or antiparallel to that of the 3d shell. Each of these peaks has a satellite denoted with (b) and (d), satellites which were assigned by Sangaletti and Parmigiani [98] to charge transfer excitations. Similar features are observed for FeO, with corresponding peaks labeled a', b', c' and d'. The Fe 3s ($FeFe_3$ & FeO) spectra were

---

[2]A possibility is that the impurity line can be associated to the silicon impurity, due to the chemical synthesis of the molecule
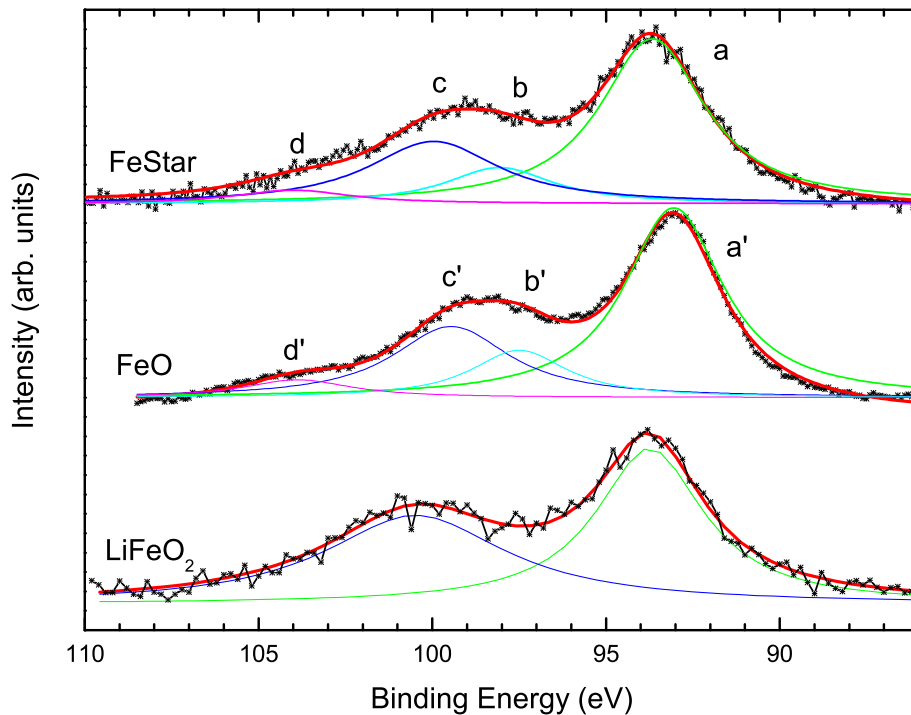
Figure 4.12: *Fe 3s photoelectron spectra of the Fe –"ferric star" in comparison with those of FeO (definitely Fe^{2+}) and $LiFeO_2$ (definitely Fe^{3+}). The features (a), (b), (c) and (d) are discussed in the text*

fitted with a Voigt function [38], by constraining the Gaussian widht to a value of 0.6 eV. The background was simulated by a Tougaard function [59], and subtracted from the spectra.

In $LiFeO_2$ the charge transfer is not prominent, therefore the fitting was done using two peaks only. The splitting is proportional to the number of the unpaired d electrons and hence to total spin S; the predicted relative intesities are given by the relation $S/(S+1)$ [99]. The value of the Fe 3s splitting in the case of $FeFe_3$ is about 5.10 eV; compared to 5.5 eV in FeO and 6.5 eV in $LiFeO_2$. A conclusion from this comparison can be drawn that the nominal valance Fe^{2+} is more plausible in the $FeFe_3$.

In table 4.1, the XPS binding energies from the main lines are presented.

	C 1s	N 1s	O1s	Fe $2p_{3/2}$	Cr $2p_{3/2}$
$FeFe_3$	286.4 eV	400.7 eV	531.9 eV	710.7 eV	–
$CrFe_3$	286.4 eV	400.8 eV	531.9 eV	710.4 eV	577.4 eV

Table 4.1: *XPS binding energies for the $FeFe_3$ and $CrFe_3$*

The core–level line of Cr 2p from the $CrFe_3$ was also recorded an it is plotted in Fig 4.13. The most striking feature of the chromium 2p spectra in comparison with the Fe 2p
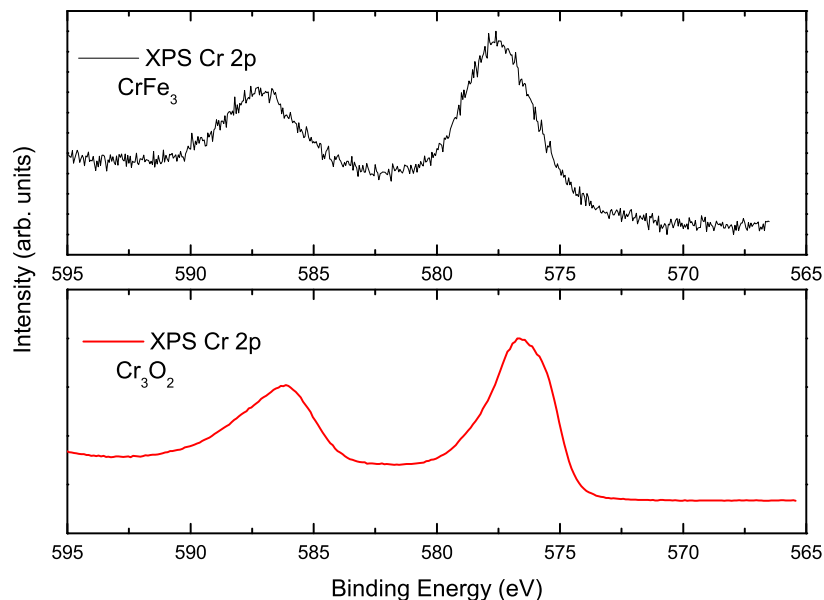
Figure 4.13: *XPS 2p spectra of chromium in $CrFe_3$ (upper panel) and Cr_2O_3 (lower panel)*

spectra, is the lack of significant charge–transfer features. This is similar to the case of Cr_2O_3, where the charge transfer effects have only a secondary role. Due to the fact that one can not see the charge–transfer satellites, it is difficult to estimate the valency of the Cr in the $CrFe_3$ molecule. For this reason, the XPS 3s line from Cr_2O_3 was chosen as a reference line. The Cr 3s spectra from the $CrFe_3$ is similar from this point of view: no charging–effects are present. So, for this reason the spectra can be fitted with two lines. All dow a third structure appears (at 82.65 eV) in the spectra of the Cr 3s, this seems to correspond most probably to a impurity line; however it has a intensity which can not be described in the frame of the 3s multiplet splitting (see Fig. 4.14). In the lower panel from Fig. 4.14, the XPS 3s line of the chromium from the Cr_2O_3 compound is presented. The value of the Cr 3s splitting in the case of the $CrFe_3$ is about 4 eV, which , compared to the splitting of the Cr3s from Cr_2O_3 is very similar. From this comparison one can predict that the valency of the Cr in the $CrFe_3$ after photoemission is Cr^{3+}, as it is known from the Cr_2O_3 compound [100]. This will give the $3d^3_\downarrow d_\uparrow$ configuration for the Cr.
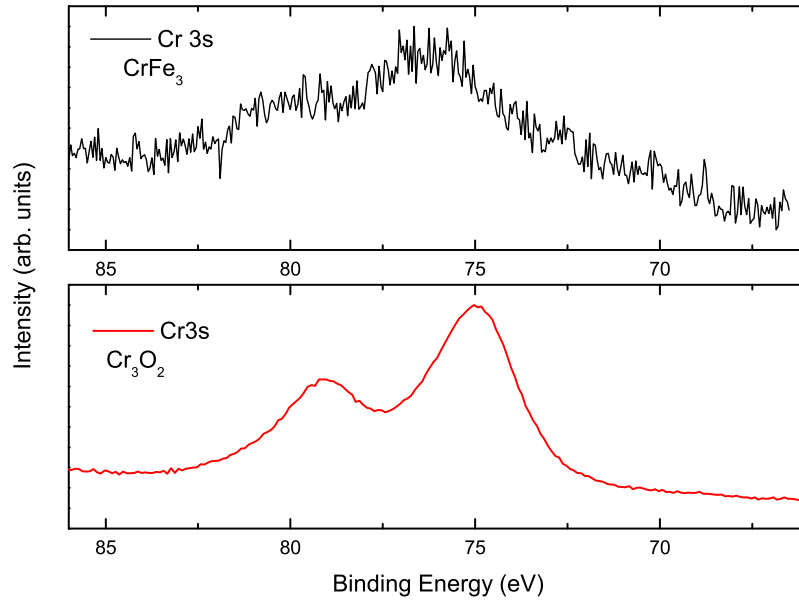
Figure 4.14: *XPS 3s core–level lines of chromium in CrFe$_3$ (upper panel) and Cr$_2$O$_3$ (lower panel)*

4.2.4   Calculation of the 3s multiplet line

In the following subsection it is proposed to study in a deeper way the structure of the 3s transition metal spectra and the extent screening effects of the FeFe$_3$ (FeStar) and CrFe$_3$ (CrStar) molecules. This can be achieved by employing an appropriate model for the multiplet splitting in insulating materials. The model which is used in order to study the structure of the 3s XPS spectra of the FeFe$_3$ was developed in Osnabrück, by Dr. V. R. Galakhov [101]. In order to present the above model, the physical values and the restrictions are presented as it follows. The multiplet XPS 3s spectrum represents a sum of magnetic exchange derived spin configurations. High–spin and low–spin states with or without charge transfer must be considered, since a charge transfer from ligand to metal ion accounts for screening the final 3s core–hole. This states are denoted as it follows: HS states :$| 3s^1 3d^n L; ^{2S+2}\Gamma\rangle$ and $| 3s^1 3d^{n+1}\underline{L}; ^{2S+2}\Gamma\rangle$, LS states: $| 3s^1 3d^n L; ^{2S}\Gamma\rangle$ and $| 3s^1 3d^{n+1}\underline{L}; ^{2S}\Gamma\rangle$. The ground state wave function Ψ_{ini} can be written in the form: $|\Psi_{ini}\rangle = \alpha_0|d^n\rangle - \alpha_1|d^{n+1}\underline{L}\rangle$ where $\alpha_0^2 + \alpha_1^2 = 1$. For the high spin–state configuration, the final–state wave function is written as: $|\Psi_{fin1}\rangle = \beta_0|s^1 d^n\rangle - \beta_1|s^1 d^{n+1}\underline{L}\rangle$; $|\Psi_{fin2}\rangle = \beta_1|s^1 d^n\rangle + \beta_0|s^1 d^{n+1}\underline{L}\rangle$. The eigenvalues are :

$$E_{1,2}^{HS} = \frac{1}{2}(U_{sd} - \Delta) \pm \frac{1}{2}\sqrt{(U_{sd} - \Delta)^2 + 4T^2} \qquad (4.2)$$

Δ represents the charge transfer energy, U_{sd} is the core–hole d electron Coulomb attraction energy, and T is the transfer integral, defined as follows:

$$U_{sd} - \Delta = \langle s^1 d^n | \hat{H} | s^1 d^n \rangle$$

$$T = \langle s^1 d^n | \hat{H} | s^1 d^{n+1} \underline{L} \rangle \tag{4.3}$$

The exchange energy for the $s^1 d^n$ final states is defined as ΔE_{ex}^n and for $s^1 d^{n+1} \underline{L}$ as ΔE_{ex}^{n+1}. Regarding this, the eigenvalues for the low–spin configuration are:

$$E_{3,4}^{LS} = \Delta E_{ex}^{n+1} + \frac{1}{2}\left[(U_{sd} - \Delta) + (\Delta E_{ex}^n - \Delta E_{ex}^{n+1})\right] \pm \frac{1}{2}\sqrt{\left[(U_{sd} - \Delta) + (\Delta E_{ex}^n - \Delta E_{ex}^{n+1})\right]^2 + 4T^2} \tag{4.4}$$

The α_0, α_1, β_0 and β_1 coefficients are determined from: $\alpha_0 = \cos\theta_0$, $\alpha_1 = \sin\theta_0$, $\beta_0 = \cos\theta_1$ and $\beta_1 = \sin\theta_1$, where:

$$\tan 2\theta_0 = \frac{2T}{\Delta} \tag{4.5}$$

$$\tan 2\theta_1 = \frac{2T}{\Delta - U_{sd}} \tag{4.6}$$

The ratio intensity for the high–spin configuration of the satellite to the main line is given (in the sudden approximation) by:

$$\frac{I_2^{HS}}{I_1^{HS}} = \frac{|\langle f_2 | g \rangle|^2}{|\langle f_1 | g \rangle|^2} = \frac{(\alpha_0 \beta_1 - \alpha_1 \beta_0)^2}{(\alpha_0 \beta_0 + \alpha_1 \beta_1)^2} \tag{4.7}$$

For the low–spin configuration, it is necessary to determine the contributions of both, the $s^1 d^n$ and $s^1 d^{n+1} \underline{L}$ configurations forming the main line and the satellite. The intensity for the main line for the low–spin state is given by:

$$I_3^{LS} = I_1^{HS}\left(K^{n+1}\beta_1^2 \frac{S^{n+1}}{S^{n+1} + 1} + k^n \beta_0^2 \frac{S^n}{S^n + 1}\right) \tag{4.8}$$

and for the satellite:

$$I_4^{LS} = I_2^{HS}\left(k^{n+1}\beta_0^2 \frac{S^{n+1}}{S^{n+1} + 1} + k^n \beta_1^2 \frac{S^n}{S^n + 1}\right) \tag{4.9}$$

For the $3s^1 3p^6 3d^n$ — $3s^2 3p^4 3d^{n+1}$ and $3s^1 3p^6 3d^{n+1}$ — $3s^2 3p^4 3d^{n+2}$ configuration interactions, the k^n and k^{n+1} coefficients are used. The sum of the 3s line is obtained by a convolution of the calculated line spectrum with the function:

$$I(E) = \frac{I_0 \gamma^3}{[(E - E_0)^2 + \gamma^2]^{1.5}} \tag{4.10}$$

where E_0 is the energy of the lines corresponding to each of the configuration contribution, and I_0 is the intensity of the lines. γ is a value for the convolution (intermediate between Lorentzian and Gaussian). The model is schematically drown in Fig 4.15.
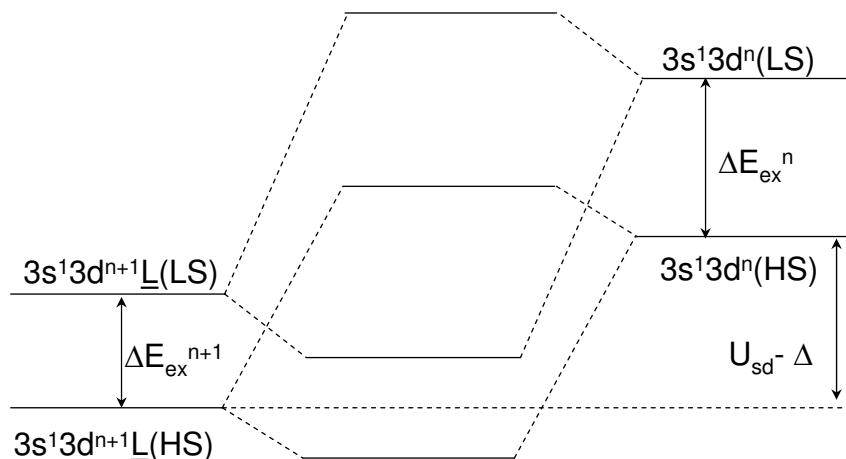
Figure 4.15: *Energy diagram for presenting the configuration mixing (from [101])*

As it was described above, two states are considered for $3s^1 3d^n$ as well as for $3s^1 3d^{n+1}\underline{L}$ (high–spine and low–spin). Each of these states with the energy E^{HS} or E^{LS} mixes with the other with the same spin, this leads to the reduction of the multiplet splitting depending on the covalent mixing in the final state. This is a two level model employed separately to high–spin and low–spin states.

The calculated $3s$ spectrum for FeFe$_3$ is presented in Fig. 4.16 together with the experimental data. The experimental spectrum is corrected for the background arising due to the secondary electrons. U_{sd} (the core–hole d electron Coulomb attraction energy), Δ (the charge–transfer energy) and T (the transfer integral) used for the calculations are presented in Table 4.2.

	U_{sd} (eV)	Δ (eV)	T (eV)	α_1^2	β_1^2
FeFe$_3$–star	5.26	6.8	2.3	0.09	0.39

Table 4.2: *Parameters used to calculate the 3s–XPS spectrum for the FeFe$_3$–Star molecule*
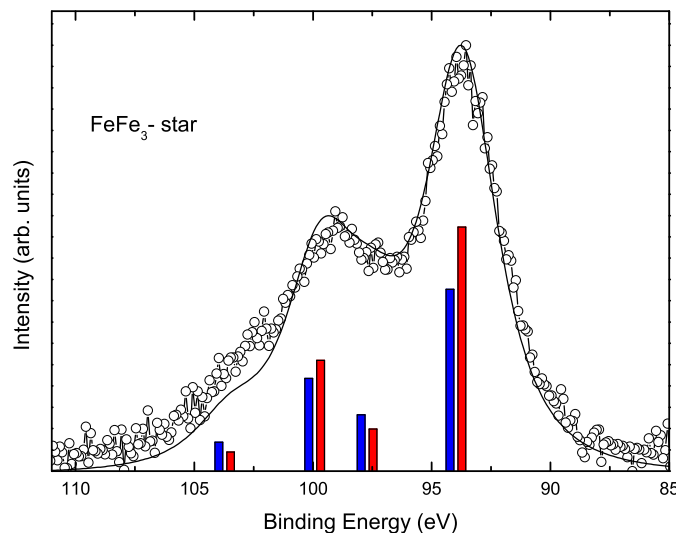
Figure 4.16: *XPS spectrum (circles) and model calculation (continuous line) of the 3s core levels (FeFe$_3$)*

The lower parts of the calculated 3s spectrum shows $3s^1 3d^n$ and $3s^1 3d^{n+1} \underline{L}$ contributions forming the main line and satellites, both high–spin and low–spin configurations. The magnitude of the exchange splitting depends on the hybridization parameters. By comparing the above result with the calculated spectra of some selected transition–metal oxides [101], one can see that a large value of Δ, reflects a strong ionic character. Regarding the calculated 3s core–level of FeFe$_3$–star, we can say that the contribution is mainly given by the $3s^1 3d^7 \underline{L}$ and $3s^1 3d^6$ states. The contributions from the $|3s^1 3d^{n+1} \underline{L}\rangle$ are quite visible, due to the moderate value of the charge–transfer energy (Δ). This allows a higher mix with screened final states. Energetically speaking , it is easier to transfer electrons from the ligand (oxygen atoms) to the metal ion (iron atoms). On the scale of atomic orbital energies the lower U_{sd} value is due to the non–zero occupancy of spin–down 3d orbitals of iron which makes the further population of spin–down states to be more accessible [60]. The value of the measured splitting in the case of the 3s line from the FeFe$_3$–star molecule, is a value of the magnetic exchange interaction, because of the value of the charge–transfer, which is not low enough to generate high contributions of final states with charge–transfer wight. The U_{sd} value obtained, gives also the valency of Fe^{2+} as it was found to be in the previous subchapter. This two–level model which was used to calculate the 3s splitting of the Fe from FeFe$_3$–star allows to explain the 3s splitting of the transition–metal which is "incorporated" in the present single molecule, as a function of the number of the 3d electrons in the ground state. We can conclude that the 3s spectrum of the Fe from the FeFe$_3$ exhibits four peaks, and the final state configuration is described mainly by the screened $3s^1 3d^n$ and $3s^1 3d^{n+1} \underline{L}$ states.

For the case of the Fe $3s$ line of $CrFe_3$, the calculation of the $3s$ splitting was a bit difficult. As it was mentioned in the previous subsection, a feature at about 103.05 eV appears which seems to be an impurity (see Subchapter 4.2.3). For this reason I have chosen a different simulating program in order to "build up" the $3s$ core–level line of the $CrFe_3$. A proper numerical approach which is also based on the Dr. V. R. Galakhov's model, was used. This numerical approach was developed in our research group by Dr. S. G. Chiuzbaian. The fit consists from two steps : first a proper starting point is found in the limits of physical constrains by means of Monte–Carlo approach; secondly the values of the parameters are refined in an adapted non–linear Levenberg–Marquardt method [102]. The peaks used for the fitting are composed out of a Lorenz–Gauss product. The free mixing parameter which was used is presented in equation 4.11:

$$f(\epsilon) = I_0 \left\{ 1 + m \left[\frac{\epsilon}{(\gamma/2)} \right]^2 \right\}^{-1} \cdot exp \left\{ -(1-m)ln2 \left[\frac{\epsilon}{\gamma/2} \right]^2 \right\} \tag{4.11}$$

where m is the Lorenzian–Gaussian mixing ratio. The Monte–Carlo procedure was run with approx. 500.000 points in the parameter space. The figure of merit function that measures the agreement between data and model was chosen in a normalized metric distance form [60, 103]:

$$\chi = \frac{1}{\sqrt{2}} \sqrt{\sum_{i=1}^{n} \left(\frac{y_i}{|y|} - \frac{F(y_i)}{|F|} \right)^2} \tag{4.12}$$

where y_i are the experimental points and F is the model function.

$$|y| = \sqrt{\sum_{i=1}^{n} y_i^2} \tag{4.13}$$

The nature of the experimental points from an XPS spectrum, is the reason for using this form. A higher number of counts, reflects a better spectrum i. e. a lower detection giving error. The reduction of exchange energy over the value of free ion was accounted for final states with or without charge–transfer with two fit parameters (k^n and respectively k^{n+1}). The fitting parameters which were used in order to obtain the calculated $3s$ line of the $CrFe_3$–star are presented in Table 4.3

	Δ (eV)	Q_{sd} (eV)	T (eV)
$CrFe_3$–star	4.056	6.23	4.707

Table 4.3: *Parameters used to calculate the Fe 3s – XPS spectrum for CrFe_3–star molecule*

The fitted spectra of the Fe $3s$ from $CrFe_3$ – star, is presented in Fig. 4.17.
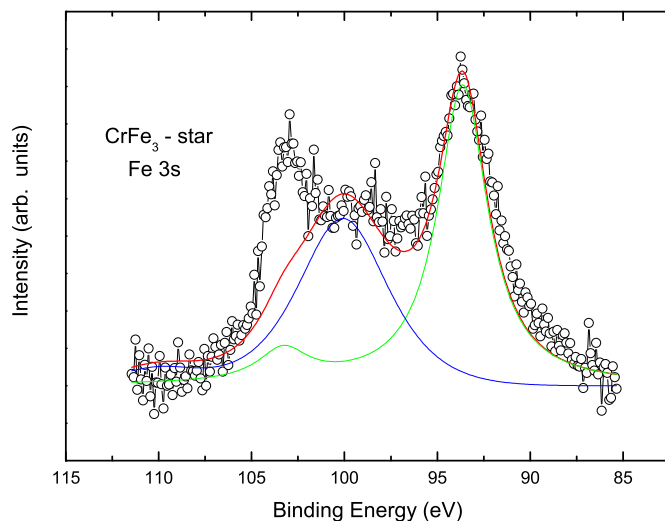
Figure 4.17: *XPS spectrum (circles) and model calculation (continuous line) of the 3s core levels (CrFe$_3$)*

For the $CrFe_3$ – star, the charge transfer is lower, allowing a higher mix with screened final states. As in the case of the $FeFe_3$ – star, where the charge–transfer energy was not low enough to generate high contributions of final state with charge transfer, the same behavior can be observed also for the $CrFe_3$ – star. As a conclusion regarding the $3s$ study on the $FeFe_3$– and $CrFe_3$ – stars, one can say that after the analysis of the screening effects, the transition–metal core–level lines (Fe), reveals for both cases a valence of M^{2+}. This conclusion is based on the value of the Δ which was obtained during the calculations, and which has a close value of those transition–metals ions which were already investigated (e.g. Fe from FeO, see [101]).

calculations for the FeFe₃ were performed from first principles within the density functional theory, using the calculation method and computer code, SIESTA [105, 106, 107].
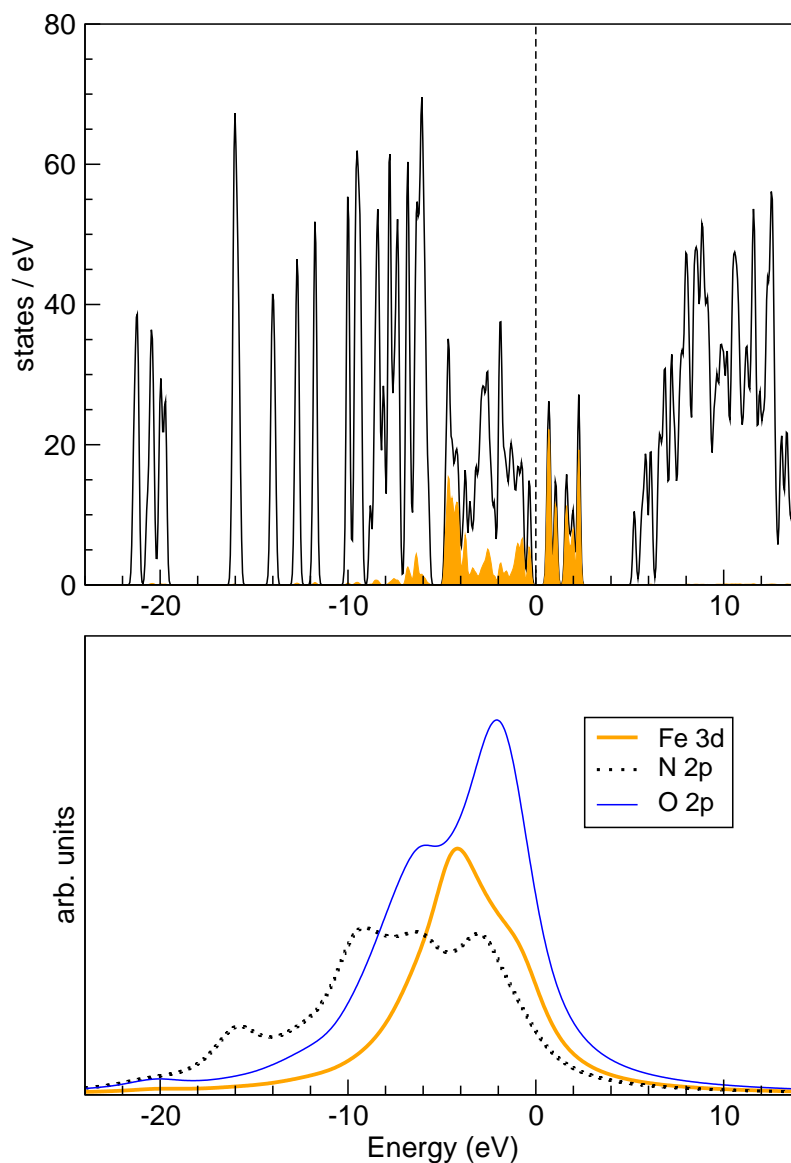
Figure 4.19: *Top panel: calculated total density of states of the FeFe₃ and local Fe 3d density of states (shaded area). Bottom panel: local densities of occupied O 2p, Fe 3d and N 2p states, additionally convoluted with a Lorentzian function of 1.6 eV halfwidth*

    The method uses norm–conserving pseudopotentials in combination with atom–centered strictly confined numerical basis functions [108, 109]. The basis set included double – ζ functions with polarization orbitals for Fe and O. The treatment of exchange–correlation was done according to the generalized gradient approximation after Perdew–Burke–Ernzerfof [110]. The single molecular unit $M[\text{Fe}(\text{L}^1)_2]_3$ was put into a simulation cell of size $22{\times}22{\times}18$

4.2.5 Valence band studies

The total and partial density of states in the valence region was investigated by means of X - ray photoelectron spectroscopy, X - ray emission spectroscopy as well as first principles calculations within the density functional theory. Fig. 4.18 presents the XPS valence band spectra of $FeFe_3$ along with the element –selective emission spectra of Fe, O and N. The emission spectra in Fig. 4.18 correspond to normal non–resonant fluorescence [104].
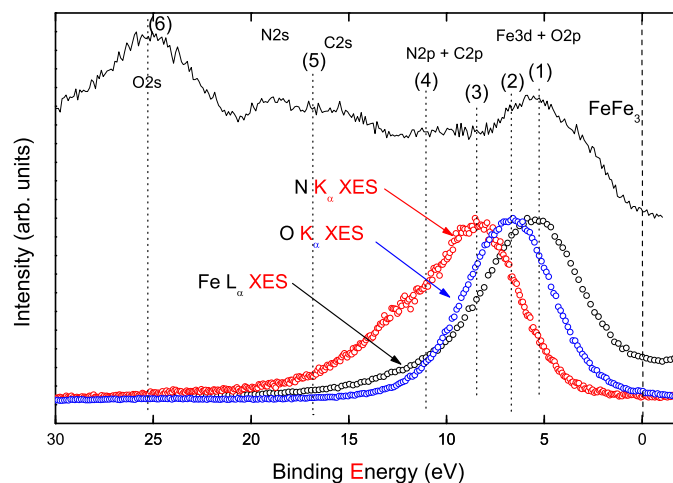
Figure 4.18: *XPS valence band of $FeFe_3$ together with the resonant XES spectra constituents*

Taking into account the binding energies of the corresponding core–levels from the XPS (710.76 eV for Fe $2p_{3/2}$, 531.96 eV for O $1s$, 400.76 eV for N $1s$), the emission spectra were brought to a common energy scale with the valence–band XPS. The excitation energies used for the XES spectra were chosen to correspond to the L_α edge for Fe and K_α threshold for C, O and N resulting from the absorption spectra, so that a close picture of the undistorted element specific density of state is achieved. The peaks visible in the XPS valence band spectrum and the corresponding emission spectra are denoted from **(1)** to **(6)**. This helps to identify the origin of pronounced features in the valence band. At the top of the valence band **(1)** and **(2)**, at about 6 eV binding energy the contribution is mostly due to Fe $3d4s$ states, but the O $2p$ states, contribute in about the same region (from ~ 7 eV to higher binding energy). The N $2p$ **(3)** states are located significantly deeper, forming a broad band centered at about 9 eV binding energy. In the middle part of the valence band **(4)** and **(5)** the N $2s$, C $2p$ and C $2s$ are strongly hybridized. Since this states are deep states, it is expected that the composition of the molecule to be independent on the nature of the transition metal ion. At the bottom of the valence band the contribution is denoted with **(6)**, which is a contribution mainly from the O $2s$ states. A deeper insight of the electronic structure of the $FeFe_3$ can be achieved by electronic structure calculations. The

Å, over which a fast Fourier transform of the charge density has been done with the cut-off 260 Ry. This corresponds to 216×216×180 divisions along the simulation cell edges, and was tested to be sufficient to obtain converged energy differences between different magnetic configurations. A discrete energy spectrum was broadened in the following figures with the halfwidth parameter of 0.1 eV in order to get a continuous density of states (DOS). The antiferromagnetic configuration (with the spin of one of the outer Fe atoms set parallel to the central one), which is 0.13 eV higher in energy. The calculations for $FeFe_3$ and $CrFe_3$ has been computed in frame of a joint co–operation by Dr. A. V. Postnikov [87].

The experimental observations are consistent with the results of first–principle calculations, which produce the DOS (summed over both spin directions) as shown in Fig. 4.19.

The top panel depicts the total DOS (summed over both spin directions) in the ground state. Zero energy separates occupied and vacant states. One finds several bands, which are derived from the C, N and O $2s$ and $2p$ levels. The lowest compact group of bands around -20 eV is almost exclusively related to the O $2s$ states. The region around the "chemical potential" (E=0) hosts Fe $3d$ states (shown shaded in the figure), which are strongly spin–split and strongly hybridize with the O $2p$ states. There is a "band gap" of about ∼0.95 eV between the highest occupied and the lowest occupied molecular orbitals, both being of mostly Fe $3d$ – O $2p$ character in the majority–spin channel. The states with the energies from -16 to -6 eV are all a mixture of different orbitals forming covalent bonds and involving C $2s$, $2p$ and N $2s$, $2p$ states.

The bottom panel of Fig 4.19 shows Fe $3d$, N $2p$ and O $2p$ contributions, summed up over atoms of the same kind in different positions in the molecule, and over both spin directions; moreover an additional broadening was introduced to yield a more straightforward comparison with the experimental XES of Fig 4.18. These three partial DOS roughly span the states probed by the emission spectra, therefore the comparison is complicated by the lack of structure in the experimental spectra. One notices however a markedly lower energy and much larger width of the N spectrum as compared to other two, in both experiment and theory. The broadness of the N spectrum indicates the participation of the N $2p$ states in a number of molecular orbitals, overlapping with C $2s$, $2p$ states through the molecule.

Spin–resolved DOS for the atoms in which the spin splitting is pronounced are shown in Fig. 4.20 A corresponding part of the molecule is shown in the inset, with the numbering of the atoms. The central atom Fe#1, which has the bridge oxygen atoms (#27) as its only neighbors, carriers a magnetic moments of 3.95 μ_B. The outer Fe atoms (#2) in the ground state are magnetized oppositely to the central one, with magnetic moments of -3.93 μ_B, and have a different environment, including two N atoms and two O #35. The latter are markedly magnetized, to -0.26 μ_B. The bridge oxygen atoms have a negligible net magnetic moment, but a marked local spin density which changes sign along the path to the nominal spin moment associated with each Fe atom. The local moment of ∼4μ_B, which is associated with Fe $3d$ states only, should be increased to ∼5μ_B if one discusses a distributed magnetic moment, which in part resides over the ligands, and follows the magnetization flips of its central Fe atom if they occur. Hence, it is a "well–behaved" rigid

of ligands, and a delocalized but rigid spin moment associated with each Fe site are quite similar to what has been reported earlier for "ferric wheels", a chemically and structurally related class of molecular magnets [111, 112].

Fig. 4.21 presents the XPS valence band of the $CrFe_3$ along with the emission spectra for Fe and O. The emission spectra for the case of $CrFe_3$ were brought as for the $FeFe_3$
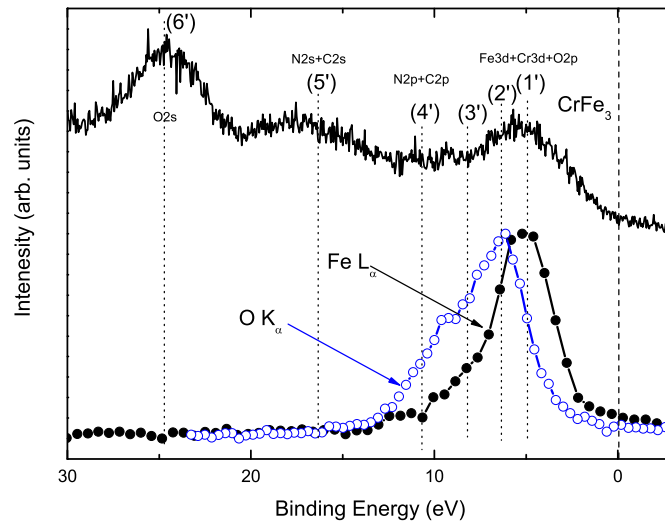
Figure 4.21: *XPS valence band of $CrFe_3$ together with the resonant XES spectra constituents*

to a common energy scale with the XPS valence–band. The excitation energies for the XES spectra correspond to the L_α edge for Fe and K_α threshold for O, resulting from the absorption spectra. In order to identify the XES contributions to the XPS valence band, these were denoted with with numbers from **(1')** to **(6')**. Before tuning to the characterization of the $CrFe_3$ valence band, an important aspect has to mentioned. The emission spectra for the corresponding Cr L_α is not presented in this study. There are two good reasons for this, the first is that the quantity of chromium in the investigated sample is considerably less that of the other elements, and the second reason is that at the Synchrotron facility were the measurements were taken (ELETTRA), the deflecting mirrors which are used, do contain chromium on their surface. For this reason I have skipped the Cr L_α emission because of the uncertainty the the given chromium line will be the one from the sample in discussion. Starting with the highest binding energy (bottom of the valence band) the features in the $CrFe_3$ valence band can be assign as it follows. Denoted with **(6')**, at about 24 eV binding energy (see Fig. 4.21) the main contribution is due to O $2s$ atomic orbitals. In the area of about 15 eV - 7 eV (**(5')**-**(3')**) on can find the a a strongly hybridized N $2p$, $2s$ and C $2p$, $2s$ states. At the top of the valence band denoted with **(2')** and **(1')** respectively, at about 6 eV binding energy the contribution is

mostly due to the Fe $3d$ states, and at about 7 eV O $2p$ states are present. As it will be seen in the computational results from this compound, the strong hybridization between Fe $3d$ states and O $2p$ states it's influenced also by the presence of the Cr $3d$ states.

As it was mentioned, spin resolved density of states of CrFe$_3$ was performed and it is presented
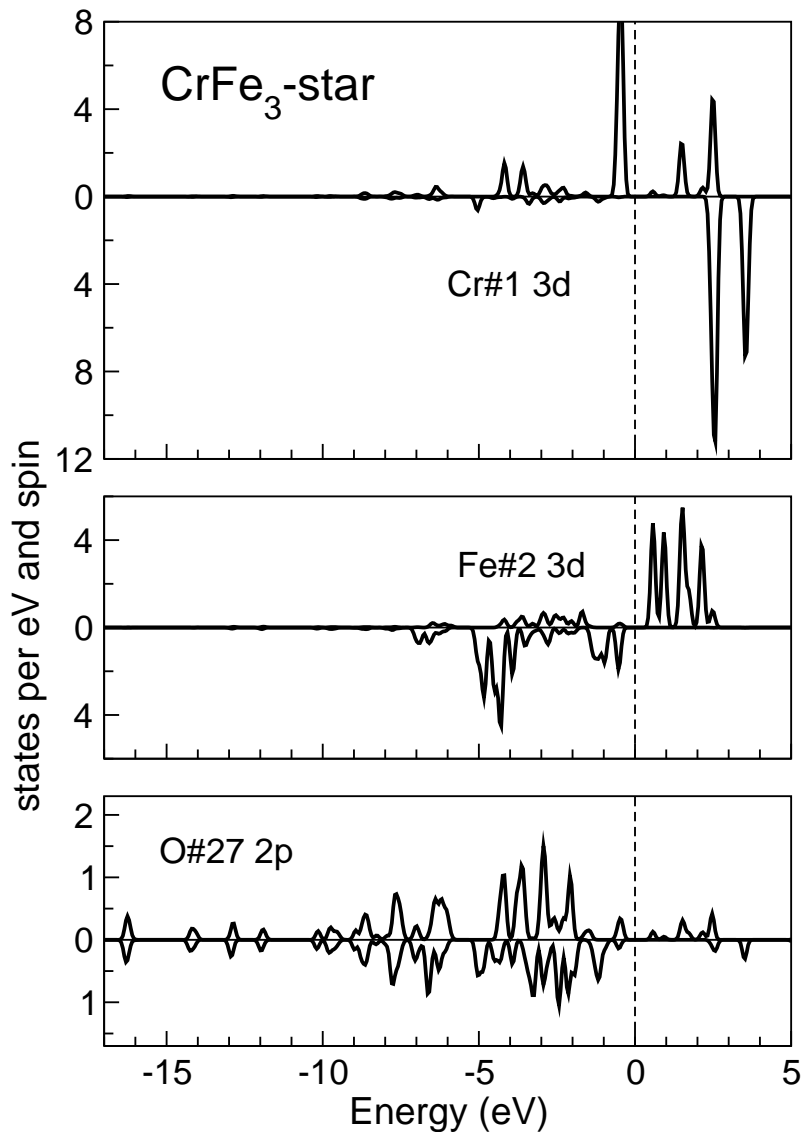
Figure 4.22: *Spin–resolved local densities of states of Cr, Fe and the bridging oxygen in the CrFe$_3$*

The situation with CrFe$_3$–star, as it seen from the calculated local density of states is different: whereas the majority spin states centered at the Cr site are not fully occupied. Moreover the lowest occupied states appear in the majority spin channel. From the above studies, and by comparing the two compounds (FeFe$_3$–star and CrFe$_3$–star), one can say
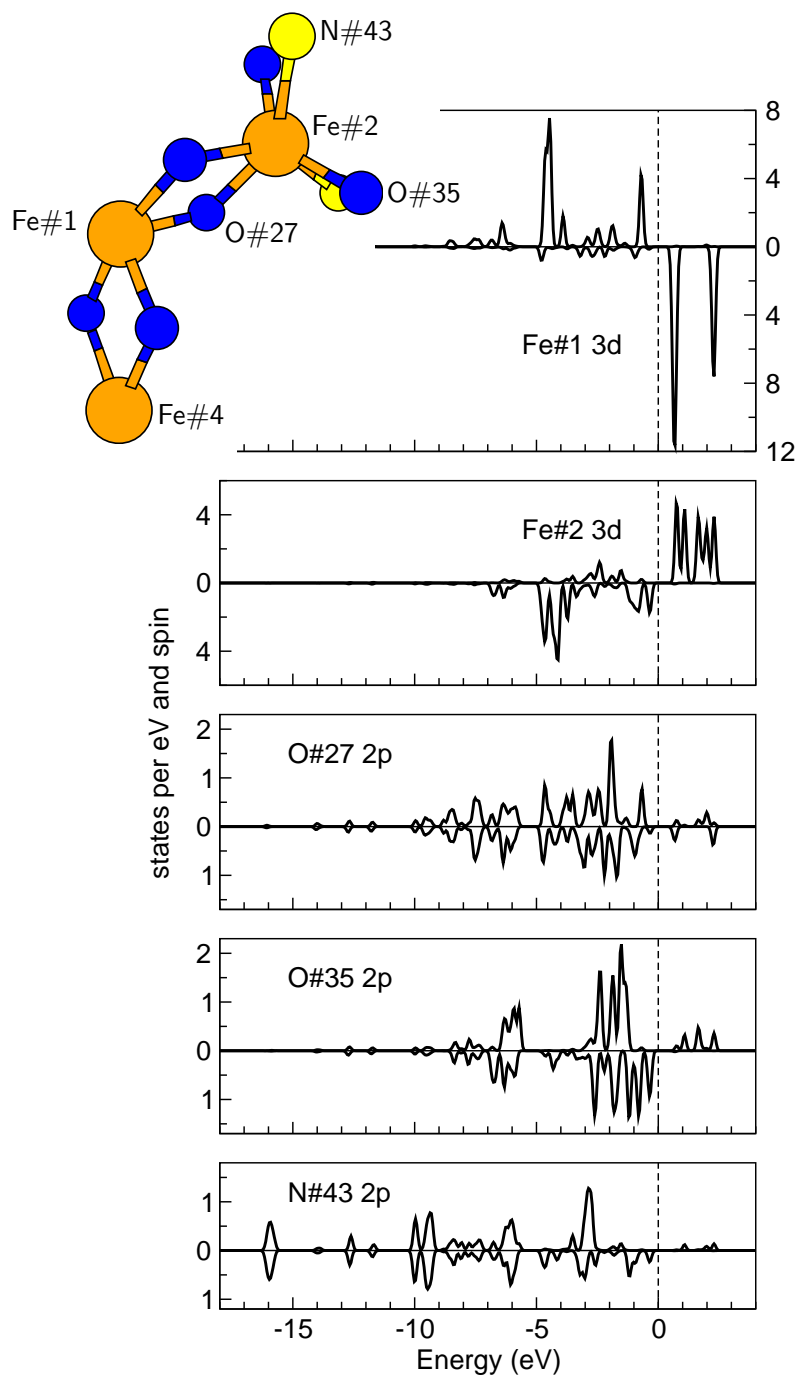
Figure 4.20: *Spin–resolved local densities of states of two inequivalent Fe sites and some their nearest neighbors. The numbering of atoms in the relevant fragment of FeFe₃ is shown in the inset*

moment in the sense that the Heisenberg model, of another model dealing with well defined spins, may be applied to it. The observations about the local DOS, induced magnetizations

that the Fe–star looks like a strong magnet, with the majority–spin band fully occupied, and only a small contribution (due to hybridization with O $2p$ states) present in the occupied part of the minority–spin channel.

Moreover, the valence band region was investigated with respect also to the unoccupied states by means of X - ray absorption spectroscopy. The most exciting one are the $3d$ metal states situated above the Fermi level. In Fig. 4.23 are presented the Fe XAS spectra for the FeFe$_3$–star and CrFe$_3$–star in comparison with the Fe L edge of the known FeO. The
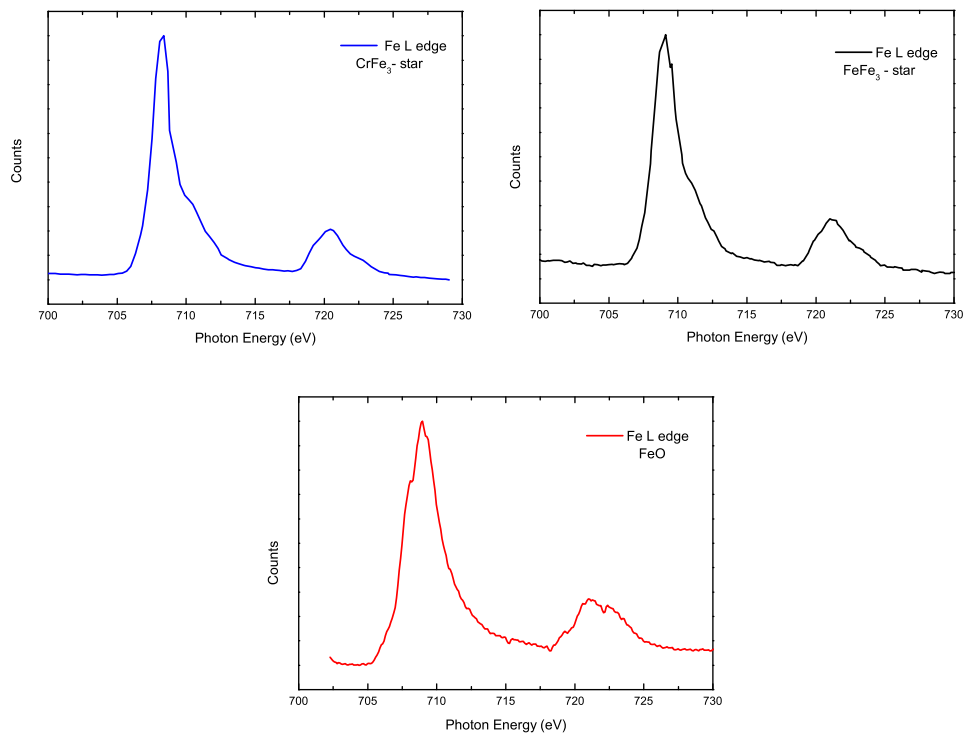
Figure 4.23: *XAS spectra of the iron 2p edges in CrFe$_3$, FeFe$_3$ and FeO*

spectra represent the excitation from the $2p$ core levels into the $3d$ unoccupied valence states. The spectrum of FeFe$_3$ consists of a main asymmetric peak at 708–709 eV and a tail at about 711 eV representing the excitations from Fe $2p_{3/2}$ core level. The second main structure starting at about 721 eV consists of excitations from the Fe $2p_{1/2}$ core–level to empty d states.

The Fe L near edge x-ray absorption spectrum of CrFe$_3$ is also presented in Fig. 4.23. The main peak as in the case of the FeFe$_3$ molecule, presents an asymmetry an it is positioned at about 708–709 eV and it is arising from the excitations of the Fe $2p_{3/2}$ core–level. The second peak which is situated at about 720-721 eV represents the excitations from the Fe $2p_{1/2}$ core–level. Since the $2p$ core hole wave function has a large overlap

with the $3d$ wave function in the $2p$ absorption is determined by the transition probability $3d^n \longrightarrow 2p^5 3d^{n+1}$. The strong overlap of the wave function is also responsible for the multiplet effect that makes the $2p$ x–ray absorption line shapes to be given, in the first approximation, by the $2p^5 3d^7$ final state in case of a Fe^{2+} ion [113]. A certain similarity does exists between the Fe L edge of FeO and corresponding edge from $FeFe_3$ and $CrFe_3$, regarding the spin orbit splitting. As in the case of the XPS data, we can associate the valency of the Fe from FeO to the one belonging to the "ferric star"–molecule.

4.2.6 Resonant X–ray emission in pure and Cr–doped ferric star

In the present section of the thesis, the comparative analysis of pure and Cr–doped systems will be presented. The Cr substitution site is not unambiguously determined by experiment, whereas recent firs–principle calculations presume that if must be the central one [114]. The valence–band XPS and Fe L–emission spectra are very similar in both systems, and Cr-related features cannot be resolved. However, certain differences were found when analyzing resonant X–ray emission, see Figs. 4.24

Panel (a) of Fig- 4.24 depicts the NEXAFS spectrum of the "ferric star" with M=Fe, converging the Fe $L_{2,3}$ edges. The peak about 709 eV corresponds to the (L_3) excitations from Fe $2p_{3/2}$ core state into the unoccupied $3d$ band, and the second one at about 721 eV corresponds to those (L_2) from the Fe $2p_{1/2}$ state. The asymmetry seen int the first structure was explained in the terms of many overlapping multiples [115]. When comparing this two–peaked structure with the XPS, we note that here the L_2–L_3 splitting is 12.73 eV, i.e. less than the spin–orbit splitting of the Fe $2p$ states determined by XPS (14 eV). The reason for the discrepancy is that the both the XPS and absorption spectra consists of many multiples, but these multiplets are different for the ionic (XPS) and neutral (absorption) final states, and therefore have different splittings. Panel (b) of Fig 4.24 shows the emission spectra at the L_3 edge, obtained for four different incident photon energies: 719.02, 719.25, 720 and 720.9 eV. Their position at the threshold and on the top of the L_2 edge are indicated in the panel with the absorption spectrum.

In RIXS, a $2p \to CB$ (CB: conduction band) excitation is followed by a $VB \to 2p$ (VB: valence band) X–ray emission; both events are normally treated as a single joint process. As the excitation energy is gradually increased, on reaching the L_3 absorption threshold the L_α emission ($3d \to 2p_{3/2}$) becomes possible. As the incident photon energy approaches the L_2 threshold, the L_β emission ($3d \to 2p_{1/2}$) appears as well. The L_α emission persists, as an off–resonance scattering process (creation and annihilation of a $2p_{3/2}$ hole), but also possible by Coster–Kronig process. In the latter, an initial $2p_{1/2}$ hole is filled due to a radiationless $2p_{3/2} \to 2p_{1/2}$ transition, and the resulting $2p_{3/2}$ hole is filled by the L_α emission. These different mechanisms affect the L_α/L_β intensity ratio as a function of the excitation energy, and its possible deviation from the statistical 2:1 relation. We observe that the $FeFe_3$ and $CrFe_3$ stars, in spite of many similarities in their Fe L spectra, behave markedly different in what regards the L_α/L_β intensity ratio on passing through the L_2 resonance excitation. In Fig. 4.24 (b) one can observe that at the maximum of the absorption resonance, the L_β intensity is higher than that of L_α, oppositely to what would
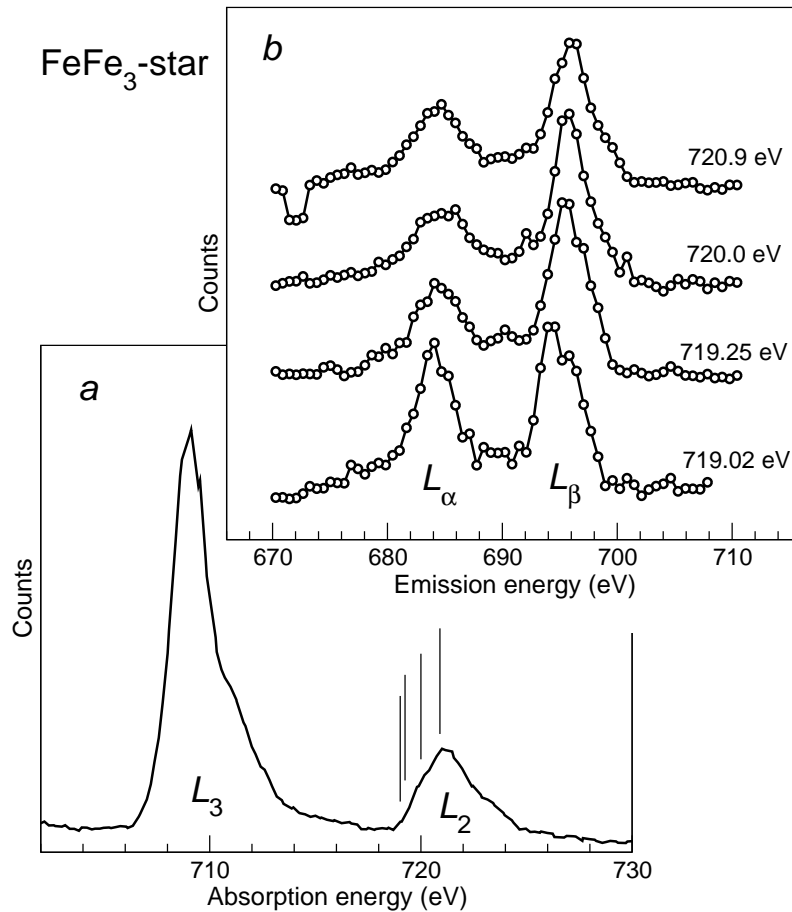
Figure 4.24: *Near–edge X–ray absorption Fe $L_{2,3}$ spectrum (a) and resonant inelastic X–ray Fe L_3 emission spectra (b) of the Fe–"ferric star" for four selected excitation energies, which are also shown in the bottom panel as vertical bars*

be a statistical distribution. We will see that this seems to be an anomaly, which does not happen in the case of Cr substitution in the "ferric star".

Fig. 4.25 (a) depicts the NEXAFS at the Fe $L_{2,3}$ edge for the Cr–doped sample, and Fig. 4.25 (b)–the X–ray emission spectra, now taken at the resonance 718.3, 719, 719.6 and 720.4 eV, from the onset to the maximum of the L_2 absorption. The intensity of the L_β emission first grows and than remains constat, relative to that of L_α, in a roughly 1:2 relation. This is the situation which occurs in most materials. The fact that in the RIXS spectra of the $FeFe_3$–star the L_α/L_β the intensity ratio is inverted to become <1 reveals the fact that usual mechanics which channel the L_2 excitation into the L_α emission, e. g. Coster–Kroning transitions, are largely suppressed.

The same (anomalous) behavior has been observed and discussed for the case of FeO, in contrast to (conventionally behaving) FeS_2, by Prince *et. al* [99]. Another example of such an anomaly was reported for Mn L RIXS spectra in Heusler alloys [116]. The interpretation of results in these papers related the L_α/L_β intensity anomaly to the high–
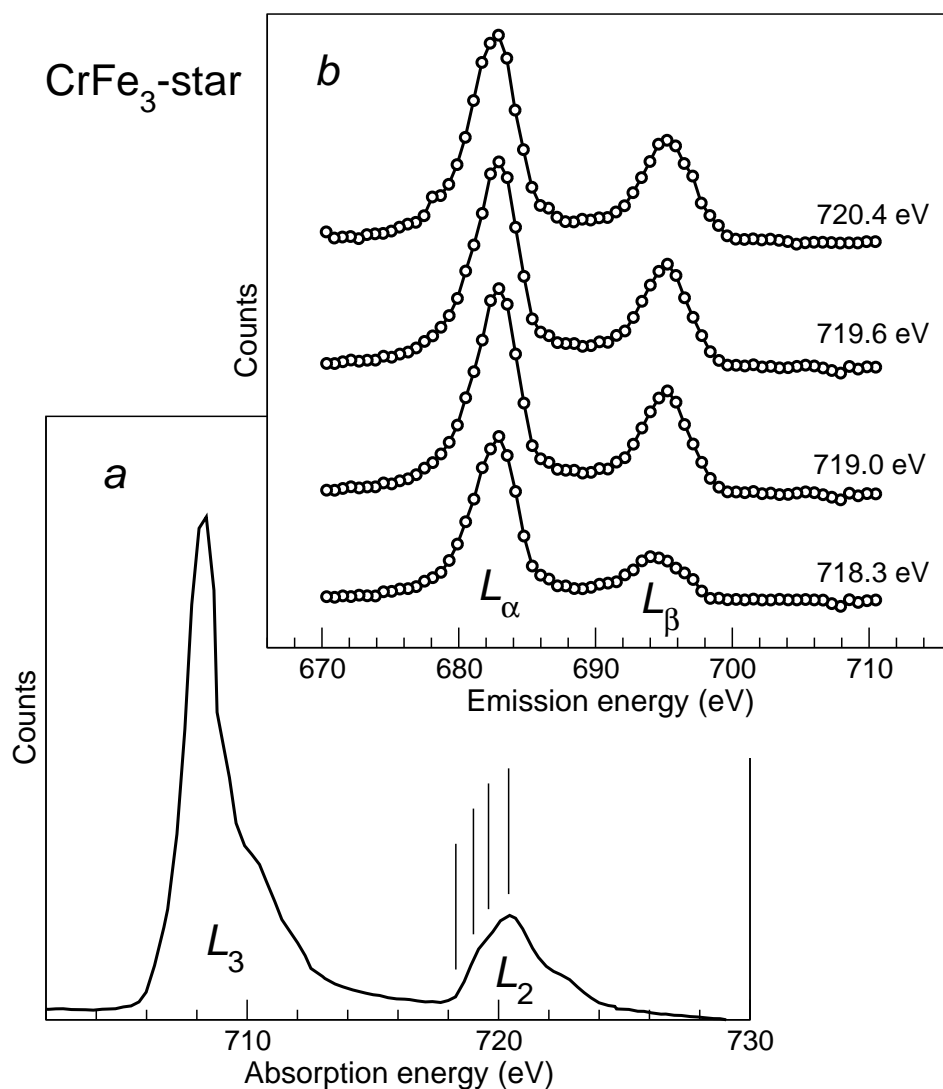
Figure 4.25: *Near–edge X–ray absorption Fe $L_{2,3}$ spectrum (a) and resonant inelastic X–ray Fe L_3 emission spectra (b) of the Cr–"ferric star" for four selected excitation energies, which are also shown in the bottom panel as vertical bars*

spin state of Fe or Mn. More specifically, the importance of having an electronic structure with the majority–spin band fully occupied and the minority–spin band completely empty was emphasized. In this case a sequence of two process, which may involve a Coster–Kroning transition as an intermediate step–an electron excitation into the conduction band and filling the $2p_{1/2}$ core hole by a $2p_{3/2}$ electron–cannot occur except with the inversion of spin, which is a low–probability event. On the contrary, the electron excitation into the conduction band and an immediate fluorescence transition, which is a resonance process, remains allowed and explains the dominance of the L_β emission on L_2 excitation. As it was mentioned in the previous chapter, the local Fe density of states, in the FeFe$_3$–star

presents the conditions of a strong magnet, with the majority–spin band fully occupied, and only a small contribution (O $2p$ states hybridization) present in the occupied part of the minority–spin channel. Therefore the anomalous RIXS in the FeFe$_3$–star can be explained consistently with that in FeO or in the Heusler alloys. The situation with the CrFe$_3$–star, as is seen from the calculated local density of states, shown in Fig. 4.22, is different: whereas the Fe local density of states (of the peripheral atoms) is identical to that in the FeFe$_3$, the majority–spin states centered at the Cr site are not fully occupied. Moreover the lowest unoccupied states appear in the majority–spin channel. Therefore the absorption–emission process involving the Cr $3d$ states may happen without the inversion of spin [117]. However it has to be admitted that it is difficult to understand how this fact helps to reduce an apparant blocking of the Coster–Kroning transitions *at the Fe site*. Some clue may be provided by considering the bridging oxygen atoms (# 27 of Fig. 4.22): whereas in the FeFe$_3$–star the magnetization density changes its sign exactly at the bridging oxygen, in the CrFe$_3$–star this oxygen atom is fully magnetizes along with its Fe neighbor, and oppositely to Cr. One can speculate that the matrix elements of the core-valence transitions, which include differently composed molecular orbitals in the valence band of FeFe$_3$– and CrFe$_3$–stars, may affect relative weights of L_α and L_β emission. This is however difficult to estimate without an explicit calculation of the RIXS process.

With relative certainty, one can eliminate the following other hypothetical explanations of a missing anomaly in the L_α/L_β intensity ratio of the CrFe$_3$ star. A possibility of a low–spin state is ruled out by the calculation result that in all trial spin–polarized calculations, the local magnetic moments remained essentially fixed to $\simeq 3$ μ_B at the Cr site and $\simeq 4$ μ_B at Fe sites. There is no way to "prepare" the system with a low–spin state of either Cr, or Fe [91]. All inversions of individual local moments from the ground state, including the situation with the lowest total magnetic moment of 2 μ_B in the Cr$_\uparrow$Fe$_\downarrow$Fe$_\downarrow$Fe$_\uparrow$ star, preserve the "strong magnetism" at the Fe site and the partial emptiness of the majority–spin states at the Cr site, with strong similarities of their corresponding density of states to those shown in Figs. 4.20 and 4.22.

Also the assumed Cr substitution in the peripheral position (highly energetically un-favorable, as was mentioned above) affected the magnetic moments and local density of states only slightly. An additional inclusion of on–site intraatomic Coulomb correlation beyond the conventional DFT treatment may affect the energy placements of $3d$ levels in the Cr and Fe density of states, but it can only enhance the "strong magnetism" at the Fe stie rather than ease it, in the presence of Cr dopant.

Therefore the understanding of "normal" L_α/L_β behavior in the CrFe$_3$–star is incom-plete on the basis of DFT calculations, whereas an explanation of "anomalous" behavior in the FeFe$_3$–star seems rather obvious, and consistent with the observed trend [99] for FeO, as compared to FeS$_2$. We can only emphasize the observed difference in RIXS spectra of FeFe$_3$– and CrFe$_3$–stars an experimental finding, which might stimulate additional research on these systems.

4.2.7   Angular and distance dependence of the magnetic properties

The aim of this section is to study in more detailed and to explain by employing a theoretical model, the magnetic interactions which occur in the investigated compounds. In order to find out the magnetic behavior (magnetic interactions), in a given compound, one has to calculate the total energy of the system in the ferromagnetic (FM) and antiferromagnetic (AFM) configurations of the magnetic moments and decide which one is energetically more convenient. Because of the close competition between the ferromagnetic and antiferromagnetic interactions which occur in the $FeFe_3$– and $CrFe_3$–star molecules, a more "inside" study is necessary in order to understand this "competition". Since the ferromagnetic coupling is still an exceptional case in these materials, the patterns which favor the ferromagnetic alignment are of highly interest. One of the main concerns regarding the magnetic interactions, is to discern the factors responsible for the obtained configurations.

Two main factors can be accounted for the sign of the exchange coupling:

- the nature of the magnetic ions

- the molecular structure
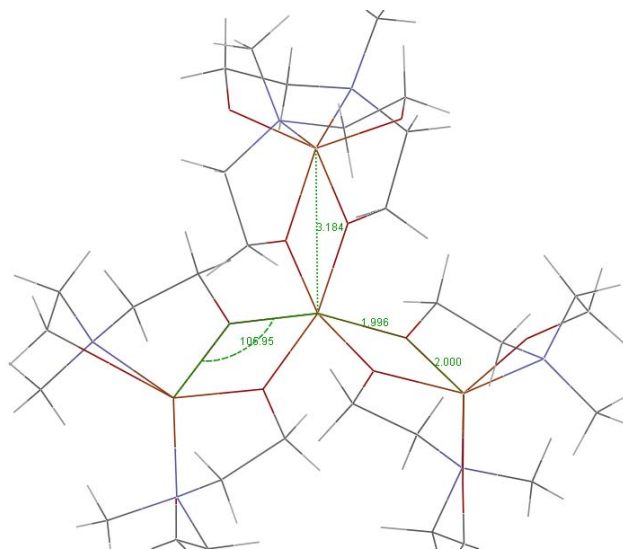
Figure 4.26: *Crystallographic structure of the "Star Molecule" including distances and angles*

The nature of the magnetic ions it is important with respect to the occupancy of the magnetic orbitals, while the crystal structure gives a magnetic interaction "view" with regard to the intra–atomic distances and bounding angles. Before going into more detailed description regarding the magnetic interactions, a description of the crystal structure will be given, in order to have a close picture of the molecules. The central transition metal

ion is linked via two μ_2–alkoxo bridges from each of the terminal blocks $[\mathrm{Fe(L^1)_2}]^-$. The formation of the based molecule by the linking of the central transition metal (Fe, Cr) with the terminal blocks, it is made in a symmetrical way, so that the distances between the central atom and the peripheral Fe atoms are the same. Moreover, the angles which are formed by the bridging via the oxygen atoms ($\widehat{MOFe}$) (M=Fe,Cr) are also approximately the same in all three directions. In this case, the distance between the central transition metal ion and the peripheral ones was found to be 3.8 $\mathring{A}$, the distance between the central transition metal atom and the bridging oxygen atom was found to be 1.96 $\mathring{A}$, meanwhile the angle which is formed by the transition metal (the central one and the peripheral one) via the oxygen atoms is $\simeq 105^0$ (see Fig. 4.26).

The starting point in the analysis of the magnetic interactions of both systems, is to discern for eligible magnetic interactions. Regarding the symmetric "construction" of the "ferric star"–molecules, one can take into consideration the interactions which may occur between the central TM–ion and the peripheral ones via– the bridging oxygens. For this reason, a schematic drawing of the possible magnetic interactions which can occur, is presented in Fig. 4.27, where the left **M** denotes the central TM–ion, which can be Fe or Cr while the right **M** denotes the peripheral Fe atom. The interactions which can
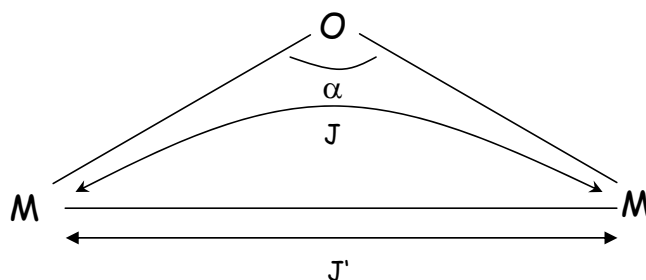
Figure 4.27: *Possible magnetic interactions in the "Star Molecule" single molecule magnet*

be taken into account are the direct metal–to–metal exchange interaction (J') and the superexchange interaction, given by the bridging oxygen atoms (J). The intensity of the J' interaction depends on the overlap of the magnetic d orbitals of the transition metal ions. Regarding the distance between the two transition metal atoms ($3.19\mathring{A}$), one can say that the probability of the overlapping of the $3d$ orbitals is practically minimized by this distance. Because of the smallest distance and the "more favorable" angles which occur between the transition metal ions and the bridging ligands, the superexchage (J) interaction will predominate in this molecule. Concluding, the J' contribution will be neglected, and we will take into consideration just the J interaction which is giving the so called superexchange interaction. In the case of the superexchange interaction, the transition metal cations are to be regarded as "source" of magnetic moments while the organic species owing filled orbitals provide the exchange paths. For the case of the J interaction, the superexchange pathway corresponds to M–O–Fe (M=Fe,Cr). As originally proposed by Anderson in its kinetic form the superexchange interaction occurs with the

excitation of an electron from a bridge–anion orbital into the partially filled d orbital of the transition metal cation [118, 119, 120]. Taking into account the well known Goodenough–Kanamori–Anderson (GKA) rules, for the case of the superexchange interaction, depending on the angle which forms the bridging, there are two possibilities. The first case is the so called "180 degrees interaction", where the transition metal ions are interacting via a ligand and forming an angle of 180^0. In this case, the exchange interaction will be a strong one and always antiferromagnetic(AFM– ↑↓). The second case is the "90 degrees interaction", were the transition metal ions are interacting via a ligand and forming an angle of 90^0. In this case like for the case of 180^0, the actual electron transfer occurs between the d–orbitals of the transition metal and the p–orbitals of the oxygen. As a result, the virtual electron hops and one electron is transferred from one of the p orbitals of the oxygen to the transition metal ion. The second GKA rule, 90^0, is ferromagnetic (FM– ↑↑)and relatively weak. For the case of the "ferric star"–molecule, regarding the fact that the angle which bridges the superexchange interaction is closer to 90^0, we will apply the second rule of the GKA-rule to the "ferric star molecule" in order to identify the interactions which occur in the molecule. Taking into account the 90^0 interaction a schematic representation of the
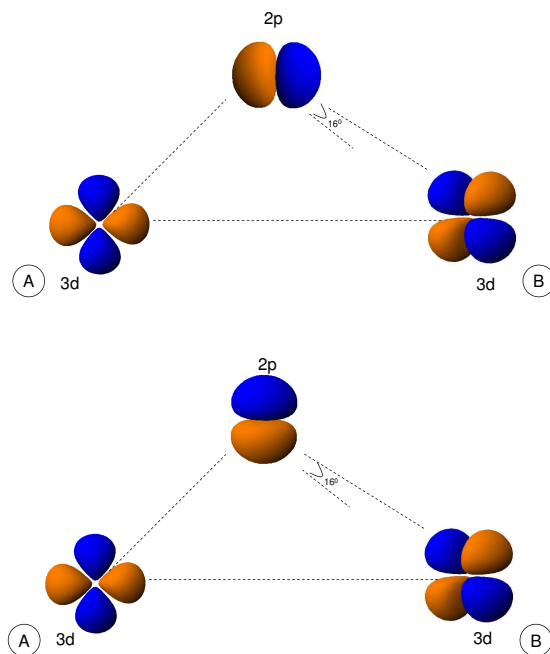
Figure 4.28: *Schematic representation of the possible interactions of the orbitals in the "ferric star" molecule*

orbitals which are interacting is given in Fig. 4.28.

In order to explain the magnetic interactions between the two transition metal sites via the oxygen atoms, the following parameters have to be taken into account: α (the angle which forms the superexchange path) and r_1 and r_2 the distances from the TM–ions

to the oxygen atom. The magnetic properties are given in terms of J, as a parameter of the effective Hamiltonian. The magnetic interaction between two coupled spins $\vec{S}_A$ and $\vec{S}_B$ localized on the molecular units A and B can be described in terms of spin–only Heisenberg–Dirac–Van–Vleck Hamiltonian:

$$H = J\vec{S}_A \cdot \vec{S}_B \tag{4.14}$$

which often appears in the form $-2J\vec{S}_A\vec{S}_B$, with $\vec{S}_A=5/2=\vec{S}_B$. In equation 4.14, the ferromagnetic and antiferromagnetic situations are represented by negative and positive J values, respectively. Two distinct contributions to J are recognized :*a)* kinetic exchange, originating in one–electron transfer process, and *b)* potential exchange due to true two–center two–electron exchange interactions. The second contribution is always ferromagnetic. It was recognize that in insulating transition metal ion systems kinetic exchange usually dominates [121]. In the sense of the interactions which can occur in the superexchange interaction, there is a schematic drawing presented in Fig, 4.29 with terms of the superexchange interaction.
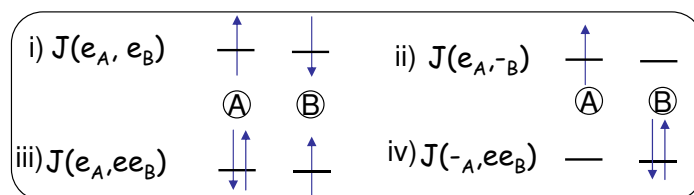
Figure 4.29: *Terms of the superexchange interaction*

i) The most important contribution originates when an electron in a half–filled orbital on center **A** interacts with an electron in a half–filled orbital on center **B**(i)). This contribution is given by :

$$J(e_A, e_B) = \frac{2}{n_A n_B} \cdot \frac{h_{ij}^2}{U} \tag{4.15}$$

where n_A and n_B are the numbers of unpaired electrons on centers **A** and **B**, respectively. The transfer integral is defined by:

$$h_{ij} = \langle a_i | \hat{h} | b_j \rangle \tag{4.16}$$

where $\hat{h}$ is the appropriate one–electron interaction Hamiltonian. U corresponds to the energy difference between the ground electron configuration and the electron–transfer configuration where one electron has been removed from the one center and restored on the other. J(e_A,e_B) is always **antiferromagnetic**.

ii) For the case of the interaction between half–filled orbital on **A** site and empty orbital on **B** site, the contribution to J is given by:

$$J(e_A, -_B) = -\frac{2}{n_A n_B} \cdot \frac{h_{ij}^2}{U} \frac{/}{U} \tag{4.17}$$

The quantity $/$ takes account of the intraatomic exchange interactions with the charge–transfer electron configuration. The $J(e_A,\text{-}B)$ contribution will give a **ferromagnetic** interaction.

   iii) For the interaction of a half–filed orbital on **A** with a full orbital on **B** the contribution is also given by.

$$J(e_A, -_B) = -\frac{2}{n_A n_B} \cdot \frac{h_{ij}^2}{U} \frac{/}{U} \qquad (4.18)$$

This contribution will also give a **ferromagnetic** interaction. Both of the ferromagnetic interactions are smaller than the antiferromagnetic one, by the $/$ $/U$ factor.

   iv) The last possible type of interaction is that between an empty orbital on **A** site and a full orbital on the **B** site. The contribution of the $J(-_A, ee_B)$ to J has been reported to be **ferromagnetic** or **antiferromagnetic**, depending on the number of the unpaired electrons from the d states of the interacting transition metal ions [3]. Taking into consideration the above mentioned interactions which can occur during the superexchange interaction, one can present the magnitude of the interactions as it follows:

$$|J(e_A, e_B)| > J(e_A, -_B) > J(e_A, ee_B) > |J(-_A, ee_B)| \qquad (4.19)$$

   Applying the above mentioned interactions to the $FeFe_3-$ and $CrFe_3$–stars, one can obtain the result of the superexchange interaction in the studied compounds. Moreover, by introducing this model in the study of the $FeFe_3-$ and $CrFe_3$–stars, we can talk about a contradiction to the GKA–rules with regard to the superexchange interaction. In Fig. 4.30 are presented the possible interactions which can occur in the $FeFe_3$ star. The model for the
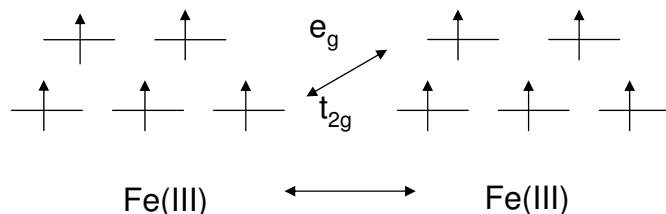
Figure 4.30: *Schematic representation of the d levels in the interacting transition metals (Fe–Fe)*

superexchange interaction, takes into account a valency of 3+ for the Fe ions, giving in this case a configuration of $3d^5$. Considering that the Fe is in a high–spin state, the occupancy of the electrons in the d shell, will be given by $t_{2g\uparrow\uparrow\uparrow}e_{g\uparrow\uparrow}$. Starting from this point, in the case of the $FeFe_3$–star, the possible interactions are governed by $J(e_A,e_B)$. This is a result of the interactions between the $t_{2g}\rightarrow t_{2g}$ or the $t_{2g}\rightarrow e_g$ orbitals, the only possible interactions which may occur in this case, giving a strong antiferromagnetic interaction for the $FeFe_3-$ star. This conclusion is in "contradiction" with the GKA–rules, which states that in

---

[3]A more detailed description can be found in [122]

the case of a superexchange interaction, having a 90^0 angle between the two interacting transition metal ions, will give a weak ferromagnetic interaction. We can call this as a modification from the GKA–rules. The same behavior was observed for the case of $CuGeO_3$, where the angle which gives the superexchange interaction is more closer to that of 90^0 ($\simeq 98^0$) [123].

In Fig. 4.31 are presented the possible interactions which may occur in the CrFe$_3$–star molecule.
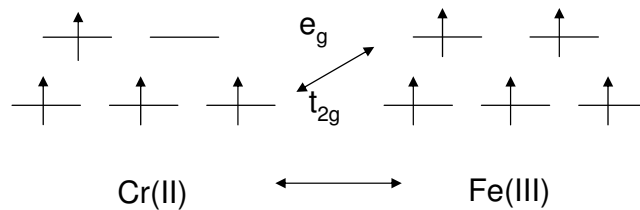
Figure 4.31: *Schematic representation of the d levels in the interacting transition metals (Cr–Fe)*

In the case of CrFe$_3$–star, because of the chromium valency (Cr^{2+}), the contribution to J is different than that of the FeFe$_3$. As one can see, in the above figure, the configuration of the $3d$ states for chromium is $3d^4$, meaning that an e_g orbital from the Cr site is empty, giving the "opportunity" that an half–filled orbital from the Fe site to interact with it. The interactions between the orbitals will be the same like in the case of FeFe$_3$, meaning that we will have either t$_{2g}$→t$_{2g}$, or a t$_{2g}$→e$_g$ interaction. The t$_{2g}$→t$_{2g}$ interaction will lead to a interaction between two half–filled orbitals, giving as a result the $J(e_A, e_B)$, a strong antiferromagnetic interaction. The other possibility is to have a e$_g$→t$_{2g}$ (t$_{2g}$→e$_g$) interaction which can be accounted for the two different interactions: the first, an interaction between two half–filled orbitals, giving the same strong antiferromagnetic interaction, characterized by $J(e_A, e_B)$; and the second one, the interaction between an empty orbital and a half–filled orbital, leading to a $J(-_A, e_B)$–giving a ferromagnetic interaction. The competition between this two interactions (antiferromagnetic and ferromagnetic), can be easily estimated in the sense of the magnitude of the interactions. Following the magnitudes given by Güdel, regarding the superexchange interactions, we can conclude that for the case of the CrFe$_3$–star, the antiferromagnetic interaction will be predominant in the favor of the ferromagnetic one (see. 4.19).

4.3   Magnetic measurements

The magnetization and susceptibility measurements were provided by Prof. Dr. Emil Burzo from Babes–Bolyai University, Cluj–Napoca, Romania. The measurements were performed with the Mag Lab System^{2000} produced by Oxford Instruments, which is a multi–measurement platform that allows different measurements. The temperature dependence of magnetic susceptibility χ, taken in a magnetic field of B=1 T for FeFe$_3$– star is plotted in Fig. 4.32
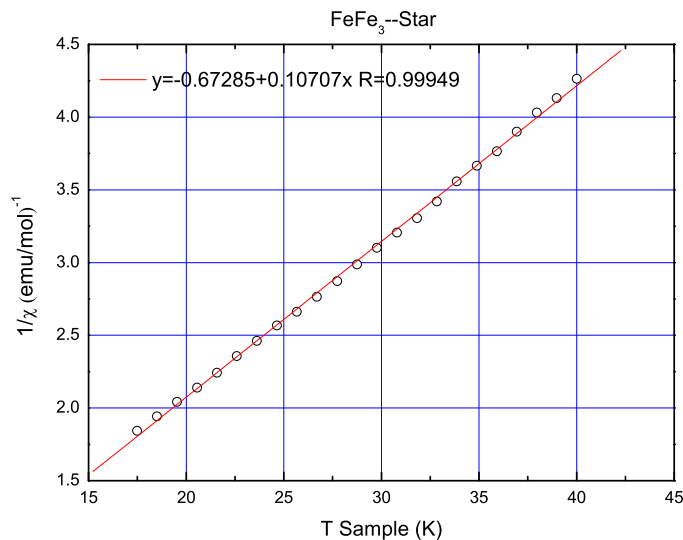
Figure 4.32: *Temperature dependence of magnetic susceptibilities for FeFe$_3$*

A Curie–Weiss behavior is observed above the characteristic temperature (T>10 K). A linear fit was performed for the Curie–Weis equation:

$$\chi = \frac{C}{T - \theta} \tag{4.20}$$

giving the equation for the fitted line as:

$$y = -0.67285 + 0.10707 \cdot x \tag{4.21}$$

In equation 4.20, C denotes the Curie constant, while θ represents the paramagnetic Curie temperature. For the linear region of χ^{-1} versus T, the effective iron moment was determined and found to be 4.32 μ_B/Fe atom. The effective moment of the Fe was obtained directly from experimental data .

The same measurement was performed on the CrFe$_3$– star, and the temperature dependence of the magnetic susceptibility is presented in Fig 4.33.
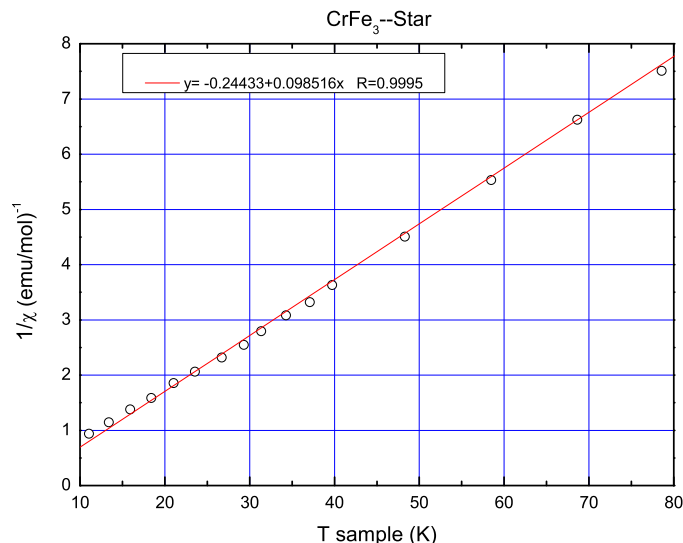
Figure 4.33: *Temperature dependence of magnetic susceptibilities for CrFe$_3$*

The same behavior as in the case of FeFe$_3$– star can be seen above the critical temperature (T>10 K), namely the Curie – Weiss type of behavior, giving the fitting equation of:

$$y = -0.24433 + 0.098516 \cdot x \tag{4.22}$$

In the case of CrFe$_3$ – star, the effective magnetic moment was found to be 4.36 μ_B/Fe atom, which is close to the value obtained for the FeFe$_3$, indicating in both cases a valency of Fe^{2+}, confirming the XPS results.

For both cases, the paramagnetic Curie temperatures are negative and found to be $\theta_{FeFe_3}= -0.62$ K and $\theta_{CrFe_3}= -0.24$ K. In Fig. 4.34 , the determination of the saturation of the magnetization for FeFe$_3$– star is presented. In order to obtain the saturation of the magnetization, the measurements were recorded by applying different magnetic fields, from 9 to 7 Tesla and different temperatures, from room temperature (300 K) to 5.5 K.

The maximum in the saturation of the magnetization was found to be $\simeq 6.5$ μ_B/f.u. at a temperature of 5.5K while the minimum was found to be at the room temperature at the value of 0.5 μ_B f.u.

The same study was performed also on the CrFe$_3$ – star, and the determination of the M$_s$ value is represented in Fig. 4.35.

In this case the saturation of the magnetization was found to be $\simeq 9$ μ_B f.u. at the temperature of 5 K.

In Fig. 4.36 and 4.37 the temperature dependence of the magnetization for FeFe$_3$ and CrFe$_3$ is represented. For the case of M = Fe, the magnetization shows a maximum at $\simeq 10$ K, while for the case of M = Cr, the maxima was found to be at $\simeq 15$ K. These maxima are
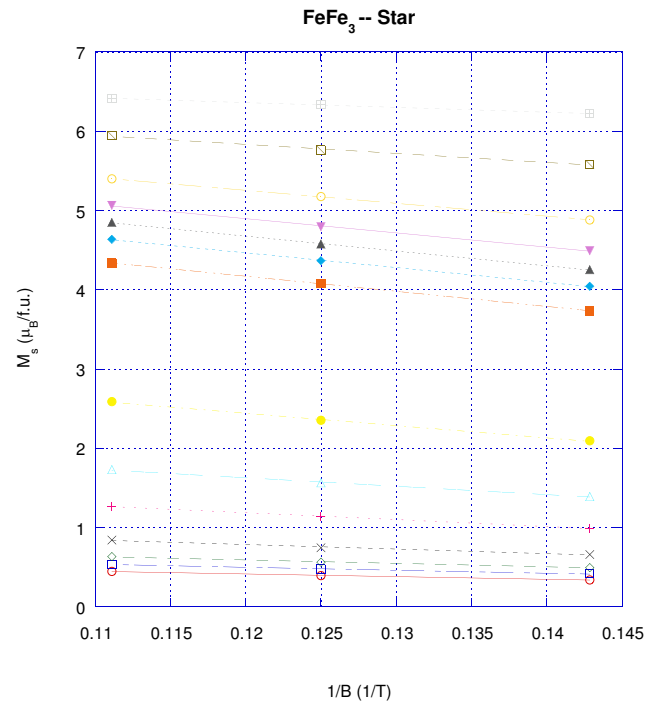
Figure 4.34: *Determination of the magnetization at saturation in FeFe$_3$–star*
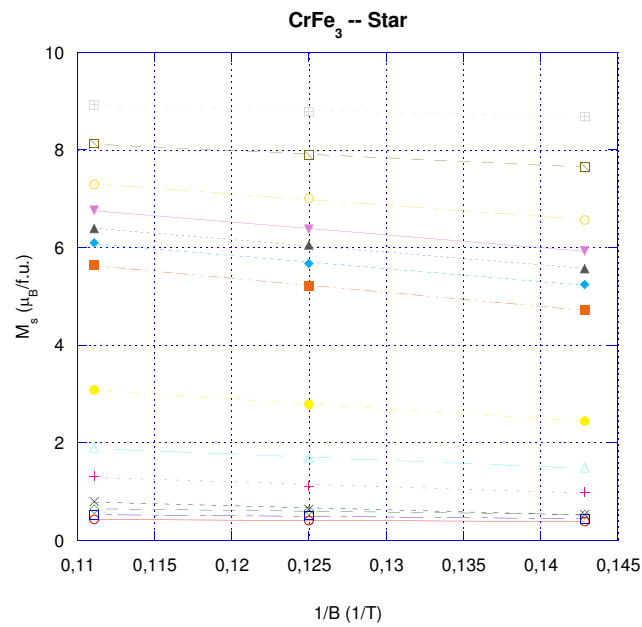
Figure 4.35: *Determination of the magnetization at saturation in CrFe$_3$–star*
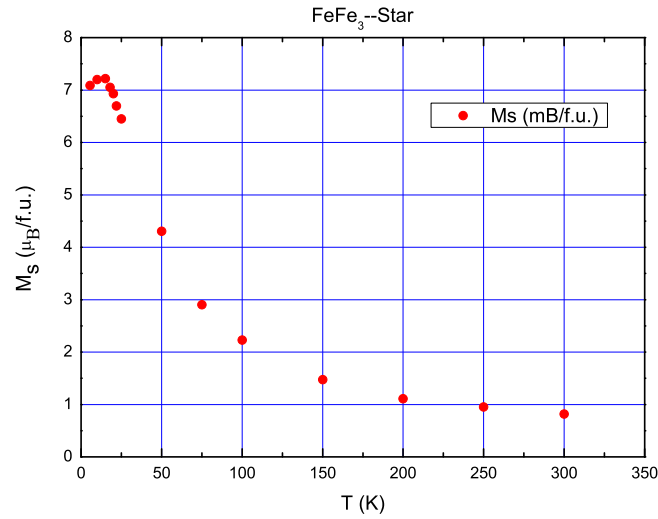
Figure 4.36: *Magnetization in function of temperature in FeFe₃–star*
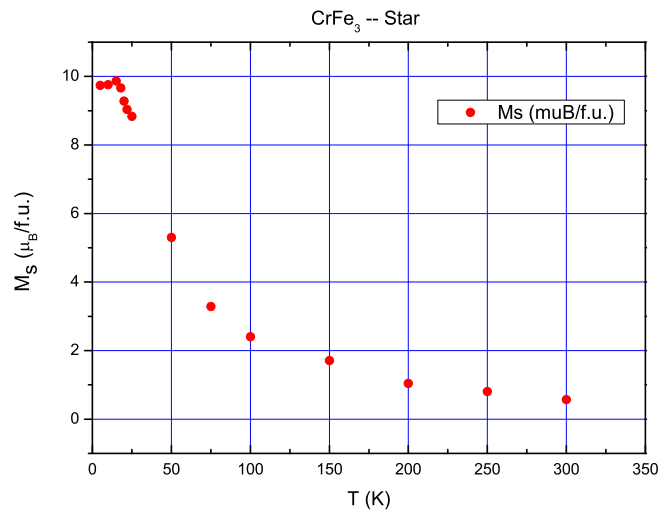
Figure 4.37: *Magnetization in function of temperature in CrFe₃–star*

characteristic for ferromagnetic exchange interactions between the M ions in the cluster fragment [124] [125]. At higher temperatures (approaching the room temperature), the magnetization values are decreasing with the increasing of the temperature, which suggests antiferromagnetic interactions between neighboring transition metals.

Analyzing the magnetization isotherms, presented in Figs. 4.34 and 4.35, one can see that the determined magnetizations are lower as compared to the expected values taking

into account the number of transition metal ions present in the system as given by the ideal formula. This can be explained when we assume that the transition metal ion in the case of $FeFe_3$ – star is in a bivalent state and the Curie constant is given by the free ion value and the molar mass is that given by nominal compositions. The Curie constant for the case of $FeFe_3$ –star can be obtained from the χ^{-1} vs. T, while the effective Fe^{2+} moment is $\simeq 4.38\ \mu_B$/ion and from this one can find the number of Fe^{2+} ions in the lattice which was found to be subunitary, instead of 4. Assuming that the saturation moment at T = 10 K of Fe^{2+} ion is $4\mu_B$ in the ferromagnetic coupling it results a saturation of $\simeq 5.5$ μ_B, the value obtained from the magnetization isotherm (see fig. 4.34). The Cr ions for the $CrFe_3$ – star was determined. The conclusion is that only a fraction of the material has the expected composition. Also, in both systems, it seems that a competition between ferromagnetic interactions and antiferromagnetic interactions occurs.

4.4   Conclusions

In this chapter photoemission and photoabsorption spectra of $M[Fe(L^1)_2]_3 \cdot 4CHCl_3$ (M = Fe, Cr) in comparison with first–principles electronic structure calculations as well as a characterization of the possible magnetic interactions which are occuring in the above mentioned magnetic molecules, is reported. Magnetic measurements were also performed on this materials, and the results were presented in this chapter. First the charge state of the Fe in these "ferric stars" was determined, in view of an existing controversy between the expected nominal valence (Fe^{3+}), from one side, and the calculated value of the Fe local magnetic moment ($4\ \mu_B$), that would imply a bivalent iron, from the other side. On the basis of a comparison of the Fe $2p$ and $3s$ photoelectron spectra with those of reference compounds, the charge state of Fe in the $FeFe_3$–star was argued to be 2^+. The valence–band X–ray photoelectron spectrum and the X–ray FeL, O and NK emission spectra show little structure but are otherwise in agreement with DFT calculations. In the $FeFe_3$– and $CrFe_3$–stars, the L_α/L_β intensity ratio in resonant X-ray emission, varies accordingly to the excitation energy on going through the Fe L_2 threshold. The trend observed in the $FeFe_3$–star is similar to that earlier reported by Yablonskikh *et al.* and Prince *et al.*, and believed to be a signature of "high–spin" structure, or more precisely of strong magnetic systems, like e.g. FeO or Heusler alloys. The explanation of this "anomalous" behavior is consistent with the assumption that the Coster–Kroning process probability is suppressed in strong magnets. The DFT calculations does indeed support an assumption of such strong magnetic behavior in the $FeFe_3$–star. However, the $CrFe_3$–star does not show such an anomalous trend in the L_α/L_β intensity, even though the local electronic structure at the Fe site remains largely the same as in the $FeFe_3$–star, and the loss of strong magnetic character appears confided to the Cr center. The magnetic interactions which occur between the transition metal ions (Fe, Cr) bridged by oxygen ligands, were studied by the means of Goodenough–Kanamori–Anderson (GKA) rules. The results are revealing a contradiction to the GKA–rules; the superexchange interaction which is accounted for the "ferric star"–single molecule magnet, giving an antiferromagnetic interaction for the

so-called 90 degrees angle. From the magnetic measurements, the paramagnetic Curie temperatures, were found to be negative for both molecules. The magnetization taken in the range of 5 K up to the room temperature, shows a rearrangement of the magnetic ordering at $\simeq 10$ K in the case of FeFe$_3$ and $\simeq 15$ K for the case of CrFe$_3$ – star molecule.

Chapter 5

Why intermetallic compounds and alloys?

The first published paper dealing with intermetallic compounds appeared in 1839, and sixty years elapsed before the field was sufficiently developed to warrant the first review paper by Neville in 1900. New results were appearing so rapidly that fifteen years later, two books were printed, devoted exclusively to this subject, one by Desch in England and one by Giua in Italy [126]. Intermetallic compounds and alloys have attracted for the last twenty years the interest of scientific community and industry due to their technological relevance as permanent magnets or as practicable hydrogen storage materials. The magnetic, mechanical, chemical and semiconducting properties of the intermetallic compounds makes them of a very high interest for studying.

- **Magnetic properties**

  The magnetic properties of para–, dia–, and ferromagnetic alloys known or suspected to contain intermetallic compounds attracted interest from the earliest times not only as a means of supporting the existence of unique compounds but also for the insights given to the fundamentals of magnetic behavior. The para–, and diamagnetic behaviors were not so unusual, but particulary intriguing results were found ferromagnets. Although intermetallic compounds, one component of which was a ferromagnet, were most frequently found to be nonmagnetic, the reverse case was found in 1903 by Heusler. He demonstrated that entirely nonmagnetic alloys of cooper and manganese are rendered magnetic by alloying with a third element such as tin or aluminium [127]. Although it was quickly established that these properties were associated with the formation of intermetallic compounds, agreement and a specific model was not readily attained. Early hypotheses were based on a supposed enhancement of the magnetic properties of the compound MnAl or on rasing the magnetic transformation temperature of elemental manganese. Many other ferromagnetic compounds comprised of nonferromagnetic elements have been discovered, both isomorphous with the Husler alloy and with other structure. Another important milestone to be marked is the suggestion of Néel [128] of the possibility of an anti-

ferromagnetically ordered state. This and a related antiferromagnetic ordering have since been found to be especially prevalent in intermetallic compounds. The ability of neutrons to interact, because of their own magnetic moment, with the moments of individual atoms in crystals, hence, to reveal the magnetic structure, has opened up a whole new field of research [126].

- **Chemical properties**

  Studies of the heats of formations of alloys were considered useful both for the determination of the existence of compounds and for the insight they gave into the strength of the interatomic bonding. Several important catalysts are are prepared by first synthesizing an intermetallic compound and then subjecting in to attack by a strong reagent. Perhaps the most famous of these is the Raney nickel prepared from NiAl intermetallics by sodium hydroxide treatment and patented by Raney in 1927 [129]. Although many intermetallic compounds are quite oxidation–, and corrosion –resistant, it was early noted in attempts to isolate intermetallic compounds by reagent attack that many were more readily attacked than the constituent elements. Indeed, many magnesides, bismuthides, and aluminides were found to disintegrate spontaneously in air [130, 131], a phenomenon rediscovered by Fitzer [132] in $MoSi_2$ in 1955 and dubbed in the "pest" effect.

- **Semiconducting properties**

  The most common and probably the most important group of semiconducting intermetallic compounds are those found between elements of group III and V of the periodic table. Although the existence of some III-V's such as AlSb an AlP were known in the nineteen century, it was not until the work of Goldschmidt in 1929 that it was appreciated that a large group of isomorphous compounds existed in this class. Semiconducting properties were first reported for the compound InSb in 1950 by Blum el al. [133] and by Goryunova [134]. The field was really opened up, however, by Welker in a paper in 1952 [135] in which he emphasized that the high carrier mobilities and wide range of band gaps available among the III-V compounds made them an important new family of semiconductors.

- **Mechanical properties**

  When one is discussing about the principal mechanical characteristics of the intermetallic compounds, their brittleness and their usual extreme hardness relative to the pure components can be taken into account. One of the first systematic studies of the mechanical properties of intermetallic compounds was performed by Kurnakov and Zhmechuzhnii [136] in 1908. The first studies of the deformation process were made by Tamman and Dahl [131] in 1928 who were also among the first to examine the temperature dependence of strength and ductility. Modern concepts of plastic behavior of crystalline solids are in terms of the structure and motion of dislocation. Koehler and Seitz [137] predicted that the ordered structure of most intermetallic compounds would require a super dislocation, that is, a pair of partial dislocation

separated by a strip of material with the ordering 180° out of phase with the normal structure. Such superdislocations were first revealed by Marcinkowski el al. [138] in electron transmission in 1960.

Chapter 6

Alloys and Intermetallic Compounds

6.1 State of the art

Growth and alloying of manganese on various substrates offers the possibility to design materials with interesting magnetic and electronic properties. Pure manganese is known to exist in four phases with different magnetic properties, and epitaxial growth of manganese on suitable substrates has proven to be a fruitful way of stabilizing particular phases [139, 140, 141, 142]. Alloying manganese with other metals yielded compounds with interesting magnetoelectronic properties ,[143, 144, 145] and its behavior as a heterogeneous catalyst may also be influenced, since Mn atoms can improve the surface reactivity or the selectivity towards particular surface reactions.

The paramagnetic behavior of pure palladium is appreciably altered by the addition of small amounts of the $3d$ metals. Addition of iron or cobalt leads to ferromagnetism [146, 147] while alloying with chromium of manganese increases the antiferromagnetic tendencies of the system [148, 149]. Several investigations were performed on the MnPd
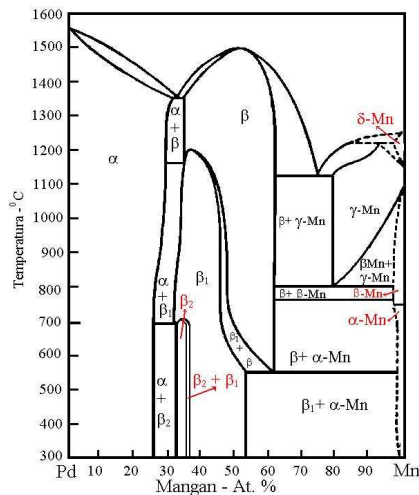

Figure 6.1: *Phase diagram of the Pd-Mn system*

system, among them neutron diffraction, inquiring into the existence of localized magnetic moments on the palladium atoms and the participation of these atoms in the magnetic exchange interactions of these alloy systems [150, 151]. The formation of superlattice in the Pd-Mn system has been reported around 3:1 composition in the α–phase region after a prolonged treatment [152]. Previous investigations had indicated that this region is devoid on any solid-state transformations [153]. A phase diagram of the Pd-Mn system is shown in Fig 6.1.

In the Mn-Pd system, different structures are possible. For instance the Pd_3Mn was found to have a fcc structure with periodic antiphase domains. The occurrence of this structure in Mn-Pd systems is of interest mainly for two reasons. In the first place, the alloy is composed of transition metals only, and not of noble metals, as in other alloys with a long period structure [154]. In the second place, the periodicity does not seem to change with a change in composition, or electron-atom ratio of the system, whereas in long-periodic superlattices of the nobel metals, the periods do change continuously as a function of the electron-atom ratio.

The study of core level and valence band photoelectron spectra of $3d$ transition metals (T) can yield important information on the electronic structure of their alloys and intermetallic compounds. Multiplet splitting in the core–level $2p$ photoelectron spectrum is directly correlated to the local magnetic moment at the transition metal sites. The localization / delocalization of the 3d valence electrons, screening, and the hybridization between $3d$ states and those of the neighboring atoms in the lattice strongly influence the core–level and valence band photoelectron spectra as well as their satellite structures.

The problem of local magnetic moments confined to the T sites, i.e., localized behavior in some aspects of itinerant d–electrons, is one of the most important issues in the physics of the magnetic alloys and intermetallic compounds. It was found experimentally that under certain conditions the magnetic moment of a transition metal remains localized when solute in another transition metal. The condition for the existence of the local moment at the transition metal site is $\pi\Delta/U < 1$, where Δ is the width of the d states (corresponds to the virtual bound states in the Fridel's model [155]) and U is the Coulomb correlation energy between d electrons [156]. The first observation of the magnetic exchange splitting in the core level Mn $2p_{3/2}$ photoelectron spectra ($\Delta_{ex} = 1.0 - 1.5$ eV) was reported on Heusler alloys [157, 158]. A prominent characteristic of these materials is their local moment character with the full magnetic moment of approximately $4\mu_B$ confined between Mn atoms. This description has been justified on the basis of the large separation between Mn atoms. It was found that both the exchange splitting and the line width of the Mn $2p_{3/2}$ peaks are closely connected to the local magnetic moment at the Mn sites determined from static magnetic measurements. In the phase diagram (see Fig. 6.1) of the Mn-Pd system there are three regions of solid solubility which comprise also four intermetallic compounds: $MnPd_3$, $Mn_{11}Pd_{21}$, Mn_3Pd_5 and MnP [159, 160, 161].

6.2   MnPd alloys

In this part of the thesis, two groups of alloys and compounds will be presented, as it follows. One group is directly related to the Mn-Pd alloys, which will include the following samples $Mn_{0.23}Pd_{0.77}$, $MnPd_3$, $Mn_{0.30}Pd_{0.70}$, $Mn_{11}Pd_{21}$, Mn_3Pd_5, $Mn_{0.42}Pd_{0.58}$ and MnPd. The second class of materials which is studied in this chapter are derived out of $MnPd_3$, where Pd is substituted by Sb as if follows: $MnPd_{3-x}Sb_x$, where x=0, 0.33 and 1. The stability of different crystallographic structures in the MnPd alloys is governed by the electron–atom ratio e/a. In $Pd_{1-x}Mn_x$ alloys there is a continuous transformation from the $AuCu_3$ (α– phase for $0.15 \leq x \leq 0.25$) structure type (cubic) to the AuCuI (β_1–phase for $0.38 \leq x \leq 0.50$) structure type (tetragonal), while passing through the tetragonally distorted periodic antiphase structure (TDPAS) (for $0.25 \leq x \leq 0.30$), tetragonal (β_2-phase $Mn_{11}Pd_{21}$) and orthorombic (β_1–phase Mn_3Pd_5) structure [162]. The common feature of the two last intermetallic compounds is that the AuCuI type unit cell is doubled in three directions due to the ordering of the Pd atoms in excess of the MnPd composition. Earlier neutron diffraction measurements pointed out that Mn–Pd alloys and compounds order antiferromagnetically with Néel temperatures and magnetic moments on Mn sites raging from approximately 200 to 825 K and 4 to $4.4\mu_B$, respectively [160].

The magnetic structure of the Mn_3Pd_5 is ferrimagnetic, the magnetic moments on the two Mn nonequivalent sites of $4.2\mu_B$ and $3.4\mu_B$ being coupled antiparallel [162]. Furthermore these studies revealed also the existence of local magnetic moments on the Pd sites ($\simeq 0.2\mu_B$) and the participation of these atoms in the magnetic exchange interactions of these alloys systems.

Previous and structural neutron diffraction studies have shown that the intermetallic compound $MnPd_3$ has an ordered fcc structure with periodic antiphase domains or a one dimensional long-period superlatice [154, 151]. The unit cell of this superlattice, based on the Cu_3Au type of order is characterized by the ratio c/a=4 of the lattice parameters with $a \simeq 3.9 \mathring{A}$. The $MnPd_3$ intermetallic compound orderes antiferromagnetically with the Néel temperature and a Mn magnetic moment of aboout 200 K and 4 μ_B, respectively. These studies revealed also the existence of magnetic moments on the Pd sites ($\simeq 0.2\mu_B$) and the participation of these atoms in the magnetic exchange interactions in this compound, namely Mn and Pd near-neighbor magnetic moments are aligned antiparallel. This interaction is in a good agreement with the general rules of coupling between the neighboring local moments, whose sign depends on the occupation fraction of the d–orbitals.

The electronic structure of Mn–Pd alloys and compounds, together with the effects of the substitution of Sb for Pd in $MnPd_3$ is studied, using x–ray photoelectron spectroscopy. The results are discussed in relation with their crystallographic and magnetic properties. As main results, I found that the $Mn2p_{3/2}$ line consists of two features that are separated by approximately 1.1 eV in the binding energy (BE). These two components arise from the exchange interactions between the core hole and the valence electrons, giving a direct evidence of the existence of local moments in Mn_xPd_{1-x} alloys and compounds. The relative intensities of these components vary depending on the Mn atomic environment, reflecting the changes in the properties of the Mn 3d states by modifying the Mn concentration in

the alloy. This is the second observation of magnetic exchange splitting of Mn 2p spectrum in bulk metallic systems after the first one reported on Heusles alloys [157].

6.2.1   Samples description

6.2.1.1 Mn_xPd_{1-x}

Seven Mn-Pd alloys and compounds (see Table 6.1) were prepared by argon arc melting. The samples were melted repeatedly (four times) in the same atmosphere to ensure

Alloys and Compounds	Structure Type	Pearson Symbol	a(Å)	b(Å)	c(Å)	No. of neighbors of a Mn atom and distances d_{Mn-Mn} and d_{MnPd}	No. of neighbors of a Pd atom and distances d_{Pd-Pd} and d_{Pd-Mn}
$Mn_{0.23}Pd_{0.77}$	Cu_3Au	cP4	3.902	–	–	12 Pd–2.75 Å	4 Mn–2.75 Å 8 Pd–2.75 Å
$MnPd_3$	Cu_3Au–TDPAS	tI16	3.931	3.913	15.496	12 Pd–2.76 Å	4 Mn–2.76 Å 8 Pd–2.76 Å
$Mn_{0.30}Pd_{0.70}$	Cu_3Au TDPAS	tI16	3.93	3.93	15.05	1 Mn–2.78 Å 11 Pd–2.72 Å	4.33 Mn–2.76 Å 7.67 Pd–2.76 Å
$Mn_{11}Pd_{21}$	$Mn_{11}Pd_{21}$	tP32	8.061	8.061	7.33	2.75 Mn–2.85 Å 9.25 Pd–2.74 Å	4.2 Mn–2.82 Å 7.8 Pd–2.75 Å
Mn_3Pd_5	Ga_3Pt_5	oC16	8.072	7.279	4.044	3 Mn–2.79 Å 9 Pd–2.70 Å	5.33 Mn–2.72 Å 6.67 Mn–2.80 Å
$Mn_{0.42}Pd_{0.58}$	CuAu	tP4	4.041	4.041	3.636	≃4 Mn–2.86 Å ≃8 Pd–2.72 Å	≃8 Mn–2.71 Å ≃4 Pd–2.86 Å
MnPd	CuAu	tP4	4.069	4.069	3.585	4 Mn–2.87Å 8 Pd–2.71 Å	8 Mn –2.71 Å 4 Pd–2.88 Å

Table 6.1: *Structure types, lattice constants, average numbers of neighbors of a Mn and Pd atom and the distances Mn–Mn, Mn–Pd and Pd–Pd for Mn_xPd_{1-x} alloys and compounds*

homogeneity.

The weight loss of the final samples was found to be <1%. The purity of the starting materials was 99.99% for Mn and Pd. X- ray diffraction measurements (XRD) showed that all the samples are single phases with the expected structure types. As an example , in Fig.6.2 are shown the x-ray diffraction pattern for five examples $MnPd_3$, $Mn_{0.23}Pd_{0.77}$, $Mn_{0.30}Pd_{0.70}$, Mn_3Pd_5 and $Mn_{0.42}Pd_{0.58}$. The lattice parameters are in agree with those reported in the literature [160, 151]. Each Mn and Pd atom in all investigated samples are sourrounded by twelve nearest-neighbors of Mn and Pd atoms, whose relative numbers are
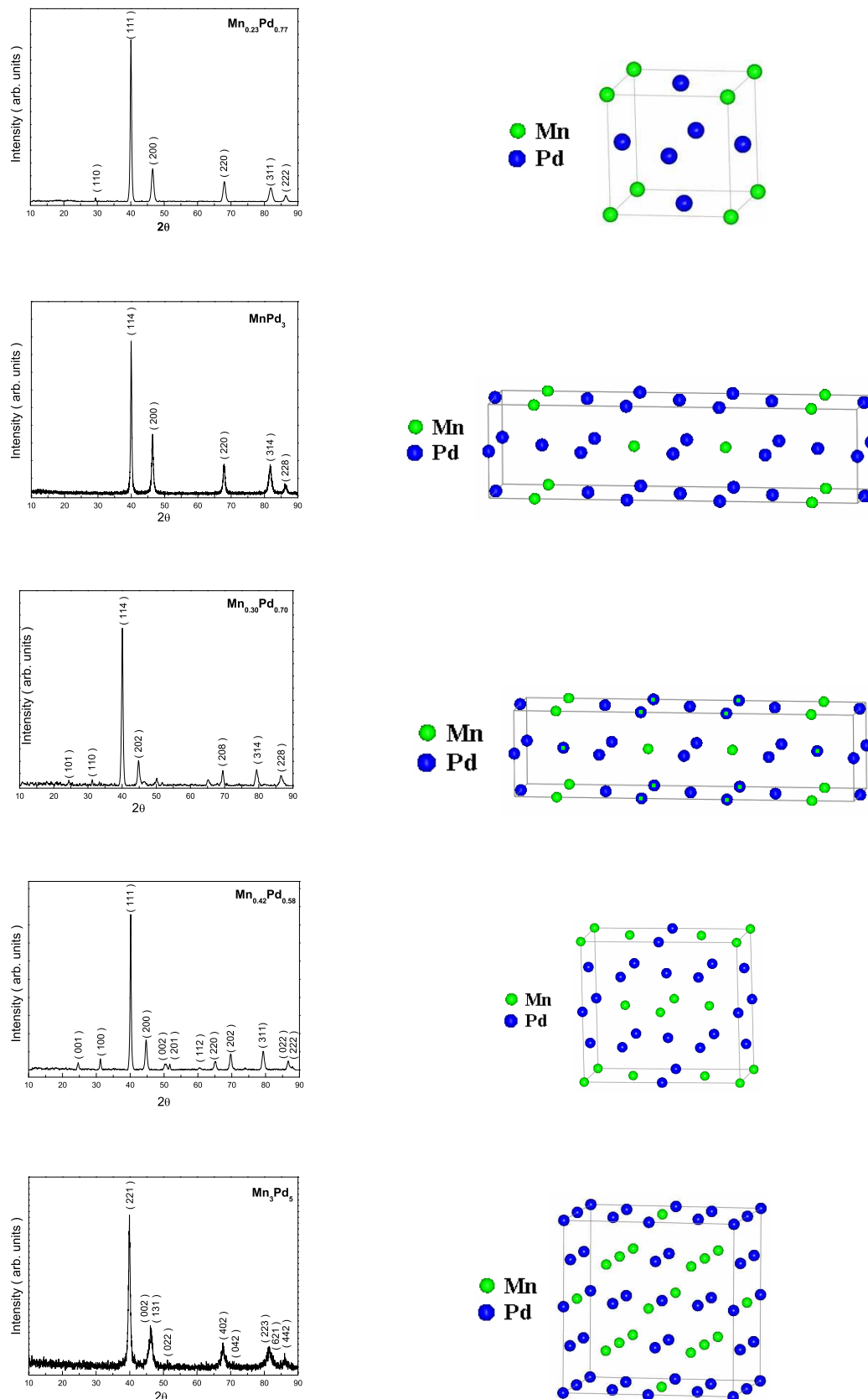
Figure 6.2: *X-ray diffraction pattern of MnPd$_3$, Mn$_{0.23}$Pd$_{0.77}$, Mn$_{0.30}$Pd$_{0.70}$, Mn$_3$Pd$_5$ and Mn$_{0.42}$Pd$_{0.58}$*
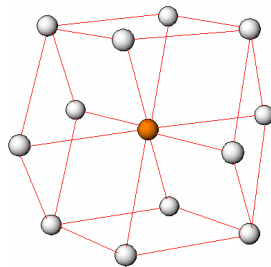
Figure 6.3: *Geometrical nearest neighbourhood of Mn and Pd atoms*

changing with the increase of the Mn concentration (see Fig. 6.3). In Table 6.1 are given the averege numbers of Mn and Pd neighbors of a Mn and Pd atom in the crystalline lattice and the corresponding distances Mn–Mn, Mn–Pd and Pd–Pd. The non-integral numbers of neighbors for some alloys and compounds resulf from different crystallographic sites of Mn and Pd atoms in the elementary cells. As it was mentioned before, in the Mn_xPd_{1-x} alloys and compounds there is a continuously transformation regarding the crystallographic structure (see Fig. 6.2).

6.2.1.2 $\mathbf{MnPd_{3-x}Sb_x}$

In the structure type which is characteristic for the $MnPd_{3-x}Sb_x$ intermetallic compound, a Mn atom is surrounded by twelve Pd atoms and a Pd atom by four Mn and eight Pd atoms respectively. The negative polarization of the Pd 4d band is induced by the exchange interactions with the Mn spins. The total magnetic moment per unit cell at 0 K per unit cell is zero. Five $MnPd_{3-x}Sb_x$ (x=0; x=0.33; x=0.67; x=0.84 and x=1.0) alloys and compounds were prepared by argon melting. The samples were melted repeatedly in the same atmosphere to ensure homogeneity. The weight loss of the final samples was 99.99% for all the components. X-ray diffraction measurements (XRD) showed that all the samples are single phased with the lattice parameters give in Table 6.2.

x	a(nm)	b(nm)	c(nm)
0.00	0.3913	0.3913	1.5496
0.330	0.3953	0.3953	1.5685
0.67	0.6300	0.6300	0.6300
0.84	0.6362	0.6362	0.6362
1	0.6429	0.6420	0.6420

Table 6.2: *Lattice parameters of $MnPd_{3-x}Sb_x$ alloys and compounds*

A change in the crystallographic structure takes place of 0.33<x<0.67, i.e. from $MnPd_3$ to the Heusler alloys structure type. The lattice parameters for $MnPd_3$ and $MnPd_2Sb$ Heusler alloy agree with those reported in the literature [163].

6.2.2 Magnetic measurements

6.2.2.1 Mn_xPd_{1-x}

The magnetic measurements were performed with a vibrating magnetometer in the temperature range of 4.2–850 K and fields up to 90 kOe. All the magnetic measurements were carried out at the University of Babes–Bolyai, Cluj–Napoca–Romania, at the Physics Department. The results on Mn_xPd_{1-x} alloys and compounds confirm earlier data obtained from neutron diffraction studies [162, 164] and susceptibility measurements [159, 164] concerning the values of the Néel temperatures T_N, paramagnetic Curies temperatures Θ and the effective magnetic moments per unit formula. The temperature dependence of the susceptibility for Mn_3Pd_5 and the temperature dependence of the reciprocal susceptibility for $Mn_{11}Pd_{21}$, $MnPd_3$, and Mn_3Pd_5 are presented in Fig.6.4. With respect to the magnetic
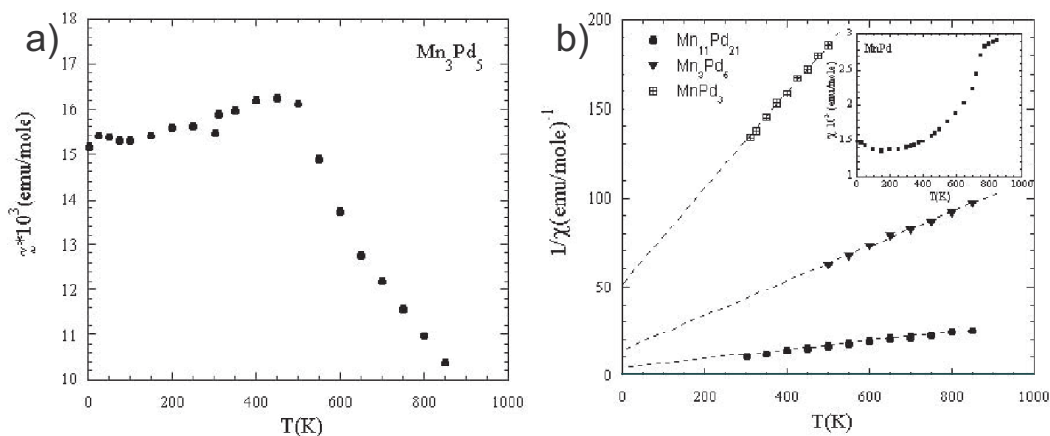
Figure 6.4: *a) Temperature dependence of the magnetic susceptibility of Mn_3Pd_5; b) Reciprocal susceptibility for $Mn_{11}Pd_{21}$,Mn_3Pd_5 and $MnPd_3$*

behavior of the Mn_3Pd_5 intermetallic compound, the results presented in this work are more closer to those obtained by Kjekshus *el al.* [159] than those reported by Kádár *et al.* [161]. The magnetic properties of this compound are very sensitive to the crystallographic order. A small deviation of the order parameter S from unity leads to an interchange of some Mn atoms with Pd ones, which does not change the antiferromagnetic alignment of Mn moments, but gives in average the same number of the nearest neighbor Mn atoms around the sites 2(a) and 4(h) from the crystallographic superstructure, resulting an antiferromagnetic behavior of this compound. The close relation between the ferromagnetic and antiferromagnetic $Mn_3Pd_5{\equiv}Mn_{0.375}Pd_{0.625}$ structures is demonstrated by the small differences between the ordering temperatures of the two phases. In Fig. 6.5 are presented the values of the Néel temperatures for Mn_xPd_{1-x} which were reported earlier in the literature and the values which we have obtained determined from the magnetic measurements. The trend is the same and shows an abrupt increase of the Néel temperature at Mn concentrations for which the crystallographic structure is changed from cubic Cu_3Au to a
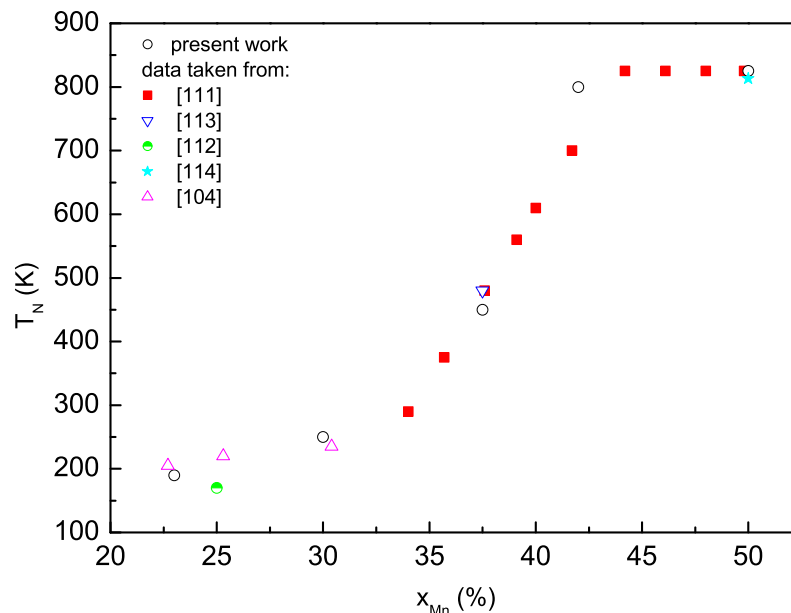
Figure 6.5: *Néel temperatures as a function of Mn concentration for Mn_xPd_{1-x} alloys*

tetragonal CuAuI structure type. The result is constituent with the increase of Mn–Mn near-neighbor pairs as the Mn concentration increases (see Table 6.1). Previous neutron diffraction measurements have evidenced an induced negative magnetic moment on Pd sites in all Mn_xPd_{1-x} alloys and compounds, whose values decreases gradually as the Mn concentration increases. The antiferromagnetic interaction is the predominant interaction in the Mn_xPd_{1-x} alloys and compounds between both near-neighbor Mn and Pd atoms and Mn–Mn pairs. The Mn–Mn interaction takes place only when the distance between the atoms is smaller than about $3\overset{\circ}{A}$ [159]. From the slope curves $1/\chi(T)$ for $T>T_N$ we have determined the values of the effective magnetic moment, which revealed spin fluctuations on the Pd sites. In the case of pure Pd, the susceptibility exhibits a peculiar temperature variation that shows a broad maximum in the vicinity of 80 K [165]. The reason for this is because of the high exchange enhancement with the Stoner enhancement factor of 9.3. The number of holes per atom in the Pd 4d band was determined also, and it was found to be equal to 0.36 [166]. This behavior may be explained in the frame of the spin fluctuation model [167] in the followings. The effective magnetic moment for $MnPd_3$ has the value μ_{eff}=5.38 μ_B/f.u. and taking μ_{eff}=4.9μ_b/Mn for a total spin S=2, evaluated from the neutron diffraction studies, results the contribution μ_{eff}=1.28μ_b/Pd of these atoms to the measured magnetic susceptibility in the paramagnetic state. From this value it was estimated a number of about 0.6 holes per atom in its 4d band. The same result regarding the number of conduction electrons per Pd atom in the $MnPd_3$ was determined by Sato *et*

al. [160].

6.2.2.2 MnPd$_{3-x}$Sb$_x$

For the case of MnPd$_{3-x}$Sb$_x$, the data for x=0.33; 0.67 and 0.84 will be presented, in comparison with the parent compound MnPd$_3$.

MnPd$_{2.67}$Sb$_{0.33}$

The temperature dependence of the spontaneous magnetization and of the reciprocal susceptibility of MnPd$_{2.67}$Sb$_{0.33}$ are presented in Fig 6.6 respectively in Fig 6.7. The values and variations of magnetization of MnPd$_{2.67}$Sb$_{0.33}$ with magnetic field and temperature suggest that this alloy has a ferrimagnetic behavior below the Curie temperature T$_c$=304K, determined from the usual Arrot plot. This is a clear evidence of a change in the magnetic
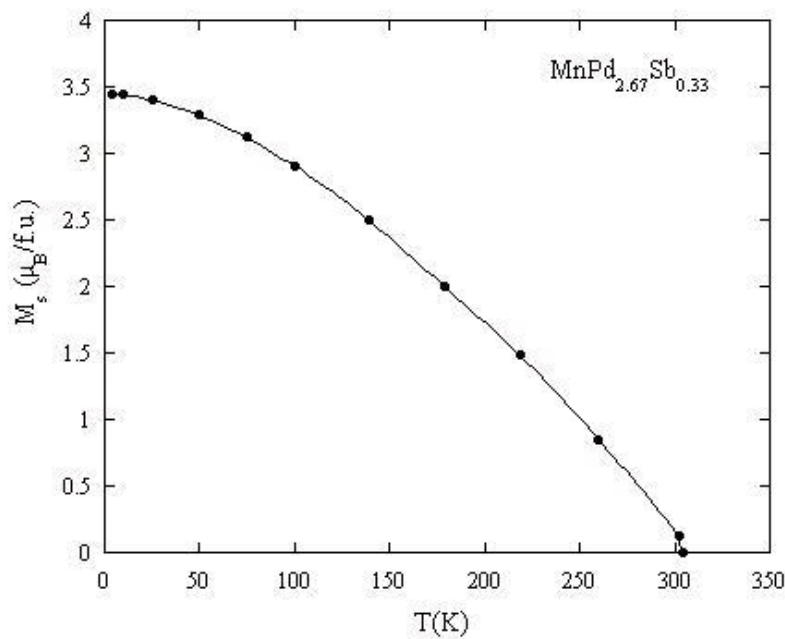
Figure 6.6: *Thermal variation of the spontaneous magnetization MnPd$_{2.67}$Sb$_{0.33}$*

structure of MnPd$_{2.67}$Sb$_{0.33}$ relative to that of MnPd$_3$ i.e., the magnetic sublattices of Mn and Pd magnetic moments are oriented antiparallel as it can be seen in Fig. 6.7

The spontaneous magnetization extrapolated to 0 K has the value of 3.44 μ_B/f.u., smaller than 4 μ_B/mn, determined by neutron diffraction measurements in the parent compound MnPd$_3$. In the temperature range 500-900 K, the magnetic susceptibility obeys the Curie–Weiss law, χ=C/(T-Θ), with the paramagnetic Curie temperature Θ=246 K. The deviation of the experimental points from the linearity in the vicinity of T$_c$ confirms the ferrimagnetic behavior of these alloys. The effective magnetic moment, determined from the Curie constant, C has the value 4.65 μ_b/f.u.. The correlation of the experimental
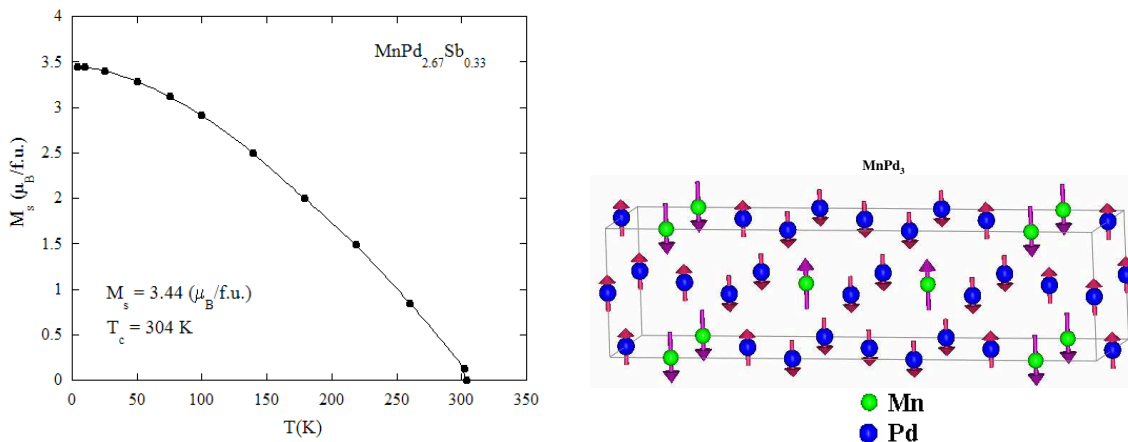
Figure 6.7: *In the left panel is presented the temperature dependence of the reciprocal susceptibility for $MnPd_{2.67}Sb_{0.33}$; in the right panel is presented the orientation of the magnetic moments in $MnPd_3$*

data obtained both from ordered and paramagnetic states, leads to the following values for the magnetic moments and the effective magnetic moments per Mn and respectively Pd atom: μ=3.71 μ_B/Mn; μ=0.1 μ_B/Pd and μ_{eff}=4.59 μ_B/Mn; μ_{eff}=0.46 μ_B/Pd. All of these values are smaller than those found in the $MnPd_3$ parent compound, suggesting a partial filling of the Mn 3d and Pd 4d bands. The bands filling takes place by the hybridization of both Mn 3d and Pd 4d states with Sb 5p states, confirmed by the XPS spectra.

$MnPd_{2.33}Sb_{0.67}$ & $MnPd_{2.16}Sb_{0.84}$

The temperature dependence of the spontaneous magnetization and of the reciprocal susceptibility of $MnPd_{2.33}Sb_{0.67}$ are presented in Fig. 6.8. This alloys shows also a ferrimagnetic behavior with the Curie temperature T_c=156 K, but the value of the spontaneous magnetization is much smaller, namely $M_s(0)$=1.3 μ_B/f.u., which suggests a new change in the magnetic structure accompanied by a change in the crystallographic structure. The $MnPd_{2.33}Sb_{0.67}$ alloy and $MnPd_{2.16}Pd_{0.84}$ have the same crystallographic structure as $MnPd_2Sb$ Heusler alloy, but with smaller lattice parameters. The high value of the effective magnetic moment, μ_{eff}=5.56 μ_B/f.u., suggests that in the ordered state of $MnPd_{2.33}Sb_{0.67}$ alloy the magnetic moments of Mn atoms have also a high value and the observed saturation magnetization results from a canted antiferromagnetism which leads to a ferrimagnet behavior. This is confirmed by the negative value of the paramagnetic Curie temperature, Θ =-70 K. In this system there is a coupling of the d states via the conduction band electrons (RKKY interaction) and an indirect Mn–Pd–Mn exchange, involving the d electrons. The ferromagnetic and antiferromagnetic states are close in energy even in $MnPd_3$ compound [168], so that the competition between different magnetic ordering is to be aspected also in the $MnPd_{3-x}Sb_x$ alloy system. As the Sb concentration is increasing, when approaching the ideal structure of $MnPd-2Sb$ Heusler alloy, the ferromagnetic
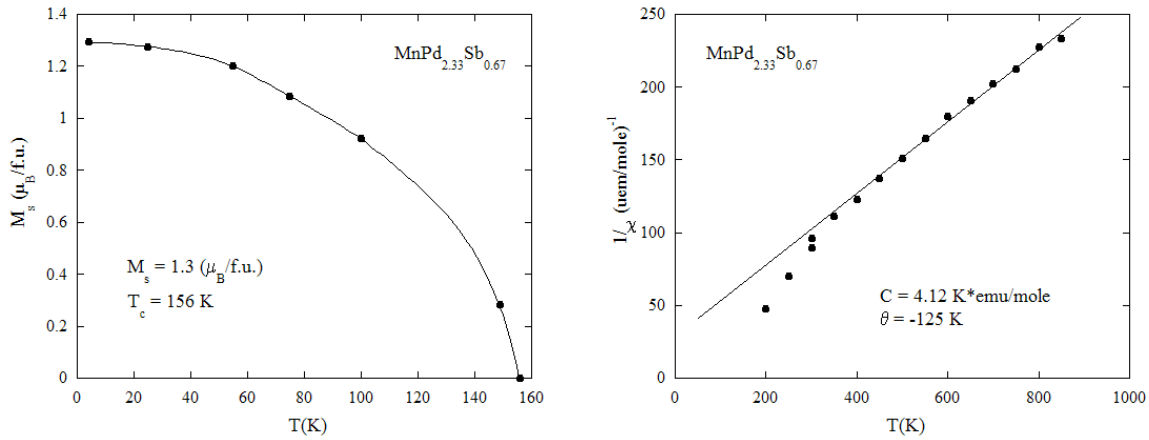
Figure 6.8: *In the left panel: Thermal variation of the sponetaneous magnetization of $MnPd_{2.33}Sb_{0.67}$; In the right panel: Temperature dependence of the reciprocal susceptibility for $MnPd_{2.33}Sb_{0.67}$*

alognment of Mn moments is energetically more favorable, as one can see from the values of the spontaneous magnetization $M_s(0)$=3.22 μ_B/f.u. and Curie temperature T_c=224 K for $MnPd_{2.16}Sb_{0.84}$ alloy (Fig. 6.9),
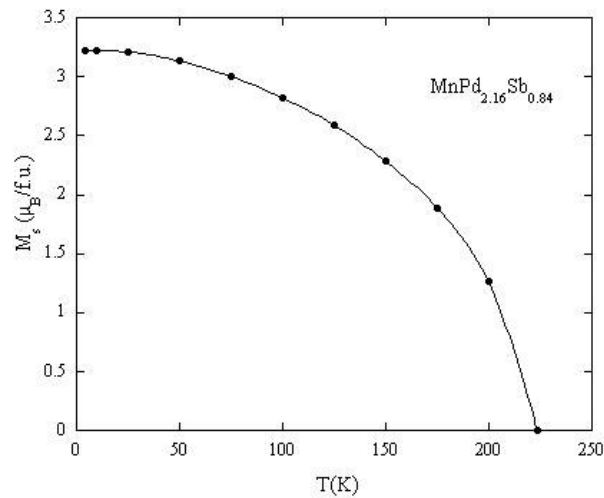
Figure 6.9: *Thermal variation of the spontaneous magnetization for $MnPd_{2.16}Sb_{0.84}$*

which are close to those found in Heusler $MnPd_2Sb$, namely 4.4 μ_B/f.u. and 247 K, respectively [163].

6.2.3   XPS measurements

6.2.3.1 Mn_xPd_{1-x}

For proving the good quality of the samples which were studied, in Fig. 6.10 is presented the survey spectrum with the identification of all core–level lines for the $Mn_{0.23}Pd_{0.77}$ alloy.
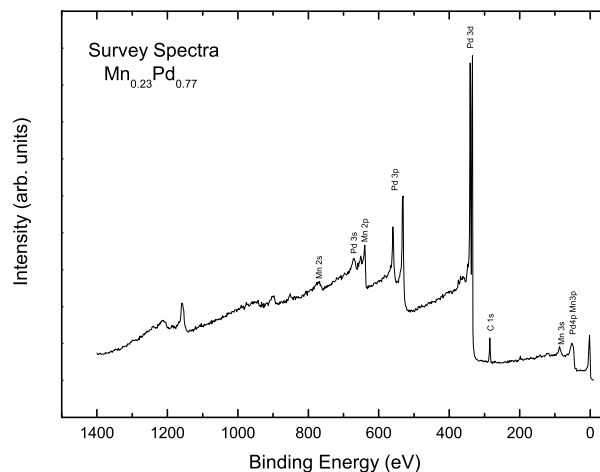
Figure 6.10: *Survey spectrum for $Mn_{0.23}Pd_{0.77}$*

At 284.5 eV, a small contamination can be observed, this is due to a very sensitive surface, and contamination in situ. The Mn 2p spectra for Mn_xPd_{1-x} alloys and compounds are shown in Fig. 6.11. The observed spin–orbit splitting, which can be identified in the distance between the two centers of energy of the $2p_{3/2}$ and $2p_{1/2}$ states is Δ_{sp}=11.5 eV. Both of these states are accompanied by broad features at about 5 eV towards higher binding energies. The whole spectrum may be explained if we assume more than one $3d^n$ final state configuration. The ground state is formed mainly out of the $3d^6$ state with a small admixture of $3d^5$ configuration, representing states of local moments in the Andreson's model [156, 167].

This assumption is consistent with the values of the magnetic moments, which are a little higher than $4\mu_B$/Mn. Upon creation of a 2p core hole one may expect thus a well screened state $2p^53d^6$ and a poorly screened $2p^53d^5$ final state. Focusing on the states associated with $2p_{3/2}$ ionization, there are structures between 639–641 eV and a broad feature at 645 eV. Similar results were reported for Mn 2p core–level photoelectron spectra on Mn thin films deposited on Ag(100) [169], Ni(110) [170], Cu(100) [171], and Pd(100) [172]. A c(2x2) structure of Pd–Mn alloy on Pd(100) was obtained by room temperature deposition of about one monolayer Mn followed by heating to 570 K for about three minutes. This structure corresponds to a MnPd terminated $MnPd_3(100)$ compounds,
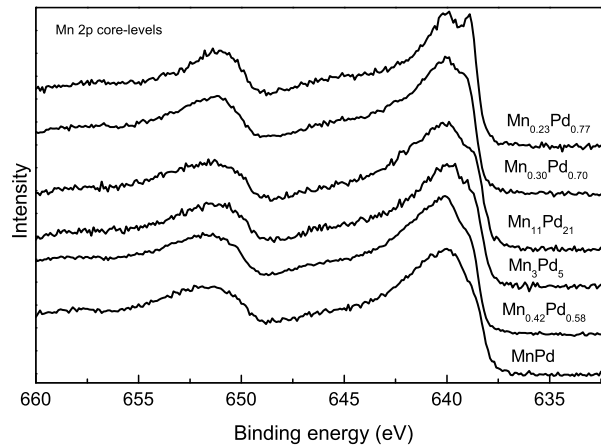
Figure 6.11: *XPS Mn $2p_{3/2}$ and $2p_{1/2}$ core level spectra of Mn_xPd_{1-x} alloys and compounds*

which has a Cu_3Au structure. A large magnetic moment was derived for the Mn monolayer ($\simeq 4\mu_B$), similar to those found for Mn atoms in Mn_xPd_{1-x} alloys and compounds. For all compounds, the 5 eV satellite located at 645 eV was assigned to a $2p^5d^5$ final state configuration whereas the main line at 640 eV was associated with $2p^53d^6$ final state configuration. The main line from Mn 2p at the binding energy of 640 eV consists of two features that are separated by $\Delta_{ex} \simeq 1.1$ eV. The analysis of the line–shape shows that the Mn 2p spectra of Mn_xPd_{1-x} alloys and compounds can be interpreted as consisting of exchange–split components. The two lower binding energies components of the Mn $2p_{3/2}$ line arise from the exchange interactions between the core hole and the valence electrons. The high– and low–binding energies correspond to the majority and minority spin core hole states respectively and the energy separation between them, Δ_{ex} corresponds to the exchange splitting of the Mn 2p core–holes states. This is a proof of local moments in the Mn_xPd_{1-x} alloys and compounds. The relative intensities of these states vary depending on the Mn atomic environment, reflecting the changes in the properties of the Mn 3d states. The line–width are closely connected with the amount of exchange multiplet splitting in the Mn $2p_{3/2}$ sublevels, as in the case of Heusler alloys [157, 158].

In Fig. 6.12 is shown the Pd 3d XPS spectra for Mn_xPd_{1-x} alloys and compounds. As the Mn concentration is increasing in the Mn_xPd_{1-x} alloys and compounds, the XPS spectra are shifted to higher binding energies. Core-level chemical shifts in XPS spectra are usually related to be due to the charge–transfer between atoms [173]. When one is dealing with intermetallic compounds the charge–transfer is smaller so the contribution to the chemical shifts from this source is smaller [166]. The increase of the binding energy of the Pd 3d peaks is an effect of the bounding of the Pd atoms to the Mn atoms. The magnitude of the Mn induced shift of the Pd 3d peak depends on the Mn concentration in the surrounding of the ionized Pd atom. The same results were obtained from the study

on Mn thin film of different thickness deposited on Pd. This results were explained by
using the Born–Haber cycle [174].
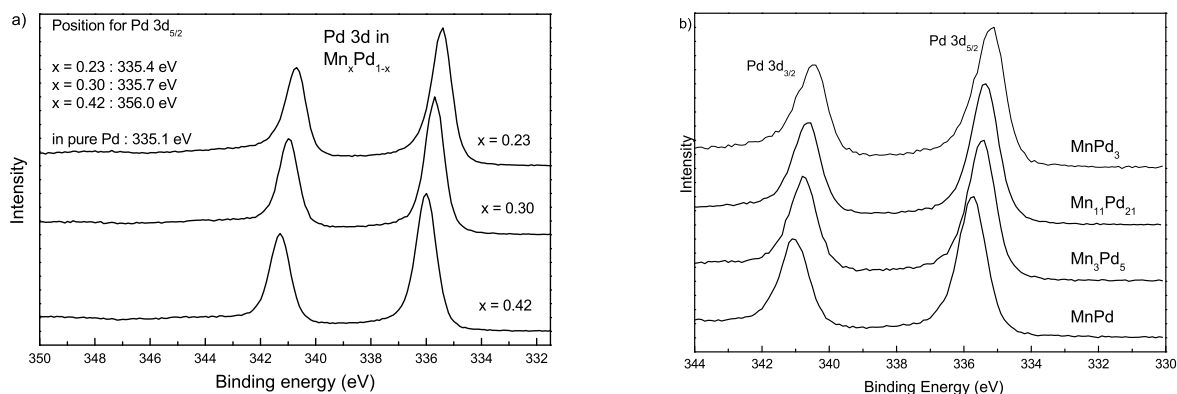
Figure 6.12: *a) Pd 3d XPS spectra for Mn_xPd_{1-x}; b) Pd 3d XPS spectra for Mn–Pd
intermetallic compounds*

This behavior may be interpreted in the terms of the $Z + 1$ approximation taking
into account the difference in the heats of solution of Pd and Ag, which is the $Z + 1$
correspondence to Pd and represents the fully screened core–ionized final state [175].

The XPS valence band spectra for Mn_xPd_{1-x} alloys and compounds are presented in
Fig. 6.13 . For the Al K_α radiation, the Pd 4d cross section is about eleven times larger
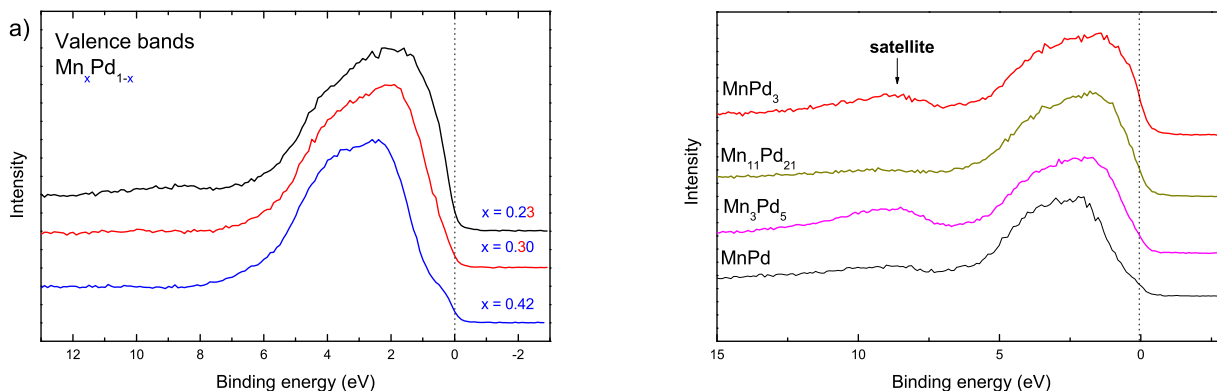
Figure 6.13: *a) XPS valence–band spectra of Mn_xPd_{1-x} alloys; b) XPS valence–band spectra
of Mn–Pd intermetallic compounds*

than the Mn 3d cross section [176], i.e. the spectra for Mn_xPd_{1-x} alloys and compounds
are dominated by the Pd 4d states. The valence band centroids are shifted towards higher

binding energies, the density of states (DOS) at Fermi level decreases and a shoulder at E_F becomes visible as the Mn concentration increases. For the majority of the investigated samples, one can observe satellite structures at about 8.5 eV, separated by approximately 6 eV from the centriods of the valence bands.

6.2.3.2 $\mathbf{MnPd_{3-x}Sb_x}$

The Mn 2p core–level spectra for $MnPd_{3-x}Pd_x$ alloys and compounds is presented in Fig. 6.14. The distance between the two centers of energy of the $2p_{3/2}$ and $2p_{1/2}$
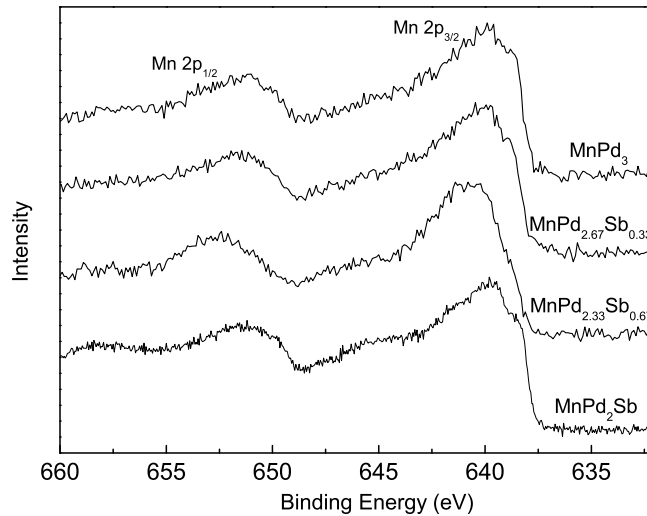
Figure 6.14: *Mn $2p_{3/2}$ and $2p_{1/2}$ XPS core–level spectra of $MnPd_{3-x}Sb_x$ alloys and compounds*

states gives the spin–orbit splitting which is $\Delta_{sp} = 11.5eV$. The main lines at about 640 eV are consistent from two lines which are separated by $\Delta_{ex} \simeq 1.1$ eV. The line–shape analysis shows that the Mn 2p spectra of $MnPd_{3-x}Sb_x$ alloys and compounds can be interpreted as consisting of exchange–split components. The two lower–binding energy components of the Mn $2p_{3/2}$ line arise from the exchange interactions between the core hole and the valence electrons. In this picture, the high– and low– binding energy components correspond to the majority– and minority–spin core–hole states respectively and the energy separation between them, Δ_{ex}, corresponds to the exchange splitting of the Mn 2p core–holes states. This gives direct evidence of the existence of local moments confined on Mn sites in $MnPd_{3-x}Sb_x$ alloys and compounds. The relative intensities of these states vary depending on the Mn atomic enviroment, reflecting the changes in the properties if the Mn 3d states. The line–widths are closely connected with the amount of exchange multiplet splitting in the Mn $2p_{3/2}$ sublevels, as in the case of Heusler [158] and Mn_xPd_{1-x} alloys [177].

In Fig. 6.15 are presented the Pd 3d XPS spectra for x=0; x=0.33, and x=0.67. One can observe that the spectra are shifted to higher binding energies as the concentration of Sb is increasing.
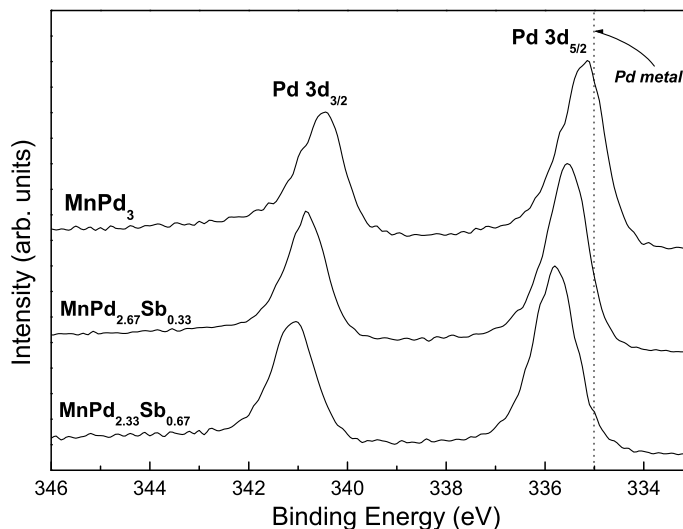
Figure 6.15: *Pd 3d XPS spectra of $MnPd3 - xSb_x$ for x=0; x=0.33, and x=0.67*

As it was discussed in the case of Mn_xPd_{1-x}, the chemical shifts for the intermetallic compounds are not realted to the charge transfer, because this is smaller so than the contribution to the chemical shifts in this compounds is an effect of the bonding to Mn atoms and Sb atoms. The magnitude of the Mn and Sb induced shift of the Pd 3d peak depends on the Mn and Sb concentration in the vicinity of the ionized Pd atom. This was also confirmed in the study which was presented above for the case of Mn_xPd_{1-x} and also for the different deposited Mn thin films of different thickness deposited on Pd [172]. As for Mn_xPd_{1-x} this behavior can be interpreted in terms of $Z + 1$ approximation taking into account the difference in the heats of solution of Pd and Ag, which is the $Z + 1$ correspondence to Pd and represents the fully screened core–ionized final state.

In Fig. 6.16 the XPS valence–band for $MnPd_{3-x}Pd_x$ alloys and compounds are presented.

The spectra for $MnPd_{3-x}Sb_x$ alloys and compounds are dominated by the Pd 4d states, the reason for this is that the Pd 4d cross section is about eleven times larger than that of the Mn 3d cross section [176]. As for the case of Mn_xPd_{1-x}, the valence–band centroids are shifted towards higher binding energies. The density of states (DOS) at the Fermi level decreases and a shoulder near to the Fermi level becomes visible as the Sb concentration increases. At about 8.5 eV in the valence–band spectra one can observe, for small concentrations of Sb, a satellite which is separated by approximately 6 eV from the centroids of the valence–band. The structure of this satellite is diminished for the x=0.33 in com-
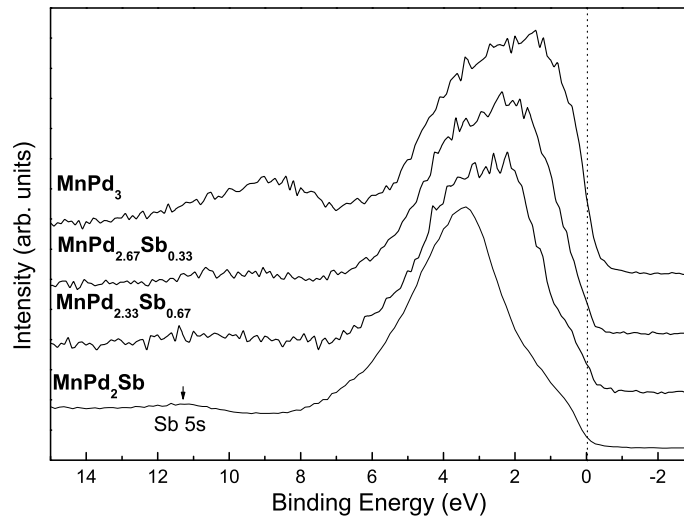
Figure 6.16: *XPS valence–band spectra of $MnPd_{3-x}Sb_x$ alloys*

parison to that observed in $MnPd_3$ and disappears for the samples with a concentration higher than x=0.67. The presence of the satellite structure at about 6 eV distance from the valence–band centroids, similar to the 6 eV satellites of pure Ni and its alloys [166], may be caused by the enhanced electron correlation in the Pd 4d band. These results are in agreement with the neutron diffraction and magnetic measurements, concerning the existence of magnetic moments on Pd atoms both in the ordered and paramagnetic state of $MnPd_3$ [178, 177]. A tendency of Sb to fill the Pd 4d band is evident with the increasing of the Sb concentration, and in the same time the shifts in the binding energies to higher values is a proof of this tendency. The band calculations have shown that the Sb 5d states in the metallic states spread down to 6 eV from the Fermi level [179] and in all Pd alloys and compounds there is always Pd 4d character in the bands above Fermi level [166]. This is a futher evidence that the filling of the Pd 4d bands takes place by hybridization of the Sb 5p levels and Pd 4d states. The spectra feature located around 11 eV is assigned to the Sb 5s states [179].

6.2.4　Computational results

$\mathbf{Mn}_x\mathbf{Pd}_{1-x}$ In order to have a clear imagine of the partial and total density(DOS) of states, and for a better interpretation of the XPS valence–band, DOS calculations were performed on this groups of materials. The partial and total density of states was calculated for $Mn_{0.23}Pd_{0.77}$, $MnPd_3$ and $MnPd$ using the TB-LMTO method [180].
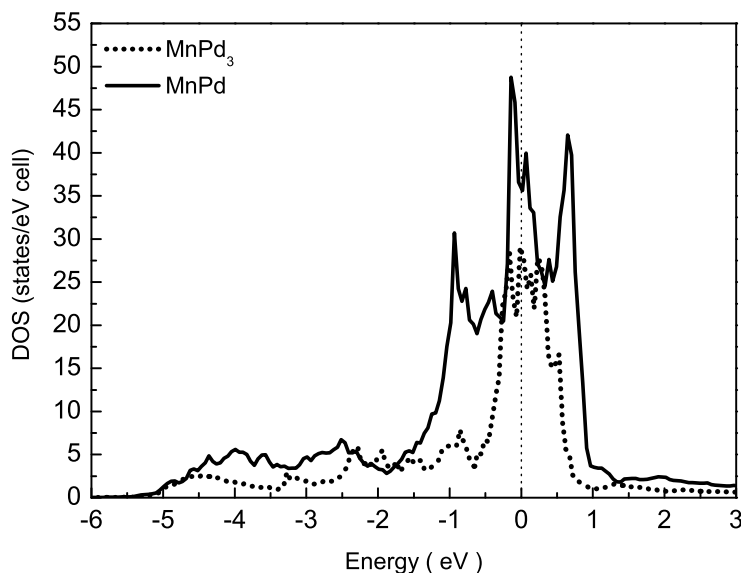
Figure 6.17: *Calculated PDOS of Mn 3d from MnPd and MnPd₃*

The basic set includes s, p and d orbitals for Mn and s, p, d and f orbitals for Pd. The Wigner–Seitz radius was scaled to that the total volume of all spheres equals that of the unit cell: Mn–2.961 a.u., Pd_I–2.793 a.u. and Pd_{II}–2.961 a.u. (for $MnPd_3$). The potentials were self–consistently obtained by performing self–consistent iterations on a mesh of 275 k–points in the irreductible part of the Brillouin zone. The *ab initio* calculations were modelled in such a way that the three compounds have the same number of atoms per cell. The calculated total density of states for $Mn_{0.23}Pd_{0.77}$ and $MnPd_3$ are practically the same, but for the MnPd compounds some differences are to be noted. In Fig. 6.17 are presented the Mn 3d partial density of states for MnPd and $MnPd_3$ intermetallic compounds. The strongly enhanced magnetic moments, confided on Mn sites in Mn_xPd_{1-x} compounds and alloys is explained by the fact that at the Fermi level the Mn 3d partial density of states is very high, as opposed to the itinerant low–spin ground state formed in Mn metal.As it was expected, both the partial density of states at the Fermi level and the Mn 3d bandwidth are larger for MnPd in comparison with $MnPd_3$ due to the presence of four Mn–Mn pairs in the nearest neighborhood for the first compounds and none for the second one. These data confirm the magnetic data concerning the values of the magnetic moments and the

Néel temperature for these compounds. As the concentration of the Mn is increasing in the Mn_xPd_{1-x} a shoulder apeare at the Fermi level, this can be attributed to the states with mainly Mn 3d character.

In Fig 6.18 the Pd 4d partial density of states for $MnPd_3$ and MnPd is presented.
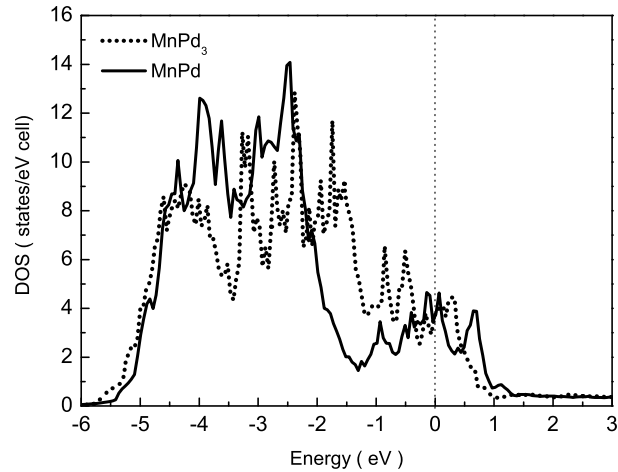
Figure 6.18: *Calculated PDOS of Pd 4d from MnPd and MnPd$_3$*
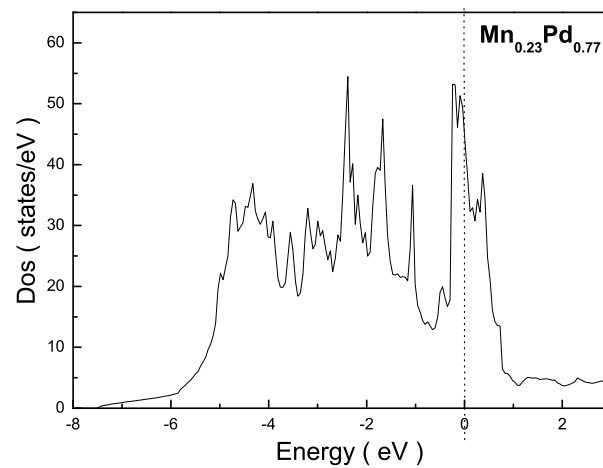
Figure 6.19: *Calculated tDOS for $Mn_{0.23}Pd_{0.77}$*

As it can be seen in the plotted spectra, the centers for the Pd 4d bands is shifted towards higher binding energies, for both of the elements MnPd and $MnPd_3$. This effect is more pronounced for the case of MnPd, and the density of states is smaller as compared to the pure Pd. This indicates that the 4d states are more localized and that there is a tendency for Mn to fill in the Pd 4d bands.

In Fig. 6.19 the total density of states for $Mn_{0.23}Pd_{0.77}$ is presented. The calculations for $Mn_{0.23}Pd_{0.77}$, $MnPd_3$ and MnPd indicate that there is always Pd 4d character in the bands above the Fermi level, which is further evidence that the filling of the Pd 4d bands takes place by hybridization of the Mn and Pd states. This explains also the shifts of the valence–band centroids towards higher binding energies as the Mn concentration is increased. The presence of the satellite at about 6 eV distance from the valence–band centroids, may be caused by the enhancement electron correlation in the pd 4d band. This result is constituent with the neutron diffraction and magnetic measurements concerning the existence magnetic moments on Pd atoms both in the ordered and paramagnetic state

6.2.5   Conclusions

Joint investigations on the electronic structure and accurate magnetic measurements were performed on the Mn_xPd_{1-x} and $MnPd_{3-x}Sb_x$ alloys and compounds.

Mn_xPd_{1-x}

In order to study the electronic structure of these materials, XPS measurements were carried out. For the Mn 2p core–level photoemission in the Mn_xPd_{1-x} alloys and compounds a remarkable split structure is visible, which is arising from the exchange interactions between the core hole and the open 3d shell. This gives a clear evidence of local magnetic moments confided on Mn sites in the Mn_xPd_{1-x} alloys. An energy split was found in the Mn $2p_{3/2}$ line, which is about 1.1 eV. This splitting is characteristic for these kind of materials. The relative intensities of the two components (splitting components) vary depending on the Mn atomic environment, reflecting the changes in the properties of the Mn 3d states with the Mn concentration. The whole Mn 2p spectra may be explained in terms of a poorly screened $2p^53d^6$ and a well screened $2p^53d^6$ final state of the Mn with a core hole.

The hybridization of the Mn and Pd states leads to a shift of the valence–bands towards higher binding energies as the Mn concentration increases, in good agreement with the calculated Mn 3d and Pd 4d partial density of states. The satellite structure at about 6 eV distance in energy from the valence–band centroids may be caused by enhanced electron correlation in the Pd 4d band.

The magnetic properties of the Mn_xPd_{1-x} alloys and compounds are strongly correlated with their crystallographic properties and may be explained considering only the near–neighbor antiferromagnetic interactions between both Mn and Pd atoms and Mn–Mn pairs.

MnPd$_{3-x}$Sb$_x$

The modification of the electron/atom ratio in the MnPd$_{3-x}$Sb$_x$, by replacing Pd with Sb, leads to changes in the crystallographic, electronic and magnetic structure. As for the Mn$_x$Pd$_{1-x}$ system, XPS measurements were performed in joint with magnetic measurements as well as theoretical calculations in order to to have a compleat image of the total density of states at the Fermi level. From the XPS measurements, one can identify that the Mn 2p$_{3/2}$ core–level photoemission spectra exhibits a split structure, arising from the exchange interactions between the core hole and the open 3d shell, giving a clear evidence of the existence of local moments confided on Mn sites in the MnPd$_{3-x}$Sb$_x$ alloys and compounds.

The magnetic order changes gradually from antiferromagnetic state to ferromagnetic state, as the Sb concentration is increasing. The changes in the magnitude of Mn and Pd magnetic moments, the shifts of the core levels and valence–band spectra towards higher binding energies and the diminution of the valence–band sattelite structure with the Sb concentration increase may be explined by hybridization between the Mn 3d and Pd 4d states with Sb 5p states.

Chapter 7

Conclusions & Outlook

The aim of the present thesis was to investigate the electronic structure of organo–metallic materials and intermetallic compounds and alloys that have gained a large interest in the last years, by means of x–ray spectroscopic investigations as well as by magnetic measurements and theoretical calculations. This studies lead to challenging results in molecular magnetism as well in the field of the intermetallic compounds, and the following conclusions can be pointed out:

"Ferric Star" – single molecule magnet

A parallel study was performed on the $\{M[\text{Fe}(\text{L}^1)_2]_3\}\cdot 4\text{CHCl}_3$ – single molecule magnet where L^1 is an organic ligand and M is Fe or Cr, by means of experimental and theoretical techniques, in order to give a clear image on the electronic structure of the given materials. The first spectroscopic results on the "ferric star" – single molecule magnet have been presented in the given thesis. From the Fe $2p$ and $3s$ core–level lines, the charge state of the Fe was determined for the case of FeFe$_3$–star molecule after a long debate between the expected nominal valence (Fe^{3+}), from one site, and the calculated value of Fe local magnetic moment ($4\mu_B$), which implies a bivalent iron as the experimental data. The X–ray photoelectron valence band spectrum was compared with the corresponding X–ray emission spectra of the selected elements from the "ferric star"–molecule. From this comparison one can conclude that the position of the ligands remain unchanged for both of the molecule and that in the center of gravity of the transition metal $3d$ valence band one can see a small shift as the transition metal ion is changed (from Fe to Cr). The DFT calculations which were performed on the molecules are in an agreement with the measured total density of states as well as with the measured partial density of states.

Resonant X–ray emission study was also performed on the "ferric star"–single molecule. The results obtained, are more than challenging. The L_α/L_β intensity ratio for FeFe$_3$ and CrFe$_3$ varies accordingly to the excitation energy on going through the Fe L_2 threshold. The trend observed for the FeFe$_3$–star is a signature for the "high–spin" structure, or more precisely of strong magnetic systems like FeO or Heusler alloys. The explanation for this

behavior in the case of FeFe$_3$–star is because of the slow rate of the Coster–Kroning process which occur during the escape of an electron from a lower p state. The CrFe$_3$–star does not show such behavior in the L_α/L_β intensity, even though the local electronic structure at the Fe site remains the same as in the FeFe$_3$–star, and the loss of strong magnetic character appears confided on the Cr center. In order to study the magnetic interactions which occur in the "ferric star"–molecule, a simple theoretical model was used. Following the Goodenough–Kanamori–Anderson (GKA) rules, it was established that the superexchange interaction will give the magnetic ordering in the "ferric star"–molecule. Still, the theoretical results, are in a contradiction to the GKA–rules which states, that in the case of a superexchange interaction where the angle which forms the pathway between the two interacting sites is close to 90^0, will give a ferromagnetic interaction. In the case of the "ferric star"–molecules, this is not the case, the superexchange interaction giving a anti-ferromagnetic interaction. In this case we can talk abut a modification of the GKA–rules. Magnetic measurements were performed on the "ferric star" – molecule at the Physics Department form the Babeş–Bolyai University–Cluj–Napoca, Romania. The temperature dependence of the magnetic susceptibilities were determined in a field of 1 T, and for both molecules (FeFe$_3$ and CrFe$_3$), above their Curie paramagnetic temperature, a Curie–Weiss behavior $\chi = (T - \theta)^{-1}$ was observed. A changing is observed in the magnetic ordering (reordering of the magnetic domains) at about 10 K for the case FeFe$_3$ and 15 K for the case of CrFe$_3$– star.

Mn–Pd – intermetallic compounds and alloys

The electronic structure of the Mn$_x$Pd$_{1-x}$ and MnPd$_{3-x}$Sb$_x$ alloys and compounds was studied by means of photoelectron spectroscopy in close collaboration with accurate magnetic measurements. In the case of Mn$_x$Pd$_{1-x}$ alloys and compounds, the Mn $2p$ core–level photoemission spectrum, presents a visible split structure, which is arising from the exchange interactions between the core–hole and the unpaired $3d$ electrons. The interpretation of this splitting can be regarded as an evidence of local magnetic moments belonging to the Mn site. The changes, with the increase of the Mn concentration in the Mn$_x$Pd$_{1-x}$ compound, can be observed in the splitting of the Mn $2p_{3/2}$ photoemission line, reflecting the changes in the properties of the Mn $3d$ states. The antiferromagnetic interactions between Mn – Pd and Mn – Mn, will give the magnetic properties of the Mn$_x$Pd$_{1-x}$ alloys and compounds.

By introducing antimony in the Mn–Pd parent compound, one can study the modification of the electron/atom ratio, as well as the changes in the crystallographic, electronic and magnetic structure in the given system. For this reason, the MnPd$_{3-x}$Sb$_x$ system was investigated. A close–up study on the Mn site was emphasised with regard to the substitution of the Pd atoms with the Sb atoms. With regard to the Mn core–level $2p$ spectrum, one can identify the existence of local moments seen on the Mn site. This is given by the splitting of the Mn $2p_{3/2}$ main line form the MnPd$_{3-x}$Sb$_x$ system. As a characterization of the magnetic behavior of the MnPd$_{3-x}$Sb$_x$ system, one can observe a change from antiferromagnetic to ferromagnetic state, with the increase of the Sb concentration.

Outlook

In order to develop a more detailed picture of the electronic structure in the "ferric star"–molecule, more compositions are necessary to be investigated. From changing the transition–metal ions (from Fe and Cr) or ligands, one can obtain a good picture of a "ferric star" series. An interesting molecule which belongs to this series is the so–called "MnStar"–molecule, which is an ferromagnetic molecule, and in this picture, a comparison of the electronic structures of the molecules would be an asset.

Additional computational efforts are requested in order to understand better the conditions in which the Coster–Kroning process takes place in the studied molecules.

Dichroims measurements are requested, especially X–ray magnetic circular dichroism (XMCD) for probing the element specific characterization of the magnetic molecules.

With regard to the Mn–Pd system of alloys and compounds, the next step would be the computational investigation on the $MnPd_{3-x}Sb_x$ system, in order to have a more detailed picture on the partial density of states. To create also a series of investigated compounds like in the case of the "ferric star"–molecules, changes in the Pd substitution can be performed with different compounds (e.g. Te, Se).

Acknowledgements

I would like to thank in the first place to apl. Prof. Dr. Manfred Neumann for giving me the opportunity to study in his research group. My special thanks goes to him because of the great support which he provided in order to complete my PhD studies; his help in the interpretation of the experimental results, his insights and discussions have been invaluable.

My special thanks goes to Prof. Dr. Marin Coldea for the very interesting and fruitful discussions that we had during his visits in Osnabrück. Prof. Marin Coldea is also acknowledged for the fruitful cooperation on the Mn–Pd alloys and compounds.

My thanks goes also to Acad. Prof. Dr. Emil Burzo for his insight of magnetism field, during my student time spend in Cluj–Napoca, and for his constant support in my scientific activities.

I was fortunate to meet Dr. Andrei Postnikov who was a real support in my scientific work, and the discussions with him with regard to the molecular magnetism were a real help in order to clarify different aspects with regard to this research field.

During my three years in Osnabrück I had the opportunity to meet several collaborators of Prof. M. Neumann. I had the pleasure to meet Dr. Vadim Galakhov, with whom I had a very nice time also at BESSY II in Berlin. The long and nice discussions with regard to the modelling of the 3s multiplet splitting, were a real help for me in order to understand it. Prof. Dr. Viorica Simon is acknowledged for the fruitful cooperation in the field of ceramics and glasses.

My thanks are going to my colleagues, members of the AG Neumann group, who provided a nice atmosphere in our research group. Here I would like to mention Dr. Sorin Chiuzbăian, Dr. Markus Bach, Dr. Bolormaa Sanduijav, Dr. Karsten Küpper, Thorsten Mayer as formal colleagues, and of course my present colleagues Stefan Bartkowski, Werner Dudas, Michael Räkers, Manuel Prinz, Bernd Zimmerman and Stefan Robin.

I would like to give a special thank to Dr. Sorin Chiuzbăian, who was supporting me during my master thesis here in Osnabrück, and for his real support in my first months as a PhD student.

I would like to give thanks to the people "who are behind" the Graduate School *Synthesis and Characterization of Surfaces and Interfaces assembled from Cluster Molecules* apl. Prof. Dr. Jürgen Schnack and Dr. Wolfgang Mikosch. I would like to acknowledge the financial support received from the Federal State of Lower Saxony.

The work in the Department of Physics was more enjoyable thanks to the administrative assistance of Ms. Marion von Landsberg, Ms. Brigit Guss, Ms. Anna–Klara Ostendorf and Ms. Frauke Riemann.

I am grateful to my wife Andreea, who was beside me in all this three years, encouraging me, supporting me and having a LOT of patience with me. To my parents I would like to thank them for their trust in me, and for their constant support which they provided during my studies in Cluj-Napoca. Although the distance is considerable, they were always beside me and encouraging me.

Bibliography

[1] D. Gatteschi. *Molecular magnetism, an interdisciplinary field.* 2002.

[2] B. Pilawa. New concepts of molecular magnets. *Ann. Phys.*, 8:191–254, 1999.

[3] M. Verdaguer, A. Bleuzen, C. Train, R. Garde, F. Fabrizi de Biani, and C. Desplanches. . *Phil. Trans. R. Soc. Lond.*, 357:2959, 1999.

[4] M. N. Leuenberger und D. Loss. Quantum computing in molecular magnets. *Nature*, 284:789–793, 2001.

[5] W. Hallwachs. Über den Einfluß des Lichtes auf elektrostatisch geladene Körper. *Wiedemann'sche Annalen*, 33:301–312, 1888.

[6] J .J Thomson. Cathode Rays. *Philosophical Magazine*, 44:293–316, 1897.

[7] H. Robinson nad W. F. Rawlinson. *Phil. Mag.*, 28:277, 1914.

[8] R. G. Steinhardt and E. J. Serfass. *Anal. Chem.*, 25:679, 1953.

[9] K. Siegahn, C. Nordling, A. Fahlman, R. Nordberg, K. Hamrin, G.Johansson, T. Bergmark, S.-E. KArlsson, I. Lindgren, and B. Lindberg. *Nova Acta Regiae Soc. Sci Upsaliensis*, 20, 1967.

[10] C. R. Brundle and A. D. Baker. *Electron spectroscopy: Theory, Thechniques and Applications.* 1979.

[11] C. S. Fadley. Phd thessis, university of california at berkeley.

[12] C. S. Fadley and D. A. Shirley. *J. Res. Nat. Bur. Stds*, 74A:543, 1970.

[13] K. Siegbahn, G. Johansson C. Nordling, and, J. Hedman, P. F. Hedén, K. Hamrin, U. Gelius, T. Bergmark, R. Manne, and Y. Baer. *ESCA Applied to Free Molecules.*

[14] S. Hüfner and G. K. Wertheim. *Phys. Rev. B*, 11:678, 1975.

[15] P. H. Citrin, P. Eisenberger, and D. R. Hamann. *Phys. Rev. Lett*, 33:965, 1974.

[16] C. S. Fadley. University of california at berkeley. 1970.

[17] R. Manne and T. Aberg. *Chem. Phys. Lett.*, 7:282, 1970.

[18] S. T. Manson. *J. Electron Spectrosc.*, 9:21, 1976.

[19] J. Pendry. Theory of photoemission. *Surface science*, 57:679–705, 1976.

[20] D. J. Spanjaard, D. W. Jepsen, and P. M. Marcus. Effects of transmission factors and matrix elements on angular distribution of photoemission from ag(111). *Phys. Rev. B*, 15:1728–1737, 1977.

[21] G. Borstel. Theoretical aspects of photoemission. *Applied Physics A*, 38:193–204, 1985.

[22] T. Schlathölter. Theorie der spinpolarisierten core level spektroskopie für photo- und auger- electronen. *PhD Thesis, Osnabrück*.

[23] V.I. Nefedof, N.P. Sergushin, I.M. Band, and M.B. Trazhaskovskaya. Relative intensities in x-ray photoelectron spectra. *Journal of Electron Spectroscopy and Related Phenomena*.

[24] J.H. Scofield. Hartree-slater subshell photoionization cross-section at 1254 and 1487 ev. *Journal of Electron Spectroscopy and Related Phenomena*.

[25] D. Briggs and J. C. Riviere. *Spectral Interpretation*.

[26] Stefan Hüfner. *Photoelectron Spectroscopy*.

[27] T. Novakov. X-ray photoelectron spectroscopy of solids, evidence of band structure. *Phys. Rev. B*.

[28] G. Wertheim, R. Cohen, A. Rosencweig, and H. Guggenheim. Multiplet splitting and two electron excitations in trivalent rare earths. *Electron Spectroscopy*.

[29] K. Kim and R. Davis. Electron spectroscopy of nikel-oxygen system. *Journal of Electron Spectroscopy and Relatet Phenomena*.

[30] K. Kim. X-ray photoelectronic spectroscopic studies of the electronic structure of coo. *Physical Review B*.

[31] G. V. der Laan, C. Westra, C. Haas, and G. A. Sawatzky. Satellite structure in photoelectron and auger spectra of ccopeer dihalides. *Physical Review B*.

[32] B. Veal and A. Paulikas. Final state screening and chemical shifts in photoelectron spectroscopy. *Physical Review B*.

[33] S. Uhlenbrock. Untersuchungen zur elektronischen struktur einfacher uebergangsmetall-oxide-unter besonderer beruecksichtigung des nikel-oxide.

[34] S. Hüfner, G. K. Wertheim, D. N. E. Buchanan, and K. W. West. *Physical Letters*, 46A:420, 1974.

[35] S. Hüfner and G. K. Wertheim. *Chemical Physical Letters*, 24:527, 1974.

[36] S. Hüfner and G. K. Wertheim. *Physical Letters A*, 47:349, 1974.

[37] J. M. Hollas. *High resolution spectroscopy.*

[38] Doniach S. and Sunjic M. Many electron singularity in x-ray photoemission and x-ray line spectra from metals. *J. Phys. C*, 4C31:285, 1970.

[39] M. Cardona and L. Ley. Photoemission in solids. Springer Verlag, Berlin, Heidelberg, 1978.

[40] J. C. Slater. Quantum theory of atomic structure. *McGraw-Hill*, 2, 1960.

[41] J. H. Wood and G. W. Pratt Jr. *Physical Review.*

[42] C. S. Fadley, D. A. Shirley, A. J. Freeman, P. S. Bagus, and J. V. Mallow. Multiplet splitting of core-electron binding energies in transition-metal ions. *Physical Review Letters.*

[43] C. S. Fadley and D. A. Shirley. Multiplet splitting of metal-atom electron binding enegies. *Physical Review A.*

[44] van Vleck. The dirac vector model in complex spectra. *Physical Review*, 45:405, 1934.

[45] E-K Viinikka and Y. Öhrn. *Physical Review B*, 11:4168, 1975.

[46] P. S. Bagus, A. J. Freeman, and F. Sasaki. *Physical Review Letters*, 30:850, 1973.

[47] V. R. Galakhov, S. Uhlenbrock, S. Bartkowski, A. V. Postnikov, M. Neumann, L. D. Finkestein, E. Z. Kurmaev, A. A. Samokhvalov, and L. I. Leonyuk. X-ray photoelectron 3s spectra of transition metal oxides. *arXiv:cond-mat/9903354v1*, 1999.

[48] B. W. Veal and A. P. Paulikas. *Physical Review Letter*, 51:1995, 1983.

[49] A. K. See and L. E. Klebanoff. Spin–resolved nature of 3s photoemission from ferromagnetic iron. *Physical Review B*, 51:7901–7904, 1995.

[50] Z. Xu, Y. Liu, P. D. Johnson, B. Itchkawitz, K. Randall, J. Feldhaus, and A. Bradshaw. Spin polarized photoemission study of the Fe 3s multiplet. *Physical Review B*, 51:7912–7915, 1995.

[51] W. J. Lademan and L. E. Klebanoff. Investigation of satellites associated with Fe 3s photoemission. *Physical Review B*, 55:6766–6769, 1997.

[52] F. U. Hillebrecht, T. Kinoshita, Ch. Roth, H. B. Rose, and E. Kisker. Spin resolved Fe and Co 3s photoemission. *Journal of Magnetism and Magnetic Materials*, 212:201–210, 2000.

[53] F. Parmigiani and L. Sangaletti. Electronic correlation effects in the Ni 3s and Co 3s X–ray photoelectron spectra of NiO, CoO, K_2NiF_4 and K_2CoF_4. *Chemical Physics Letters*, 213:613–618, 1993.

[54] L. Sangaletti, L. E. Depero, P. S. Bagus, and F. Parmigiani. A proper Anderson Hamiltonian treatment of the 3s photoelectron spectra of MnO, FeO, CoO and NiO. *Chemical Physics Letters*, 245:463–468, 1995.

[55] D. A. Shirley. High–resolution X–ray photoemission spectrum of the valence band of gold. *Physical Review B*, 5:4709–4714, 1972.

[56] S. Tougaard and P. Sigmund. Influence of elastic and inelastic scattering on energy spectra of electrons emitted from solids. *Physical Review B*, 25:4452–4466, 1982.

[57] S. Tougaard and B. Jørgensen. Inelastic Background Intensities in XPS Spectra. *Surface Science*, 143:482–494, 1984.

[58] S. Tougaard. Low Energy Inelastic Electron Scattering Properties of Noble and Transition Metals. *Solid State Communications*, 61:547–559, 1987.

[59] S. Tougaard. Quantitative analysis of the inelastic background in surface electron spectroscopy. *Surface and Interface Analysis*, 11:453–472, 1988.

[60] S. G. Chiuzbăian. Electronic structure and magnetism of selected materials, 2003.

[61] C. N.Berglund and W. E. Spiecer. Photoemission studies of copper and silver: Theory. *Physical Review*, 136:A1030–A1044, 1964.

[62] T. Albers. Untersuchung ionenstossinduziert effecte bei der tiefenprofileanalyse an oxidichen multischichtsystemen mittels roentgenphotoelectronenspektroskopie, 1994.

[63] J. Stöhr. *NEXAFS Spectroscopy*. Berlin: Springer, 1992.

[64] A. Kotani and S. Shin. Resonant inelastic x-ray scattering spectra for electrons in solids. *Rev.Mod. Phys.*, 73:203–246, 2001.

[65] H. A. Kramers and W. Heisenberg. über die streuung von strahlung durch atome. *Z. Phys.*, 31:681–708, 1925.

[66] Y. Kayanuma and A. Kotani. *Core-level Spectroscopy in Condensed Systems.* Springer, Heidelberg, 1988.

[67] S. Tanaka, Y. Kayanuma, and A. Kotani. Theory of the resonant 5p→3d x-ray emission spectra in ceo$_2$. *Journ. Phys. Soc. Japan*, 59:1488–1495, 1990.

[68] J. Nordgren, G. Bray, S. Gramm, R. Nyholm, J. E. Rubensson, and N. Wassdahl. Soft x-ray emission spectroscopy using monochromatized synchrotron radiation (invited). *Rev. Sci. Instrum.*, 60:1690–1696, 1989.

[69] http://www.elettra.trieste.it/experiments/beamlines/bach/index.html.

[70] http://www.bessy.de/.

[71] O. Kahn. *Molecular Magnetism*. VCH, Weinheim, 1993.

[72] J. Kortus A. V. Postnikov and M. R. Pederson. Density Functional Studies of Molecular Magnets. *Scientific Highlight of the Month*, 2003.

[73] David N. Hendrickson George Christou, Dante Gatteschi and Roberta Sessoli. Single - Molecule Magnets. *www.mrs.org/publications/bulletin*, pages 66–71, 200.

[74] Pardi L. Sessoli R. Gatteschi D., Caneschi A. . *Science*, 265:1054, 1994.

[75] D. M. Adams H.-L. Tsai G. Christou S. M. J. Aubin, M. W. Wemple and D. n. Hendrickson. . *J. Am. Chem. Soc*, 118:7746, 1996.

[76] R. Sessoli, D. Gatteschi, A. Caneschi, and M. A. Novak. Magnetic bistability in a metal ion cluster. *Nature*, 365:141–143, 1994.

[77] R. Sessoli A. Cornia D. Gatteschi. . *Chem. Commun*, page 725, 2000.

[78] M.A. Bolcar G. Christou H.J. Eppley K. Folting D.N. Hendrickson J.C. Huffman R.C. Squire H.-l. Tsai S. Wang G. Aromi, S.M.J Aubin and M.W. Wemple. . *Polyhedron*, 17:3005, 1998.

[79] R.E.P. Winpenny. In perspectives in Supramolecular Chemistry . *Transition metals in supramolecular chemistry*, 5:193–223, 1998.

[80] B. Demleitner R. W. Saalfrank. *Perspectives in Supramolecular Chemistry*.

[81] E. Uller F. Hampel R. W. Saalfrank, I. Bernd. *Angew. Chem. Int. Ed. Engl*, 36:2482–2485, 1997.

[82] M. M. Chowdhry F. Hampel R. W. Saalfrank, I. Bernd. Ligand to metal ratio controlled assembly of tetra- and hexanuclear clusters towards single-molecule magnets. *Chemistry a European Journal*, 7:2765–2769, 2001.

[83] O. Kahn. *Molecular Magnetism*. John Wiley and Sons, Singapore, 1993.

[84] W. Linert and M. Verdaguer. *Molecular Magnets*. Springer–Verlag, Wien, 2003.

[85] J. S. Miller and A. J. Epstein. *MRS Bulletin*, 25:21, 2000.

[86] A. L. Barra, A. Caneschi, A. Cornia, F. Fabrizi de Biani, D. GAtteschi, C. Sangregorio, R. Sessoli, and L. Sorace. *J. Am. Chem. Soc.*, 121:5302, 1999.

[87] A. F. Takács, A. V. Postnikov, M. Neumann, K. Kuepper, A. Shceurer, S. Sperner, R. W. Saalfrank, and K. C. Prince. Electronic structure study by means of x - ray spectroscopy and theoretical calculations of the "ferric star" single molecule magnet. *J. Chem. Phys.*, submitted Aug. 2005.

[88] A. Cornia, A. C. Fabretti, P. Garrisi, C. Mortalo, D. Bonacchi, D. Gatteschi, R. Sessoli, L. Sorace, W.Wernsdorfer, and A. L. Barra. Energy–barrier enhancement by ligand substitution in tetrairon(iii) single–molecule magnets. *Angewandte Chemie – International Edition*, 43:1136, 2004.

[89] J. Kortus (unpublished).

[90] R. Koch, S. Schromm, H. Rupp, and P. Müller. private communication.

[91] A. V. Postnikov and S. Blügel. to be published.

[92] G. Beamson and D. Briggs, editors. *High Resolution XPS of Organic Polymers: The Scienta ESCA300 Database*. John Wiley & Sons, Chichester, 1992.

[93] F. Parmigiani and L. Sangaletti. Electronic correlation effects in the Ni 3s and Co 3s x–ray photoelectron spectra of NiO, CoO, K_2NiF_4, and K_2CoF_4. *Chemical Phys Lett.*, 213:613–618, 1993.

[94] L. Sangaletti, L. E. Depero, P. S. Bagus, and F. Parmigiani. A proper anderson hamiltonian treatment of the 3s photoelectron spectra of mno, feo, coo, and nio. *Chemical Phys Lett.*, 245:463–468, 1995.

[95] J. Zaanen, G. A. Sawatzky, and J. W. Allen. Band gaps and electronic structure of transition metal compounds. *Phys. Rev. Lett.*, 55:418–421, 1985.

[96] B. Mayer, S. Uhlenbrock, and M. Neumann. Xps–satellites in transition–metal oxides. *J. Electron. Spectrosc. Relat. Phenom*, 81:63–67, 1996.

[97] V. R. Galakhov, A. I. Poteryaev, E. Z. Kurmaev, V. I. Anisimov, St. Bartkowski, M. Neumann, Z. W. Lu, B. M. Klein, and Tong-Rong Zhao. Valence-band spectra and electronic structure of $CuFeO_2$. 56(8):4584–4591, August 1997.

[98] Fulvio Parmigiani and Luigi Sangaletti. Fine structures in the X-ray photoemission spectra of MnO, FeO, CoO, and NiO single crystals. *J. Electron Spectrosc. Relat. Phenom.*, 98–99:287–302, January 1999.

[99] K. C. Prince, M. Matteucci, K. Kuepper, S. G. Chiuzbăian, S. Bartkowski, and M. Neumann. Core-level spectroscopic study of FeO and FeS_2. 71(8):085102–1–085102–9, February 2005.

[100] E. S. Ilton, W. A. deJong, and P. S. Bagus. Intra–atomic many–body effects in p–shell photoelectron spectra of Cr^{3+} ions. *Phys. Rev. B*, 68:125106, 2003.

[101] V. R. Galakhov, St. Uhlenbrock, St. Bartkowski, A. V. Postnikov, B. Mayer, M. Neumann, L. D. Finkelstein, E. Z. Kurmaev, and L. I. Leonyuk. $3s$ exchange splitting in transition metal oxides. Unpublished, `http://arXiv.org/abs/cond-mat/9903354`.

[102] W. H. Press, S. A. Teukolsky, W. T. Vetterling, and B. P. Flannery. Numerical recipes in c: The art of scientific computing. *Chambridge University Press*, 1992– Chambridge.

[103] U. Korte and G. Meyer-Ehmsen. Diffuze reflection high–energy electron diffraction. *Phys. Rev. B*, 48:8345–8355, 1993.

[104] R. Szargan, K.-H. Hallmeier, R. Hesse, A. Kopczynski, S. A. Krasnikov, L. Zhang, T. Chassé, O. Fuchs, C. Heske, and E. Umbach. X-ray fluorescence spectroscopy at U41–PGM by means of ROSA–present status and results. BESSY Annual Report 2001.

[105] Pablo Ordejón, Emilio Artacho, and José M. Soler. Self-consistent order-N density-functional calculations for very large systems. 53(16):R10441–R10444, April 1996.

[106] José M. Soler, Emilio Artacho, Julian D. Gale, Alberto García, Javier Junquera, Pablo Ordejón, and Daniel Sánchez-Portal. The SIESTA method for *ab initio* order-N materials simulation. 14(11):2745–2779, March 2002.

[107] http://www.uam.es/siesta.

[108] Daniel Sánchez-Portal, Emilio Artacho, and José M. Soler. Analysis of atomic orbital basis sets from the projection of plane-wave results. 8(26):3859–3880, May 1996.

[109] Javier Junquera, Óscar Paz, Daniel Sánchez-Portal, and Emilio Artacho. Numerical atomic orbitals for linear scaling. 64(23):235111–1–235111–9, November 2001.

[110] John P. Perdew, Kieron Burke, and Matthias Ernzerhof. Generalized gradient approximation made simple. 77(18):3865–3868, October 1996.

[111] A. V. Postnikov, S. G. Chiuzbǎian, M. Neumann, and S. Blügel. Electron spectroscopy and density-functional study of "ferric wheel" molecules. *J. Phys. Chem. Solids*, 65(4):813–817, 2004.

[112] A. V. Postnikov, Jens Kortus, and S. Blügel. Ab initio simulations of Fe-based ferric wheels. *Molecular Physics Reports*, 38:56–63, 2003.

[113] K. Kuepper. Electronic and magnetic properties of transition metal compounds: An x-ray spectroscopic study, 2005.

[114] According to recent calculations, the central position of substitutional Cr is by 1 eV/molecule more favorable than the peripherical one.

[115] J. P. Crocombette, M. Pollak, F. Jollet, N. Thromat, and M. Gautier-Soyer. X-ray-absorption spectroscopy at the Fe $L_{2,3}$ threshold in iron oxides. 52(5):3143–3150, August 1995.

[116] M. V. Yablonskikh, Yu. M. Yarmoshenko, V. I. Grebennikov, E. Z. Kurmaev, S. M. Butorin, L.-C. Duda, J. Nordgren, S. Plogmann, and M. Neumann. Origin of magnetic circular dichroism in soft x-ray fluorescence of Heusler alloys at threshold excitation. 63(23):235117–1–235117–10, June 2001.

[117] We emphasize that the occupation of Fe or Cr states in the FeCr$_3$ star remains qualitatively the same also for other possible configurations: when the Cr atom substitutes a peripheral site, or with different setting of magnetization directions over Fe, Cr atoms.

[118] P. W. Anderson. Antiferromagnetism. Theory of Superexchange Interaction. *Physical Review*, 79:350–356, 1950.

[119] P. W. Anderson. Exchange in Insulators: Superexchange, Direct Exchange, and Double Exchange. In G. T. Rado and H. Suhl, editors, *Magnetism*, volume 1, chapter 3, pages 25–85. Academic Press, New York, 1963.

[120] P. W. Anderson. Theory of Magnetic Exchange Interactions: Exchange in Insulators and Semiconductors. In F. Seitz and D. Turnbull, editors, *Solid State Physics*, volume 14, pages 99–214. Academic Press, New York, 1963.

[121] P. W. Anderson. *Physical Review*, 115:2, 1950.

[122] Hogni Weihe and Hans Güdel. Quantitative interpretation of the gooudenough–kanamori rules: A critical analysis. *Inorg. Chem.*, 36:3632–3639, 1997.

[123] W. Geerstma and D. Khomskii. Influence of side groups 90^0 superexchange: A modification of the goodenough–kanamori–anderson rules. *Phys. Rev. B*, 54:5, 1996.

[124] C. J. Gomez-Garcia, J. J. Borras-Almenar, E. Coronado, and L. Ouahab. . *Inorg. Chem.*, 33:4016, 1994.

[125] I. M. Mbomekalle, B. Keita, M. Nierlich, U. Kortz, P. Berthet, and L. Nadjo. . *Inorg. Chem.*, 42:5143, 2003.

[126] J. H. Westbrook. *Intermetallic Compounds*. John Wiley and Sons, 1977.

[127] F. Heusler. *Verhandl. Deut. Phys. Ges.*, 5:219, 1903.

[128] L. Néel. *Ann. Phys.*, 17:5, 1932.

[129] M. Raney. *US Patent*, 1,628,190, 1927.

[130] E. S. Sperry. *Trans. AIME*, 29:280, 1899.

[131] G. Tamman and A. Ruhenbeck. *Z. Anorg. Chem.*, 223:288, 1935.

[132] E. Fitzer. Molybdenum disilicide as a high temperature material. *Plansee Proceedings*, F. Benesovsky, ed. Pergamon Press, London, 1956, 1955.

[133] A. N. Blum, N. P. Mokrovskii, and A. R. Regel. *7th All Union Conference on Properties of Semiconductors, Kiev*, 1950.

[134] V. M. Goryunova. *PhD Thesis*. PhD thesis, 1951.

[135] H. Welker. *Z. Naturforsch*, 11:744, 1952.

[136] N. S. Kurnakov and S. F. Zhemchuzhnii. *Z. Anorg. Chem*, 60:1, 1908.

[137] J. S. Koehler and F. Seitz. *J. Appl. Mech.*, 14:A217, 1947.

[138] M. J. Marcinkowski, R. M. Feiker, and N. Brown. *J. Appl. Phys.*, 3:1303, 1960.

[139] P. Eckerlin and H. Kandler. *Structure Data and Elements and Intermetallic Phases*. K. -H. Hellwege, Landolt–Börnstein, vol 6, group III, 1971.

[140] D. Tian, S. C. Wu, F. Jona, and M. Marcus. *Solid State Commun.*, 70:199, 1989.

[141] B. T. Jonker, J. J. Krebs, and G. A. Prinz. *Phys. Rev. B*, 39:1399, 1989.

[142] Y. U. Idzerda, B. T. Jonker, W. T. Elam, and G. A. Prinz. *J. Appl. Phys.*, 67:5385, 1990.

[143] P. Schieffer, M. H. Tuilier, M. C. Hanf, C. Krembel, G. Gewiner, D. Chandesris, and H. Magnam. *Phys. Rev. B*, 57:15507, 1998.

[144] M. Wutting, Y. Gauthier, and S. Blügel. *Phys. Rev. Lett.*, 70:3619, 1993.

[145] S. Blügel. *Appl. Phys. A: Mater. Sci. Process*, 63:595, 1996.

[146] J. Burger and J. Wucher. *Compt. rend.*, 245:2230, 1958.

[147] J. Crangle. *Phil. Mag.*, 5:335, 1958.

[148] J. Wucher. *Collogue National de Magnetisme(Centre National de la Recherche Scientifique)*, page 139, 1958.

[149] J. Burger and J. Wucher. *Compt. rend.*, 251:2667, 1960.

[150] E. O. Wollan. *Phys. Rev.*, 122:1710, 1961.

[151] J. W. Cable, E. O. Wollan, W. C. Koehler, and M. K. Wilkinson. *Suppl. J. Appl. Phys.*, 33:1340, 1962.

[152] D. Watanabe. *Trans. Japan Inst. Metals*, 3:234, 1962.

[153] G. Grube and O. Winkler. *Z. Electrochem.*, 42:815, 1936.

[154] H. Sato and R. S. Toth. *Phys. Rev.*, 127:469, 1962.

[155] J. Friedel. *Nuovo Cimento Suppl.*, 2:287, 1958.

[156] P. W. Anderson. *Phys. Rev.*, 124:41, 1961.

[157] Zu. M. Zarmonshenko, M. I. Katsnelson, E. I. Shreder, E. Z. Kurmaev, A. Slebarski, S. Plogmann, T. Schlathölter, J. Braun, and M. Neumann. *Eur. Phys. J. B*, 2:1, 1998.

[158] S. Plogmann, T. Schlathölter, J. Braun, M. Neumann, Zu. M. Zarmoshenko, M. V. Zalonskikh, E. I. Shreder, and E. Z. Kurmaev. *Phys. Rev. B*, 60:6428, 1999.

[159] A. Kjekshus, R. Mollebud, A. F. Andersen, and W. B. Pearson. *Phil. Mag.*, 16:1063, 1967.

[160] H. Sato and R. S. Toth. *Phys. Rev. A*, 139:1581, 1965.

[161] G. Kádár and E. Krén. *Solid State Commun.*, 11:933, 1972.

[162] J. W. Cable, E. O. Wollan, W. C. Koehler, H. R. Koehler, and H. R. Child. *Phys. Rev.*, 128:2118, 1962.

[163] P. J. Webster and R. S. Tebble. *Philos. Mag.*, 16:347, 1967.

[164] L. Pál, E. Krén, G. Kádár, P. Szabó, and T. Tarnóci. *J. Appl. Phys.*, 39:538, 1968.

[165] S. Foner, R. Dolco, and E. J. McNiff. *J. J. Appl. Phys.*, 39:551, 1968.

[166] C. Fuggle, F. U. Hillebrecht, R. Zeller, Z. Zolnierek, P. Bennett, and Ch. Freiburg. *Phys. Rev. B*, 27:2145, 1983.

[167] T. Moriya. *J. Magn. Magn. Mat.*, 10:31–34, 1983.

[168] P. H. Andersson, L. Nordström, and O. Eriksson. *Phys. Rev. B*, 60:6765, 1999.

[169] P. Schieffer, C. Krembel, M. C. Hanf, and G. Gewiner. *J. Electron Spectrosc. Relat. Phenom.*, 104:127, 1999.

[170] O. Rader, T. Mizokawa, and A. Fujimori. *Phys. Rev. B*, 64:165414, 2001.

[171] O. Rader, E. Vescovo, M. Wutting, D. D. Sarma, S. Blügel, F. J. Himpsel, A. Kimura, K. S. An, T. Mizokawa, A. Fujimori, and C. Carbone. *Europhys. Lett.*, 39:429, 1997.

[172] A. Sandell and A. J. Jaworowski. *J. Electron Spectrosc. Relat. Phenom.*, 135:7, 2004.

[173] K. Siegahn, C. Nordling, G.Johansson, J. Hedman, P. F. Hedin, K. Hamrin, U. Gelius, T. Bergmark, L. O. Werme, R. Manne, and Y. Baer. *ESCA Applied to Free Molecules, North–Holand, Amsterdam*, 1971.

[174] A. Sandell, P. H. Anderson, E. Holmström, A. J. Jaworowski, and L. Nordström. *Phys. Rev. B*, 65:35410, 2001.

[175] B. Johansson and N. Martensson. *Phys. Rev. B*, 21:4427, 1980.

[176] J. Yeh and I. Lindau. *At. Data Nucl. Tables*, 32:1, 1985.

[177] M. Coldea, S. G. Chiuzbăian M. Neumann, V. Pop, L. Pascut, O. Isnard, A. F. Takács, and R. Pacurariu. *Submitted to JMMM*, 2005.

[178] E. Krén and G. Kádár. *Phys. Lett.*, 29 A:340, 1969.

[179] A. Kimura, T. Matusushita S. Suga, H. Daimon, T. Kaneko, and T. Kanomata. *J. Phys. Soc. Jap.*, 62:1624, 1993.

[180] O. K. Andersen. *Phys. Rev. B*, 12:3060, 1975.

Curriculum Vitae

I was born in Zalau, Sălaj district, Romania on August 18th 1977. In 2001 I graduated the Faculty of Physics at the "Babeş–Bolyai" University in Cluj–Napoca, Romania and I obtained the Diploma (Romanian: Licenţa). In 2002 I have obtained the Master Degree (Romanian: Diploma de Studii Aprofundate) at the same University. Since January 2003 I have worked in the group of apl. Prof. Dr. Manfred Neumann at the University of Osnabrück – Germany.

List of publications

1. Publications in refereed Journals

- *"Magnetic and XPS studies on $TbNi_{5-x}Al_x$"* : E. Burzo, A. F. Takács, M. Neumann and L. Chioncel Phys. Stat. Sol.(c), 2004

- *"Investigation of Sr_2FeMoO_6 by means of MCD in XAS and RXES at the Fe L edge"*: K. Kuepper, M. Raekers, K. C. Prince, F. Bondino, M. Zangrando, M. Zacchigna, F. Parmigiani, A. F. Takács, C. Piamonteze, A. T. Young, S. George, S. Robin, H. Hesse and M. Neumann: manuscript in preparation

- *"Investigation of orbital ordering in $La_{7/8}Sr_{1/8}MnO_3$ by means of x-ray linear dichroism at the Mn L edge"*: K. Kuepper, F. Bondino, K. C. Prince, M. Zangrando, M. Zacchigna, A. F. Takács, T. Crainic, M. Matteucci, F. Parmigiani, V. R. Galakhov, Ya. M. Mukovskii, A. Winiarski and M. Neumann: J. Phys. Chem. B 109 (33) 15667 - 15670 (2005)

- *"Electronic structure and X-ray spectra of defect Li_xCoO_2"* V. R. Galakhov, N. A. Ovechina, A. S. Shkvarin, S. N. Shamin, E. Z. Kurmaev, K. Kuepper, A. F. Takács , M. Raekers, S. Robin, M. Neumann and G. Gavrila: Phys. Rev. B, (2005), submitted

- *"Electronic structure study by means of X-ray spectroscopy and theoretical calculations of the "ferric star" single molecule magnet"* A. F. Takács, A. V. Postnikov, M. Neumann, K. Kuepper, A. Scheurer, S. Sperner, R. W. Saalfrank and K. Prince. Submitted at J. Chem. Phys.

- *"Effects of substitution of Sb for Pd in $MnPd_3$ compound"* M. Coldea, V. Pop, M. Neumann, A. F. Takács, O. Isnard, L. G. Pascut, R. Pacurariu. submitted at Physica Status Solidi (b)

- *"X- ray photoelectron spectroscopy and magnetism of Mn-Pd alloys"* M. Coldea, M. Neumann, S. G. Chiuzbăian, V. Pop, L.G. Pascut, O. Isnard, A. F. Takács and R. Pacurariu. submitted to J. Alloys Comp.

- *"Iron doping effect on the electronic structure in yttrium aluminosilicate galsses"* V. Simon, D. Eniu, A. Takács, K. Magyari, M. Neumann and S. Simon. Journal on Non-Crystalline Solids 351 (2005) 2365 - 2372

- *"Magnetic and electronic properties of the iron containing polyoxotungstate "* M. Prinz, A. Takács, K. Kuepper, J. Schnack, I. Balazsz, E. Burzo, U. Kortz and M. Neumann, Submitted at JMMM

2. Non refereed publications (Annual Reports, etc.)

- *"Investigation of orbital ordering in $La_{7/8}Sr_{1/8}MnO_3$ by means of x-ray linear dichroism at the Mn L edge"*: K. Kuepper, F. Bondino, K. C. Prince, M. Zangrando, M. Zacchigna, A. F. Takács, T. Crainic, M. Matteucci, F. Parmigiani, V. R. Galakhov, Ya. M. Mukovskii, A. Winiarski and M. Neumann: ELETTRA Science Highlights 2004

- *"Electronic structure of $La_{1-x}Sr_xMnO_3$: Resonant Inelastic X-ray Scattering (RIXS)"*: K. Kuepper, V. R. Galakhov, A. F. Takács, M. Neumann, and Ya. M. Mukowskii: BESSY Annual Report 2003.

- *"Electronic structure of $[Fe(FeL_2)]\cdot 4CHCl_3$ where $L=NO_2$: Normal X-ray emission (XES)"*: A. F. Takács, K. Kuepper, M. Neumann, T. Crainic, D. Wett, R. Szargan, R. W. Saalfrank and A. Scheurer: BESSY Annual Report 2003.